uOttawa

L'Université canadienne
Canada's university

FACULTÉ DES ÉTUDES SUPÉRIEURES ET POSTOCTORALES

uOttawa

L'Université canadienne
Canada's university

FACULTY OF GRADUATE AND POSDOCTORAL STUDIES

Charles Chiu
AUTEUR DE LA THÈSE / AUTHOR OF THESIS

M.A.Sc. (Electrical Engineering)
GRADE / DEGREE

School of Information Technology and Engineering
FACULTÉ, ÉCOLE, DÉPARTEMENT / FACULTY, SCHOOL, DEPARTMENT

Fabrication of Surface Plasmon Waveguide Devices in *CYTOP* with Microfluidic Channels

TITRE DE LA THÈSE / TITLE OF THESIS

R.N. Tait
DIRECTEUR (DIRECTRICE) DE LA THÈSE / THESIS SUPERVISOR

CO-DIRECTEUR (CO-DIRECTRICE) DE LA THÈSE / THESIS CO-SUPERVISOR

N.G. Tarr

H. Schriemer

Gary W. Slater
Le Doyen de la Faculté des études supérieures et postdoctorales / Dean of the Faculty of Graduate and Postdoctoral Studies

Fabrication of Surface Plasmon Waveguide Devices in *CYTOP* with Microfluidic Channels

By

Charles Chiu

A thesis submitted to the Faculty of Graduate Studies and Post-doctoral Studies in partial fulfillment of the requirements for the degree of Master of Applied Science in Electrical Engineering

12/21/2009

Ottawa-Carleton Institute for Electrical and Computer Engineering
School of Information Technology and Engineering
University of Ottawa
Ottawa, Ontario, Canada

©Charles Chiu Ottawa, Canada, 2010

Library and Archives Canada

Published Heritage Branch

395 Wellington Street
Ottawa ON K1A 0N4
Canada

Bibliothèque et Archives Canada

Direction du Patrimoine de l'édition

395, rue Wellington
Ottawa ON K1A 0N4
Canada

Your file Votre référence
ISBN: 978-0-494-65538-2
Our file Notre référence
ISBN: 978-0-494-65538-2

NOTICE:

The author has granted a non-exclusive license allowing Library and Archives Canada to reproduce, publish, archive, preserve, conserve, communicate to the public by telecommunication or on the Internet, loan, distribute and sell theses worldwide, for commercial or non-commercial purposes, in microform, paper, electronic and/or any other formats.

The author retains copyright ownership and moral rights in this thesis. Neither the thesis nor substantial extracts from it may be printed or otherwise reproduced without the author's permission.

AVIS:

L'auteur a accordé une licence non exclusive permettant à la Bibliothèque et Archives Canada de reproduire, publier, archiver, sauvegarder, conserver, transmettre au public par télécommunication ou par l'Internet, prêter, distribuer et vendre des thèses partout dans le monde, à des fins commerciales ou autres, sur support microforme, papier, électronique et/ou autres formats.

L'auteur conserve la propriété du droit d'auteur et des droits moraux qui protège cette thèse. Ni la thèse ni des extraits substantiels de celle-ci ne doivent être imprimés ou autrement reproduits sans son autorisation.

In compliance with the Canadian Privacy Act some supporting forms may have been removed from this thesis.

While these forms may be included in the document page count, their removal does not represent any loss of content from the thesis.

Conformément à la loi canadienne sur la protection de la vie privée, quelques formulaires secondaires ont été enlevés de cette thèse.

Bien que ces formulaires aient inclus dans la pagination, il n'y aura aucun contenu manquant.

Acknowledgements

I would like to first dedicate this thesis to my parents, sister and friends whom has helped to foster a supportive and enjoyable environment throughout my academic study. I would also like to thank all persons who have made contributions to this thesis. This includes the guidance from my supervisors Pierre Berini and Niall Tait, fabrication experience form Richard Daviau and Norman Fong, and experimentation help from Ewa Lisicka-Shrzek, Mchal Tensor, Ali Akbari, Asad Khan, Fan Hui and Israel De Leon. My regards also go to Carleton University fabrication lab personnel Rob Vandusen, Rick Adams, and Carol Adams as well operators from GroupIV Semiconductors. They have all made the research in the lab a smooth and pleasant experience.

Abstract

Long Range Surface Plasmon Polariton (LRSPP) waveguide biosensors were fabricated and optically characterized. The topology comprised of thin (*35 nm*) *Au* stripe waveguide devices embedded in thick (*~18 μm*) *CYTOP* claddings. Patterned regions of the *Au* surface were exposed from its top cladding through O_2 plasma etching. The etched *CYTOP* cavity acted as mircofluidic channels for containment of index-matched sensing fluid. The fabrication process was documented and examined for dimension and structure/surface profiles. The presented data and figures are: optical index measurements, thickness measurements, microscope images, SEM images, and AFM profiles. Optical characterizations were performed on full *CYTOP* cladded and half cladded, channel-filled straight waveguides. LRSPP modes were excited through end-fire coupling with fiber-optics. The measured propagation losses were *6.33 dB/mm* and *10.46 dB/mm* respectively. The results deviated from the simulated value of *7.2 dB/mm* and were suspected to originate from material and structure properties of *CYTOP*.

Table of Contents

1. Introduction 6
1.1 Optical Biosensors 6
1.2 Long Range Surface Plasmon Polariton Biosensors 11
1.3 Process Flow 17
1.4 Thesis Structure 19
2. *CYTOP* Claddding 20
2.1 Bottom Cladding 20
2.1-1 Fabrication Process 20
2.1-2 Thickness, Index and Roughness Check 23
2.2 Top Cladding 26
2.2-1 Fabrication Process 26
2.2-2 Heat and Solvent Issues 28
2.2-3 Solutions and Checks 30
3. Lithography 33
3.1 Bi-layer Lithography 33
3.1-1 Layout and Mask 33
3.1-2 Device Level Lithography Process 35
3.1-3 Past Issues 38
3.1-4 Metal Liftoff 40
3.1-5 Bi-layer, Sidewall and Dimension Problems/Solutions 41
3.2 Channel Lithography 49
3.2-1 Layout and Mask 49
3.2-2 Channel Level Lithography Process 53
3.2-3 Post Development Check 57
4. *CYTOP* Etching 59
4.1 CF_4/O_2 Etching 59
4.1-1 Etch Rate Tests 59
4.1-2 Etch Profile 60
4.2 O_2 Etch 63
4.2-1 Etch Rate Test 63

4.2-2 Etch Profile ... 63
4.2-3 Etch Quality Check ... 65
4.3 Final Devices ... 70
5. Optical Characterization ... 72
5.1 Setup Description ... 72
5.2 Embedded Device ... 75
5.2-1 Measurement ... 75
5.2-2 Analysis ... 76
5.3 Channel-filled Device ... 78
5.3-1 Measurement ... 78
5.3-2 Analysis ... 80
6. Concluding Remark and Future Work ... 83
Appendix ... 85
I. Processed Wafer List ... 85
II. CWS 19 Microscope Process History ... 86
References ... 91

1. Introduction

1.1 Optical Biosensors

With the advent of photonics systems and the maturity of micro fabrication processing, biosensors have become practical devices of great interest. Biosensors are analytical devices which can detect biochemical substances. Traditionally, detection in biological systems is performed by introducing probes and tagging them onto specific targets [1]. These probes are then excited with light and an emission of another wavelength can then be observed. This technique has the drawbacks of time-consuming labeling process and photobleaching (a process which the probes cease to emit light after a certain time period). Thus, the underlying goal of micro-fabricated biosensors is to improve on this conventional technique by providing label-free, direct sensing and quantitative monitoring of biological and chemical substances. The optical approach to accomplishing this goal is to create transducers that perform detection through light and are sensitive to a specific target analyte. For roughly two decades, different methods of realizing these optical transducers have emerged. These methods are broad and vary between technologies, topologies and applications [2]. Examples of the more distinct utilized technologies are: fiber-optics, photonic crystals, LED microcells, waveguide couplers, integrated waveguides, and surface plasmons.

The fiber-optic approach presented in [3],[4] involves directing one end of the detection fiber to a membrane. The membrane is functionalized to immobilize analytes at its surface. Sensing is performed by observing changes in the reflected optical properties such as beam intensity. This method has the advantage being lower cost than integrated device alternatives.

The photonic crystal (PC) approach makes use of the concept behind Bragg diffractions. This means that when the device is subjected to light, particular bands of wavelengths will be attenuated due to internal reflections between lattice sites. The authors in [5] fabricated a PC planar waveguide with the ability to

immobilize anaytes at the surface. This changes the allowed bands of light propagating through the waveguide, thereby signifying detection of analytes. The authors of [6],[7] took another approach by changing the distance between lattice points of the PC. This change is brought upon by artificial lattice centers which swell and shrink when it comes in contact with the target analyte. This will also change the allowed bands passing through the device. PC sensors have the advantage of having a larger range of sensing applications due to its use of broad band light.

LED microcell is an arrayed approach for detecting different targets at the same time. The basic design presented in [8],[9] is to micromachine wells on top of semiconductor LEDs and then functionalize each cell to be sensitive to different analytes. Transduction is performed by powering the underlying LED and then observing the optical properties of the resulting "spot arrays" through a photodetector.

The authors of [10],[11] fabricated planar waveguide grating couplers that couple onto specifically angled incident light. The surface of the grating couplers are embedded in flow channels or flow cells. When analyte solutions flow over the surface, the light coupling angle or wavelength will change. This is the transduction mechanism behind detection. This type of sensing has a convenient platform for bulk medium sensing (in addition to surface sensing), which does not require immobilization of analytes at the sensing surface.

Integrated waveguide sensing has been under great attention because of its potential to be practically deployed in the industry. This is because integrated optical devices for communication applications have been widely available for decades. These devices are conventionally realized using planar fabrication technologies and dielectric materials. As such, there is a plethora of device designs; some of which have been adapted for biochemical sensing. This type of waveguide-based transducer is commonly known in the literature as evanescent field sensing (EFS). EFS utilizes the decaying or evanescent EM fields which extends away from the core of a waveguide and into the surrounding claddings. From Maxwell's

equations, we know that a guided wave's propagation constant is derived from applying the constituent relations subject to material properties and boundary conditions. Thus, if the cladding material is substituted with either a bulk or thin layer of another medium, the propagation constant will change accordingly. This is demonstrated in Figure 1. A non-integrated approach using cladding-stripped, fiber-optics is explained in [12]. However, the integrated approach has the advantage of having a smaller footprint.

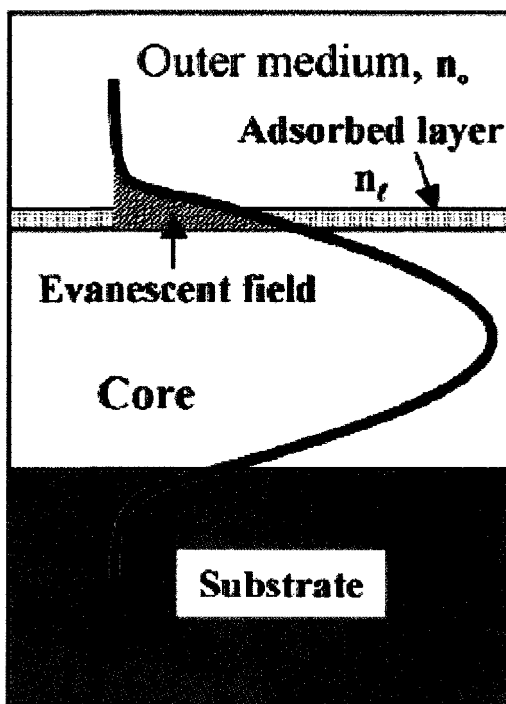

Figure 1: EFS - Surface optical index sensing of absorbed analyte adlayer using evanescent EM fields from waveguides. Adapted from [16].

Complimenting the EFS concept, the Mach-Zehnder interferometer (MZI -Figure 2) is a natural choice to be adapted for biochemical sensing as shown in [13], [14] and [15]. MZI devices require two "arms" of waveguides: a reference arm and a sensing arm. The sensing arm is the branch where it is optically exposed to the target analyte. This sensing waveguide is often functionalized with biochemical recognition elements which immobilizes the analyte from its carrier (i.e. aqueous buffer solution) and

forms a thin adlayer on top. The MZI's optical outputs are recorded from a single arm since both the reference and sensing waveguides are joined at the output. Detection is registered through output power variations caused by phase differences between the reference and sensing arm. This phase difference is caused by the adlayer formed on the sensing arm.

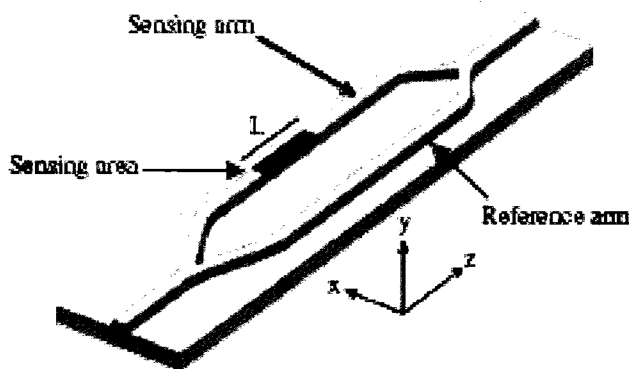

Figure 2: MZI sensor – input light enters both sensing and reference arms. Sensing arm is exposed to analyte and then combined with reference arm at output. Adapted from [14].

The last of the listed sensor technology is surface plasmon. The phenomenon of surface plasmon is also commonly termed surface plasmon polaritons (SPP) due its modal wave nature. SPP are electron waves confined on the interface between a metal and dielectric layer. This can be mathematically modeled using Drude's model of free electron gas ([17],[18]). This is a model where the elastic binding force between nucleus and electrons is omitted in the Lorentz equation. The result is a wave vector dispersion (k_{sp}) which is dependent on the permittivity ($\varepsilon_{r,M}$) of the metal and dielectric material ($\varepsilon_{r,D}$). This means that for a specific excitation wavelength, there is only one allowed plasmon wave vector. Thus, when illuminated by light, SPP can only be excited at a specific angle of incidence which corresponds to the proper longitudinal k_{sp}. One practical way of exciting a SPP is to use a prism to couple incident light onto the interface. This is shown in Figure 3 where the well known Otto and Kretschmann geometries ([21], [22]) are used to excite SPP. The Kretschmann configuration ($s=0$) can be adapted to a biosensor by sandwiching the metal layer ($\varepsilon_{r,2}$) between the prism and the analyte solution ($\varepsilon_{r,1}$). Sensing is

accomplished by noticing the angle of which there is a sudden drop in intensity of the reflected beam. This SPP coupling angle will change when the target analyte is immobilized at the analyte-metal interface. SPP sensing is currently the dominant technology behind biosensors due to its high sensitivity and low detection limits [24].

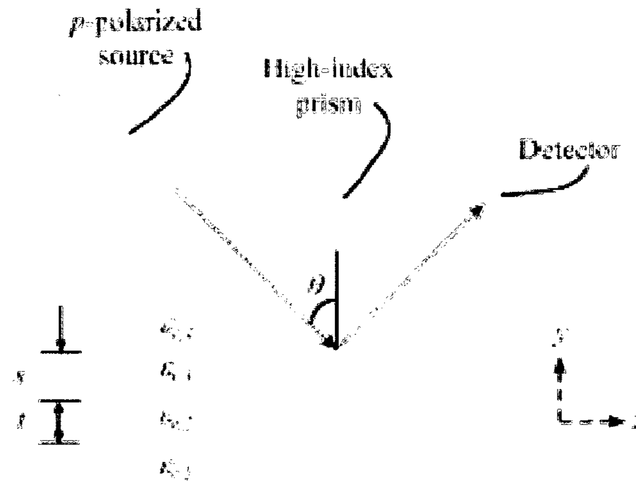

Figure 3: SPR Sensor – The Otto ($t = \infty$) and Kretschmann ($s = 0$) configurations utilizing prism coupling to excite SPP. $\varepsilon_{r,1}$, $\varepsilon_{r,2}$, $\varepsilon_{r,3}$ is the relative permittivity of lower dielectric cladding, metal and upper cladding/analyte, respectively. LRSPP can be excited from finite metal and upper cladding thickness (*s* and *t*). Adapted from [23].

For all of the introduced sensor types, there is one common function which must be implemented (for surface sensing), and that is the successful immobilization of analytes. In other words, the target molecules have to be localized on the sensing surface. This process involves formation of covalent bonds between the surface and a bio-recognition element such as a protein (enzyme or antibody). This often requires modification of the sensing surface to introduce coupling functional groups such as –OH, $-NH_2$, -COOH, and –SH. Naturally, the sensing surface medium is what dictates the possible functionalizations. In the case of dielectric surfaces, a commonly used functional group called biotin is used to adhere to a protein called avidin. Avidin-biotin affinity is one of the strongest bonds known in biology and is often used to immobilize to antibodies [1]. In the case of metal surfaces, a self-assembled monolayer (SAM) of the –SH (thiol) group can be formed on gold surfaces. The other end of the thiol chain can be specified

to be $-NH_2$ or $-C_xH_x$ for coupling onto enzymes or antibodies [25]. Once an adlayer of target analytes form on the surface, it will affect the output optical properties of the sensing device. This is shown in Figure 4 for SPP and EFS sensing.

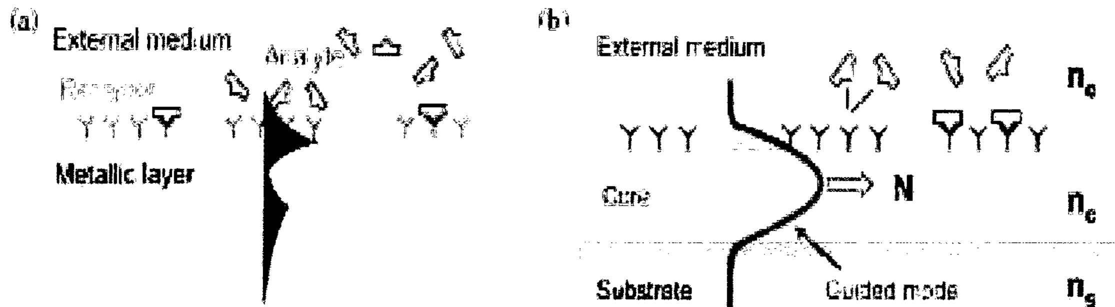

Figure 4: Surface functionalization and analyte immobilization of (a) SPR sensor (b) EFS waveguide. Adapted from [14].

1.2 Long Range Surface Plasmon Polariton Biosensors

This section presents the theory behind integrated waveguide sensors using surface plasmon polaritons. It was implied in the previous section that SPP has only one mode of propagation. This is, however, only true for single interface (metal-dielectric) geometries. Recall that the configuration presented in Figure 3 showed a planar 1-D geometry where the metal and dielectric layers are of finite thickness (*t*). This geometry actually has two modes of propagation termed s_b (symmetric bound) and a_b (asymmetric bound). The modes are named according to its corresponding top and bottom longitudinal electric field direction and its bounded nature to the metal-dielectric interfaces. This is shown in Figure 5; the corresponding mathematical derivations can be found in [26]. It should be noted that all the excited modes on a surface plasmon interface are TM modes. This is due to the fact that TE modes do not allow the interface mediums to have opposite signs of permittivity. Since metals and dielectrics are known to have opposites signs of permittivity (at optical frequencies), only TM modes are allowed for surface plasmon waves.

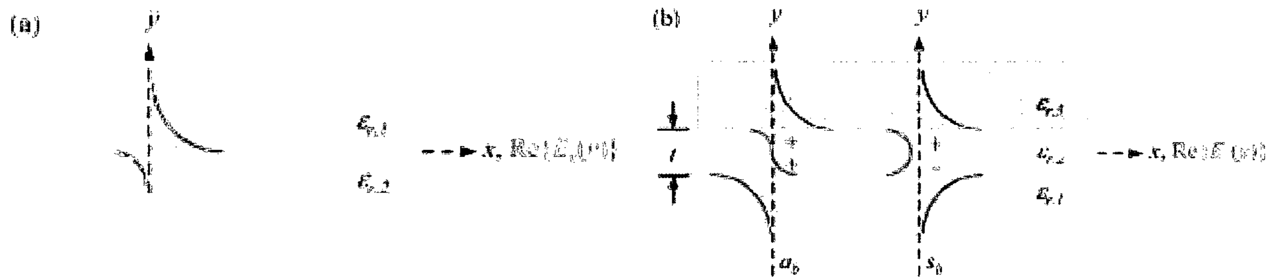

Figure 5: Longitudinal electric field strength distribution of (a) single interface SPP (b) symmetrically cladded ($\varepsilon_{r,1} = \varepsilon_{r,3}$)LRSPP modes. Adapted from [23].

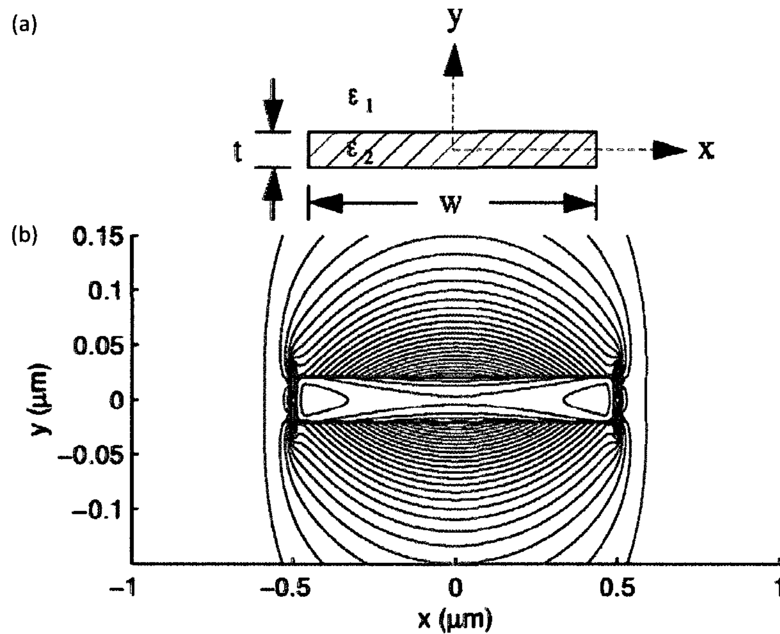

Figure 6: (a) Stripe waveguide cross-section. ε_1 and ε_2 represents the permittivity of the surrounding cladding and the metal waveguide, respectively. *t* is the thickness of the metal. (b) Electric field distribution of a LRSPP SS^0_b mode. Adapted from [27].

The slab waveguide geometry was further extended ([27]) to include a finite width dimension, resulting in a stripe waveguide structure (Figure 6). It was shown that this structure supports four 1st order modes termed: ss^0_b (symmetric-symmetric bound), sa^0_b (symmetric-asymmetric bound), as^0_b, (asymmetric-symmetric bound), and aa^0_b (asymmetric-asymmetric bound). The interesting conclusion to draw from [27] is that by limiting the metal thickness, it is possible to isolate and excite only the ss^0_b mode. Furthermore, this mode has a propagating attenuation constant that is at least 1 to 2 orders of magnitude lower than that of single interface SPP. Hence, the SPP supported on a dielectrically

sandwiched, finite metal waveguide is termed long range SPP or LRSPP. Actual performance of LRSPP structures was first fabricated and studied in [28].

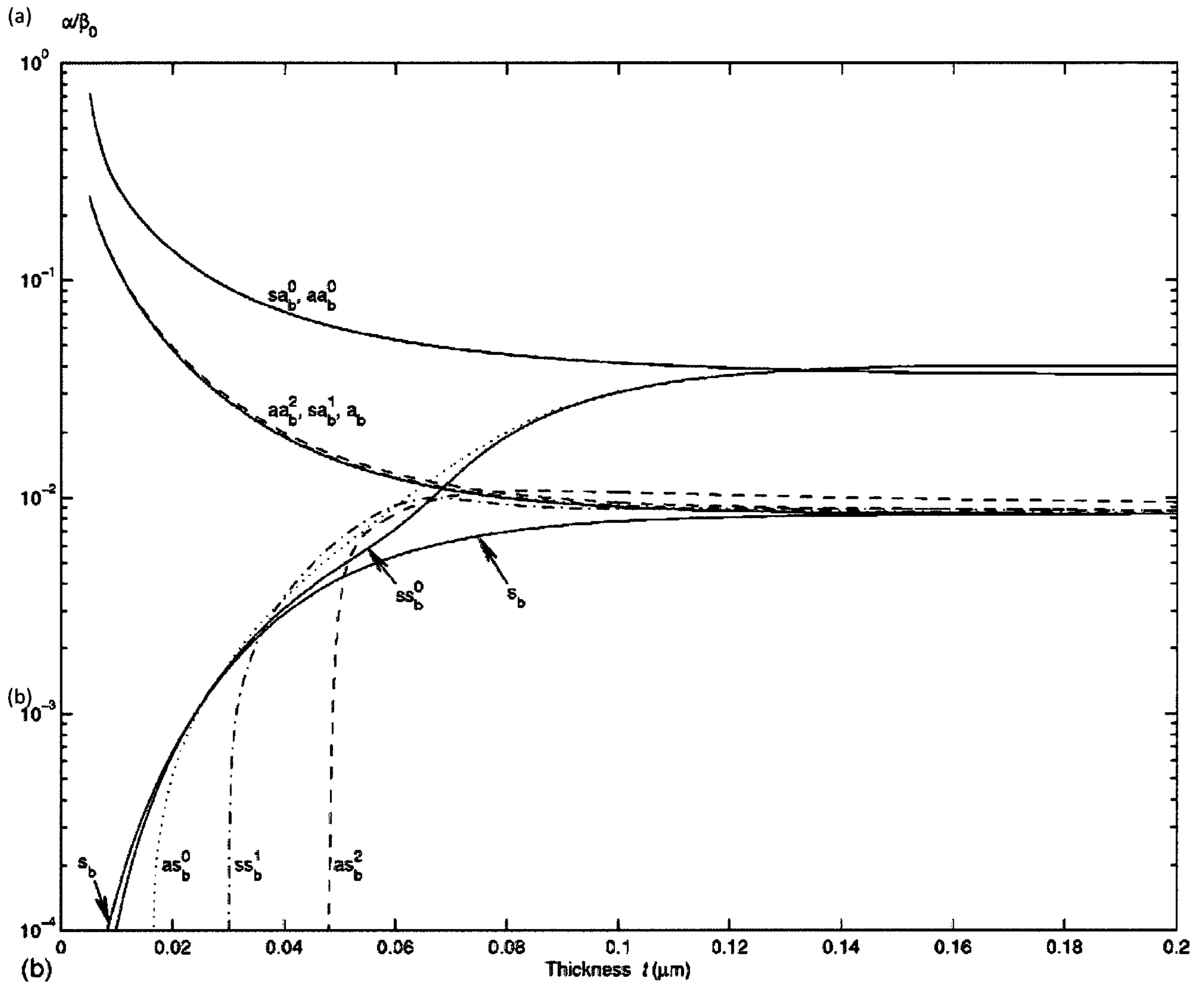

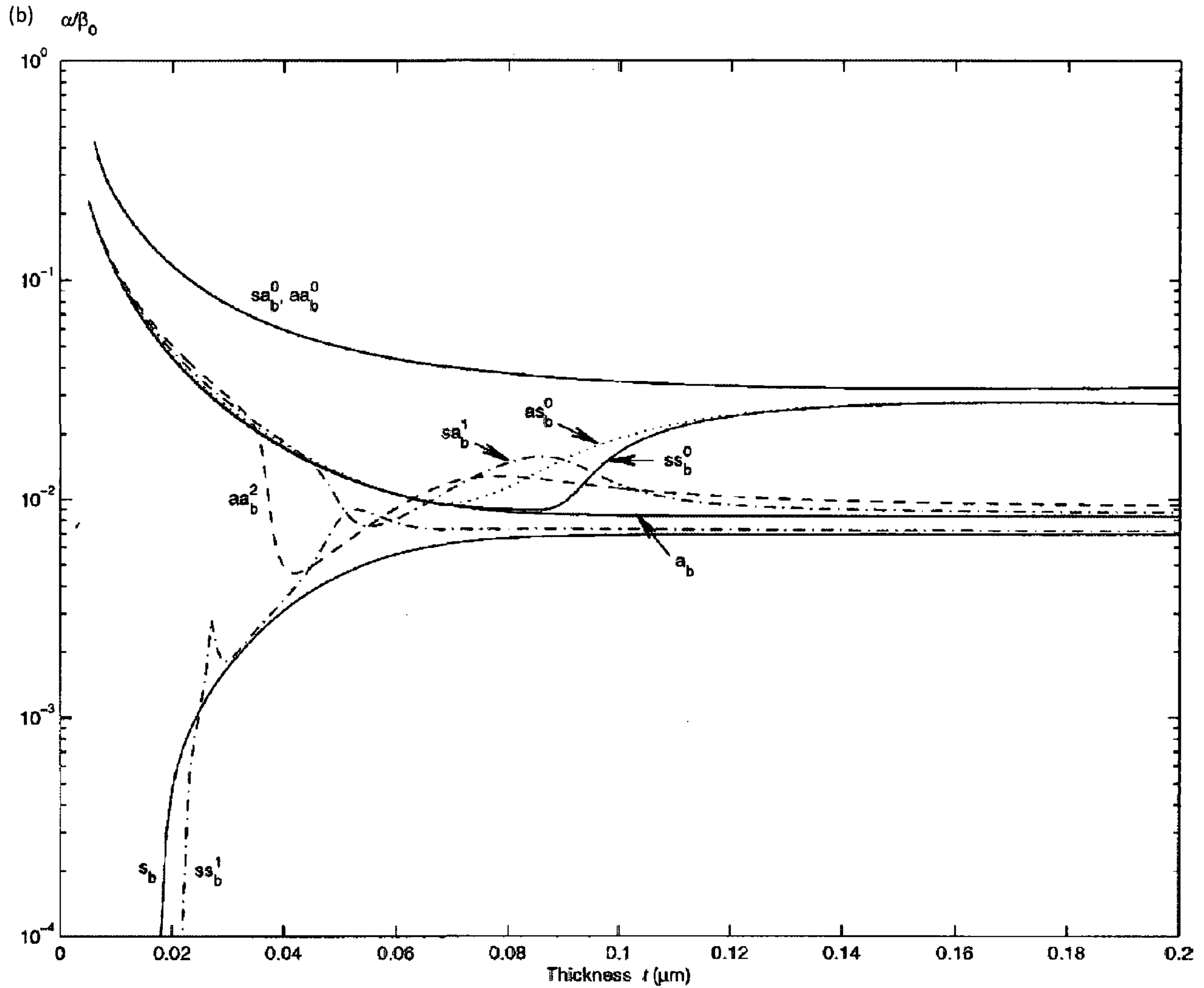

Figure 7: Various mode attenuation constants versus stripe metal thickness. (a) symmetric structure (b) asymmetric structure. Adapted from [27] and [29].

From a sensing application point of view, it is important to implement the dielectric sandwich claddings to have equal values of permittivity. In the literature, this is commonly referred to as a symmetric LRSPP structure. In contrast, mismatching permittivities between the upper and lower cladding is termed asymmetric structure. It was shown in [29] that with decreased metal thickness, the ss^0_b mode on an asymmetric structure has a higher attenuation constant than that of a symmetric structure (Figure 7). Having a low attenuation constant is important because it increases the sensitivity of waveguide-based sensors ([24]). Recall that one of the dielectric waveguide-based sensors is a MZI. Following the same

sensing concept, it is also possible to construct a LRSPP-type sensor using the MZI configuration. The surface and bulk sensitivities of LRSPP MZI were investigated in [24]. It was revealed that optimal sensitivity values were limited by the propagation length of the MZI's sensing arm, which was limited by its propagation attenuation constant. It was stated that in an ideal lossless waveguide scenario, the sensitivity increases indefinitely along with increasing sensing lengths. Thus, it is intuitively apparent that lowering the propagating attenuation constant will increase the viable sensing length of the waveguide, thereby also increasing the sensitivity of MZI devices. This is why having a symmetric structure is both critical and desirable in order to fabricate practical LRSPP biosensors.

Symmetric LRSPP devices were fabricated and reported in [30] where gold stripe waveguides were embedded in a polymer called benzocylcobutene (BCB). The gold stripes were *10-20 nm* thick and *6-10 μm* in width. In addition, the each BCB claddings (top and bottom) were *15 μm* thick. The ss^0_b mode was excited via end-fire coupling with an input laser beam using a polarization-maintaining (PM) fiber. The reported propagation loss was *6-8 dB/cm*. Although this is indeed a long-ranging propagation performance, BCB remains incompatible for sensing application. This is because BCB has an optical index of $n_{BCB} = 1.537$ ($\lambda = 1310$ nm); which is much different from that of de-ionized water ($n_{DIW} = 1.319$). This means that if one is to construct a LRSPP MZI (with BCB as the bottom cladding) and allow the sensing arm's top surface to be exposed to the analyte solution, it will result in an asymmetric structure. The direct consequence is reduced power output, hence decreased sensitivity.

In order to maintain structure symmetry and maximize sensing capabilities, the cladding material must be properly chosen so that it is index-matched to the sensing transport fluid. There are two commonly explored choices for this material: *CYTOP* and Teflon. Both materials have optical indices close to that of de-ionized water, and have been widely studied in slab LRSPP sensors. Teflon AF has an optical index of $n_{Teflon} = 1.31$ and was used in [31] to perform sensing with a gold layer interface. The gold thickness was

24 nm and attained an index detection limit of $2.5x10^{-8}$. *CYTOP* is another commercially available fluoro-polymer which has a refractive index of *1.33* (*λ = 1310 nm*). It was explored in [32] as the cladding layer when attached to a gold interface. The authors in [33] compared both materials in different configurations and sensing experiments. It was concluded that Teflon was better for bulk sensing (entire medium) and *CYTOP* was better for surface sensing (immobilized analyte adlayer).

Although Teflon and *CYTOP* have been shown to be suitable materials for sensors, the discussed configurations still utilized a prism-coupling, planar-slab geometry; operating in the s_b propagation mode. Recall that the stripe waveguides have potential for higher sensitivity due to the operating ss^0_b mode having a lower attenuation constant. Therefore, it is naturally desirable to fabricate integrated waveguide sensors using either Teflon or *CYTOP*. In [34] and [35], gold waveguide devices (i.e. MZI) were fabricated with *CYTOP* as the base cladding layer. During optical characterization tests, the entire wafer/waveguide surface was immersed in an index-matched oil (*n = 1.335*). The oil maintained structure symmetry and properly excited the LRSPP ss^0_b mode. The author reported results which matched well with those from simulation. No sensing experiments were performed, but the mode power attenuation (MPA) for straight waveguides was reported at *7.1 dB/mm*. Although the author reported good results, the presented fabrication/characterization process did not allow for any exposure selectivity of the sensing surface. In other words, it is much more desirable to fabricate devices where only selected surfaces are exposed for sensing. It is also desirable to have the rest of the devices embedded in *CYTOP* which will maintain a perfect symmetric structure while shielding the MZI reference arms from the analyte. Thus, the main goal behind this thesis is to present a process for fabricating LRSPP gold strip stripe devices in *CYTOP* with selected surfaces exposed for sensing. A preview of the proposed device is shown in Figure 8. Gold is chosen as the metal waveguide because of its chemical stability and good surface chemistry capability.

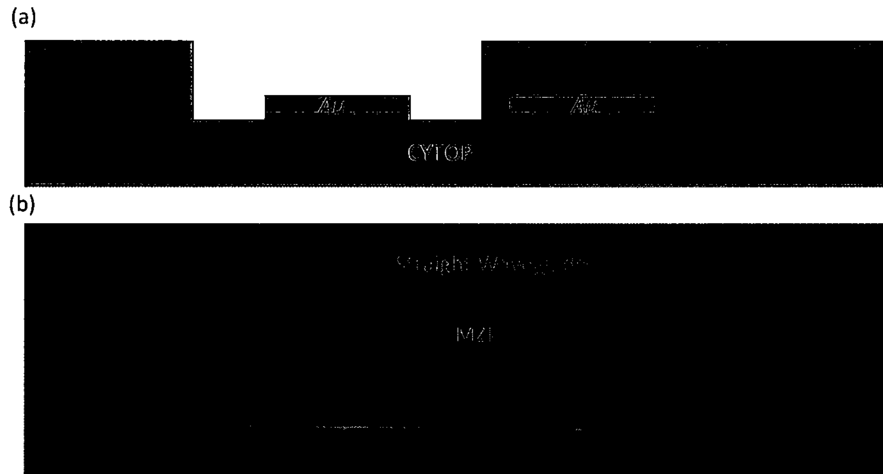

Figure 8: Proposed design of LRSPP gold stripe sensors. (a) cross section view of exposed waveguide and symmetric *CYTOP* cladded waveguide (b) top view of MZI and straight waveguide.

The last structure addition to stripe waveguide sensors is the analyte fluid flow system. Biochemical elements and reagents are usually transported in a liquid medium. Thus, a lot of biochemical sensors are designed to allow fluidic entry to the transducers. In the case of integrated structures, microfluidic channels are often implemented during the fabrication process. One common method of implementation is to mold the channels on a separate wafer and then bond it directly with the finished device. However, this is not necessary for the proposed structure in Figure 8. This is because the exposed regions can also act as fluidic channel cavities. All that is needed to encapsulate the fluid in the channels is a lid. Detailed implementation of this configuration will be presented in Chapter 5.

1.3 Process Flow

Fabrication of LRSPP stripe devices in *CYTOP* with microfluidic channels can be divided into two process levels. The first level is the device level and it involves bottom cladding *CYTOP* on silicon wafers and putting down gold stripe devices. The second level is the channel level and it involves embedding the stripe devices in full claddings of *CYTOP* and selectively exposing them for fluid sensing. This general process flow is presented in Table 1: Steps 1-6 in sequential fabrication order. Step 6 marks the end of

the entire fabrication process and the finished products are 2" or 4" wafers ready to be diced for optical testing.

Step	Description	Details
Device Level		
1	Bottom cladding of *CYTOP* on Si substrate wafers	Cladded through the process of spin-coating
2	Lithography of stripe devices	Bi-layer lithography used for proper realization of gold devices
3	Gold deposition and resist strip	E-beam metal deposition and wet solvent strip
Channel Level		
4	Top cladding of *CYTOP* on stripe devices	Embeds devices in *CYTOP* through spin-coating
5	Lithography of microfludic channels on *CYTOP* claddings	Aligned to device level lithography for proper placement of channels
6	Patterned etch of stripe devices	Top *CYTOP* claddings are dry etched with plasma
7	Optical characterization	Performed in optics lab

Table 1: General process flow for fabrication of *Au* waveguide devices in *CYTOP* with microfluidic channels.

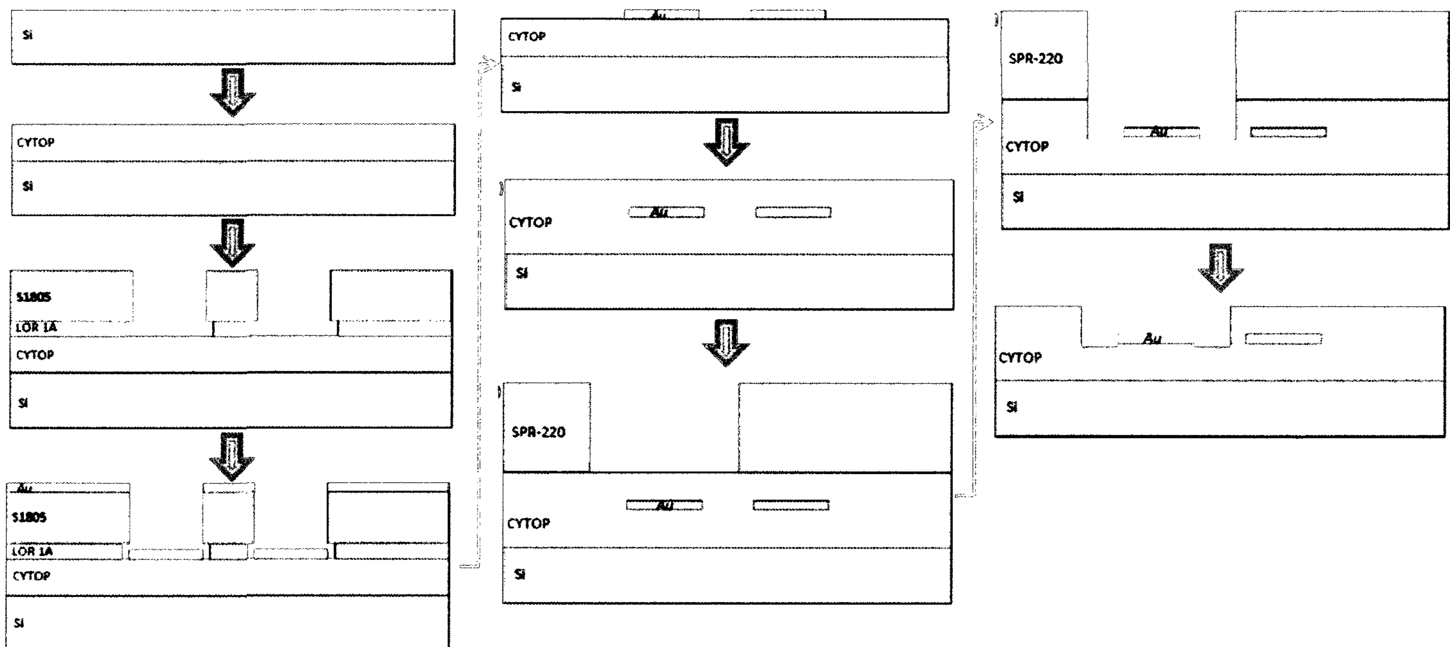

Figure 9: General process flow for fabrication of *Au* waveguide devices *CYTOP* in with microfluidic channels as described in Table 1

1.4 Thesis Structure

This thesis is structured on commonality between processes and not in sequential fabrication order. Table 1 shows that there is a general repetition of processes between the device and channel level. The repetitions are between steps 1-2 and 4-5. Therefore, this thesis is split into four main chapters as listed in the Table of Contents. This is done so that the thesis can be reviewed without constant reference to content already presented for similar processes:

2. Top and bottom *CYTOP* cladding
3. Device and channel lithography
4. *CYTOP* etching
5. Optical characterization

Within the first two chapters, a detailed, finalized fabrication process will first be summarized. This is preceeded by issues and problems encountered during the development process. Solutions and quality examinations used to address those problems will then be presented and discussed. Chapter 4 is divided into two sections presenting etch tests/results for CF_4/O_2 and O_2 plasma. The 5th chapter describes the characterization setup used for optical measurement; followed by measurements, analysis and result discussions for both embedded and channel-filled devices.

The addendum to this thesis is an appendix where extra figures and tables are available for reference. These figures serve as additional backup to material presented in the described chapters. One particular table of interest is Table 13 which lists all the wafers fabricated for the development of this thesis. This table indexes the wafers under its ID and presents a description of its production purpose as well as its availability of qualitative results. Throughout this thesis, various figures and tables will be documented with wafer IDs which can be referenced to this table.

2. *CYTOP* Claddding

2.1 Bottom Cladding

2.1-1 Fabrication Process

The *CYTOP* bottom cladding process is described in Table 2. It begins with a priming step of the silicon (*Si*) substrate wafer. This process first involved removal of the native thermal oxide (SiO_2) through a quick static bath in hydrofluoric acid (*HF*). Under normal conditions, the native SiO_2 film should strip between *15~20 sec.* [36]. This step is shown in Figure 10. The wafer was then subjected to a *10* minute dehydration and organic cleaning process using a Plasma-Preen cleaner (microwave-induced O_2 plasma).

After priming the *Si* wafer, it was then ready to be cladded with *CYTOP* (Table 2: Step 3, Figure 11a). *CTL-809M* was the grade of *CYTOP* used for the first layer. This particular grade of *CYTOP* was designed by the manufacturer (*Asahi Glass Co.*), to adhere directly onto inorganic materials such as *Si*, SiO_2, *SiN*, *Al*, *Cu* and glass. Thus, a thin layer (*0.4 μm*) was first coated to act as an adhesion layer between the *Si* substrate and successive *CYTOP* layers. Coating was done using the conventional method of spin-coating. The specific spin speed conditions are listed in the Table 2. It should be noted that in order to attain the desired thickness, the packaged *CYTOP* had to be diluted with its solvent (*CT-SOLV180*) from the manufacturer. Previous attempts of spin-coating ([34]) thick, undiluted layers of *CYTOP* led to streaking and thickness uniformity issues. The initial concentration of *CTL-809M* (or *M*-grade for short) was *9% CYTOP* by weight; thus, a digital scale was used to dilute it to *5%*. Spin-coat curves for both concentrations were provided by the manufacturer [38]. Step 4 required the wafer to be placed on a hotplate set to $50\ ^0C$ and soft-baked for *30 min.* This soft-bake step is a solvent evaporation step meant to properly dry the mixed-in solvent before spin-coating additional *CYTOP* layers. This step was followed in adherence to the documentations provided by *Asahi Glass Co* [38].

After the first adhesion layer has been properly coated, additional *CYTOP* layers were again spin-coated (Table 2: Step 5). This time, the grade of *CYTOP* used was *CTX-809SP2*, or *S*-grade. The reason behind the switch from *M*-grade to *S*-grade *CYTOP* was experimentally derived. Although both materials contain similar optical index ([38]), it was observed that M-grade *CYTOP* solutions were very easily tainted with water molecules (moisture). This is due to the fact that, in order to promote *Si* substrate adhesion, the chemical makeup of *M*-grade *CYTOP* includes Silane groups (SiH_4). The silane groups can bind with water very easily. As a result, moisture tainted *CYTOP* claddings behaved structurally different (elastic versus glass) and degraded in water over long periods of time. The S-grade *CYTOP* was not designed to contain Silane agents, thus, it was used as the bulk cladding layers. Using different *CYTOP* grades should have no optical consequence as long as the bulk *S*-grade cladding is above $7\ \mu m$ [35], and the optical index difference is on the order of *0.001*. It will be shown that both these conditions are satisfied. In Table 2: Steps 5~7, *S*-grade *CYTOP* was repeatedly spun and soft-baked until the desired thickness was achieved (Figure 11b). The last two *CYTOP* layers were thin *5%* layers instead of the bulk *9%* layers (Table 2: Step 8~10, Figure 11c). This was done to planarize the top surface to be as smooth and fine as possible. After the last layer was coated and soft-baked, the wafer was then baked on the hotplate at $200\ ^0C$ for *1.5 hr.* This was preceded by a temperature ramp from $50\ ^0C$ to $200\ ^0C$ in *1 hr.* Thus, the wafer underwent a total of *2.5 hr.* of hard-bake. The purpose of this hard-bake is to completely evaporate all the solvent [38] and bring the *CYTOP* claddings above its glass-transition temperature ($T_g = 108\ ^0C$) to improve structural robustness (Table 2: Step 12). The method of *UV* curing was explored but discarded because but *CYTOP*'s transmittance is 90% for wavelengths down to *200 nm* [38].

Step	Description	Details
1	HF dip of Si wafer to strip native thermal SiO_2. Figure 10a & 9b	*20 sec.* static dip
2	Plasma-Preen cleaning and dehydration to prime wafer for coating	Subject for *5 min.*, let cool for *5 min.*, then subject to another 5 min.
3	Spin-coat *5% CTL-809M CYTOP* (diluted *M*-grade) on wafer for *Si*-adhesion layer. Figure 11a	*500 RPM* spread spin for *10 sec.*, followed by *1000 RPM* for *20 sec.* (*~0.40 μm*)
4	Solvent evaporation bake on hotplate	*50 °C* for *30 min.*
5	Spin coat *9% CTX-809SP2 CYTOP* (S-grade) for main cladding layer. Figure 11b	*1000 RPM* spread spin for *10 sec.*, followed by *1500 RPM* for *20 sec.* (*~2.65 μm*)
6	Solvent evaporation bake on hotplate	*50 °C* for *30 min.*
7	Repeat steps 5 and 6 to attain desired thickness	Usually 2 additional layers
8	Spin coat *5% CTX-809SP2 CYTOP* (diluted S-grade) for smooth planarization of surface. Figure 11c	*500 RPM* spread spin for *10 sec.*, followed by *1000 RPM* for *20 sec.* (*~0.76 μm*)
9	Solvent evaporation bake on hotplate	*50 °C* for *30 min.*
10	Repeat steps 8 and 9 to attain desired thickness and smoothness	Usually 2 additional layers for final thickness of *10.0 μm*
11	Solvent evaporation bake on hotplate	*50°C* for *30 min.*
12	*CYTOP* hard-bake on hotplate	Temperature ramp @ *150 °C/hr.* to *200 °C* in *1 hr.*, then hold at @ *200 °C* for *1.5 hr.*

Table 2: Fabrication process flow for bottom *CYTOP* claddings.

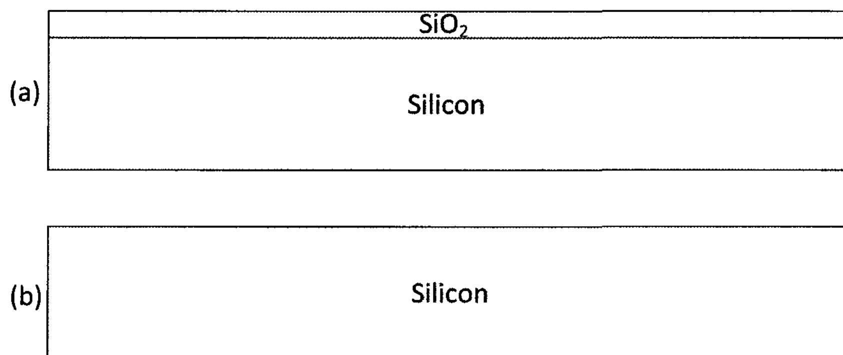

Figure 10: (a) *Si* substrate wafer with native thermal SiO_2 (b) bare *Si* substrate.

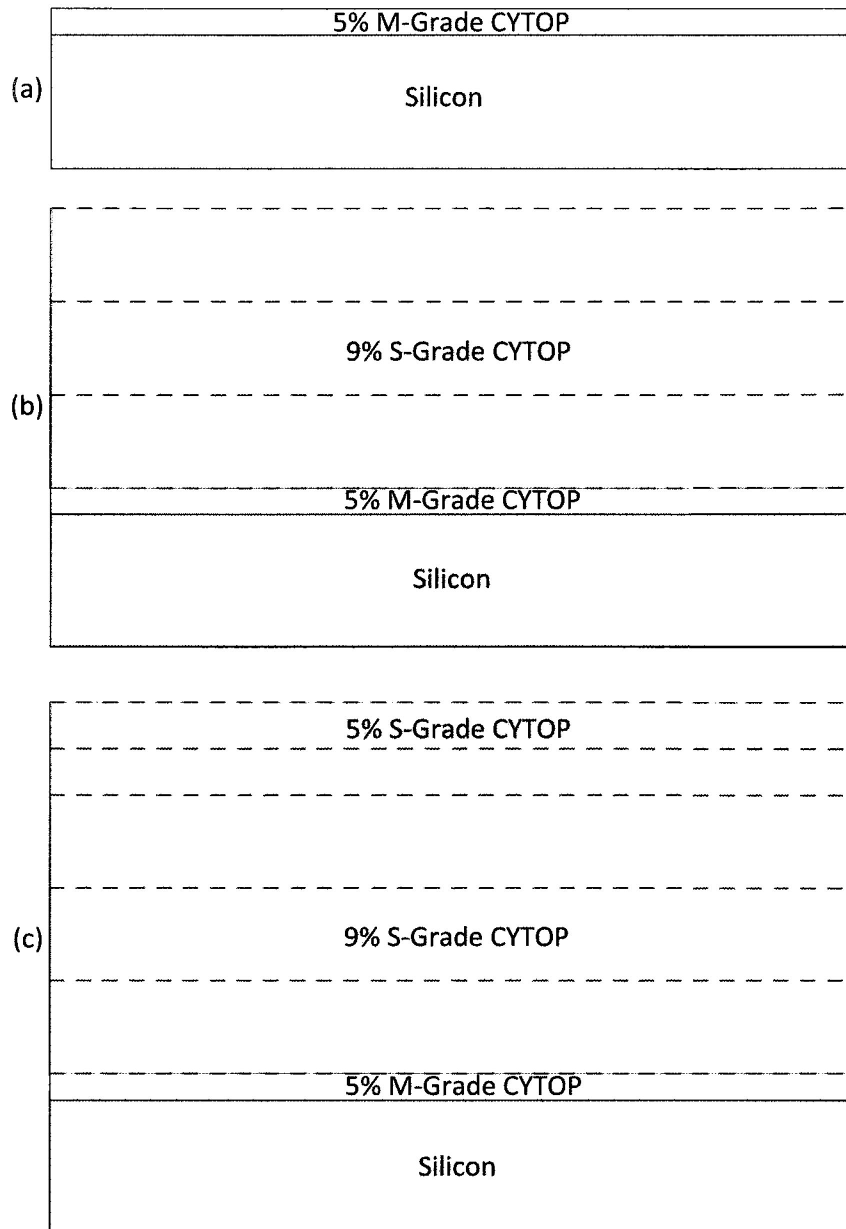

Figure 11: (a) *0.40 µm CYTOP* adhesion layer (b) *3x 2.65 µm CYTOP* bulk layers (c) *2x 0.76 µm CYTOP* planarization layers.

2.1-2 Thickness, Index and Roughness Check

In order to confirm the exact values of the coated *CYTOP* thickness and optical index, a prism coupling tool was used for measurement. The *Metricon 2010/M* is an instrument which couples laser light through a prism onto thin films or bulk materials. By varying the coupling incidence angle, different waveguide modes can be excited, which translates into a change in intensity of the reflected light from

the material. A photo-detector monitors and records the changes in intensity as incidence angle changes. A computer software then finds the angle of minimum intensities and calculates the thickness and optical index of the material under test. Similar to ellipsometric techniques, the substrate's optical index must be provided for the wavelength of laser used; in this case, the index for *Si* is *3.882* for $\lambda_0 = 632.8\ nm$. This wavelength was chosen because it allowed for measurement of *CYTOP* thicknesses below $0.5\ \mu m$.

Using prism coupling, various *CYTOP* claddings were measured for its thickness and optical index. Since the developed cladding process involved different grades of *CYTOP*, different concentrations and different spin speeds, it was necessary to gather data on each of those conditions. The measured results were compared with the manufacturer's data [38] (thickness only) in Table 3. It is worthy to note that the actual thicknesses are about $.05\text{-}0.1\ \mu m$ thinner than the target thickness. This discrepancy can be attributed to subtle factors such as environment temperature, humidity, shelf life, and instrument (spinner) accuracy. Nevertheless, we see that the process presented in Table 2 yielded $10.0\ \mu m$ of *CYTOP* cladding. This is much thicker than the theoretical requirement ($>7\mu m$) for LRSPP modes ([35]). Therefore, being slightly off target will not affect the end-result performance of the devices.

Wafer ID	***CYTOP* Cladding Layers**			**Measured Index**	**Measured Thickness (µm)**	**Measured Thickness % Standard Deviation**	**Manufactur-er's Target Thickness (µm)**
	5% M-Grade	**9% S-Grade**	**5% S-Grade**				
CLT 7	1	0	0	1.3386	0.4073	0.37	0.45
CLT 7	1	1	0	1.3385	3.0573	0.56	3.15
CLT 8	1	2	0	1.3384	5.8651	0.35	5.85
CLT 8	1	3	0	1.3384	8.5005	0.45	8.55
CLT 9	1	3	1	1.3386	9.2527	0.48	9.33
CLT 9	1	3	2	1.3386	10.0127	0.60	10.11

Table 3: Thickness and optical index measurement of *CYTOP* claddings. Measured with *Metricon 2010/M* prism waveguide coupling at $\lambda = 632.8\ nm$.

The next relevant factor to examine is the surface roughness of the *CYTOP* claddings. This is especially important because any roughness will be carried over to the metal waveguide when it is deposited on

top of the claddings. From previous theoretical studies, it was determined that the waveguide performance depended heavily on the metal thickness; thus, it is desirable to fabricate the *CYTOP* surface to be within acceptable scales of roughness (~*1 nm*). Following that, *CYTOP* cladded wafers were subjected to atomic force microscopy (AFM). This is a technique which involves a cantilever probe brought within close proximity of the surface under test. Atomic forces between the cantilever tip and the surface will produce deflection data. Therefore, surface profile images can be constructed by scanning the probe across entire surfaces. Result from AFM of the *CYTOP* surface roughness was determined to be *0.81 nm* RMS, and *0.60 nm* average as shown in Figure 12a. This is scale of roughness is less than *1 nm* and is acceptable according to simulation studies in [40]. The corresponding phase shift image (Figure 12-b) showed only slight changes in phase (less than 3.5 degrees). This indicates that there are no sudden changes in surface profile caused by extraneous particulates.

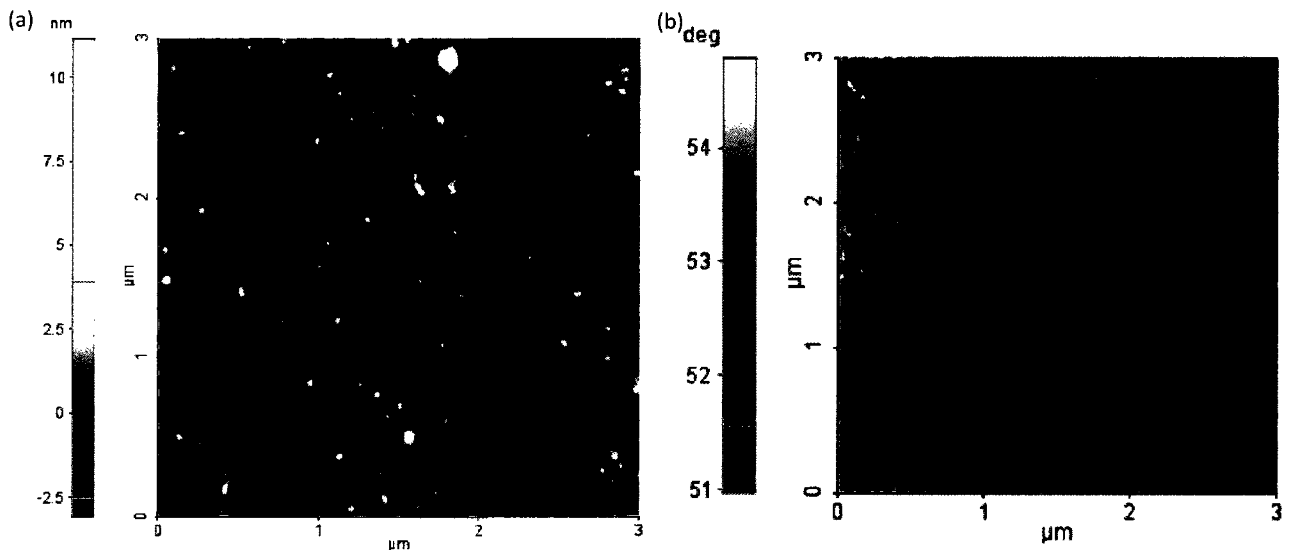

Figure 12: AFM surface roughness profile of bottom *CYTOP* cladding. *0.81 nm* RMS, *0.60 nm* average. (a) amplitude image (b) phase shift image.

2.2 Top Cladding

2.2-1 Fabrication Process

The *CYTOP* top cladding process is described in Table 4. The reader is reminded that the top claddings are coated only after the metal waveguides have been properly patterned and deposited on the bottom claddings. Details on this procedure are outlined in the next chapter. Figure 13a shows the starting point of the top cladding process. The goal is to fabricate fully embedded LRSPP devices in *CYTOP*.

The initial priming process is a simple dehydration bake on the hotplate for *15 min.* at *90 ^{0}C* (Table 4-Step 1). It was necessary to carefully monitor the temperature of the bake because heating the wafer above *108 ^{0}C* (T_g) can physically stretch the waveguides due to thermal state expansion of the *CYTOP* bottom claddings. After the dehydration bake, the wafer was spin-coated with multiple layers of *9% S-grade CYTOP*. Detailed spin-coat conditions are outlined in Table 4-Steps 2-4. Each layer underwent *30 min.* soft-bakes at *50 ^{0}C* before successive layers were spin-coated (Figure 13-b). A slow and low temperature hard bake was applied at the end.

Step	Description	Details
1	Dehydrate wafer on hotplate. Figure 13a	*15 min. @ 90 °C*
2	Spin coat *9% CTX-809SP2 CYTOP* (S-grade) for thin cladding layer. Figure 13b	*1000 RPM* spread spin for *10 sec.*, followed by *4000 RPM* for *20 sec.* (*~1.35 μm*)
3	Solvent evaporation bake on hotplate	*50 °C* for *30 min.*
4	Repeat steps 3 and 4 to attain desired thickness	Usually 5 additional layers for final thickness of *8.1 μm*
5	Solvent evaporation bake on hotplate	*50 °C* for *30 min.*
6	*CYTOP* hard-bake on hotplate	Temperature ramp @ *20 °C/hr.* to *90°C* in *2 hr.*, then hold at @ *90 °C* for *2 hr.*

Table 4: Fabrication process flow for top *CYTOP* claddings.

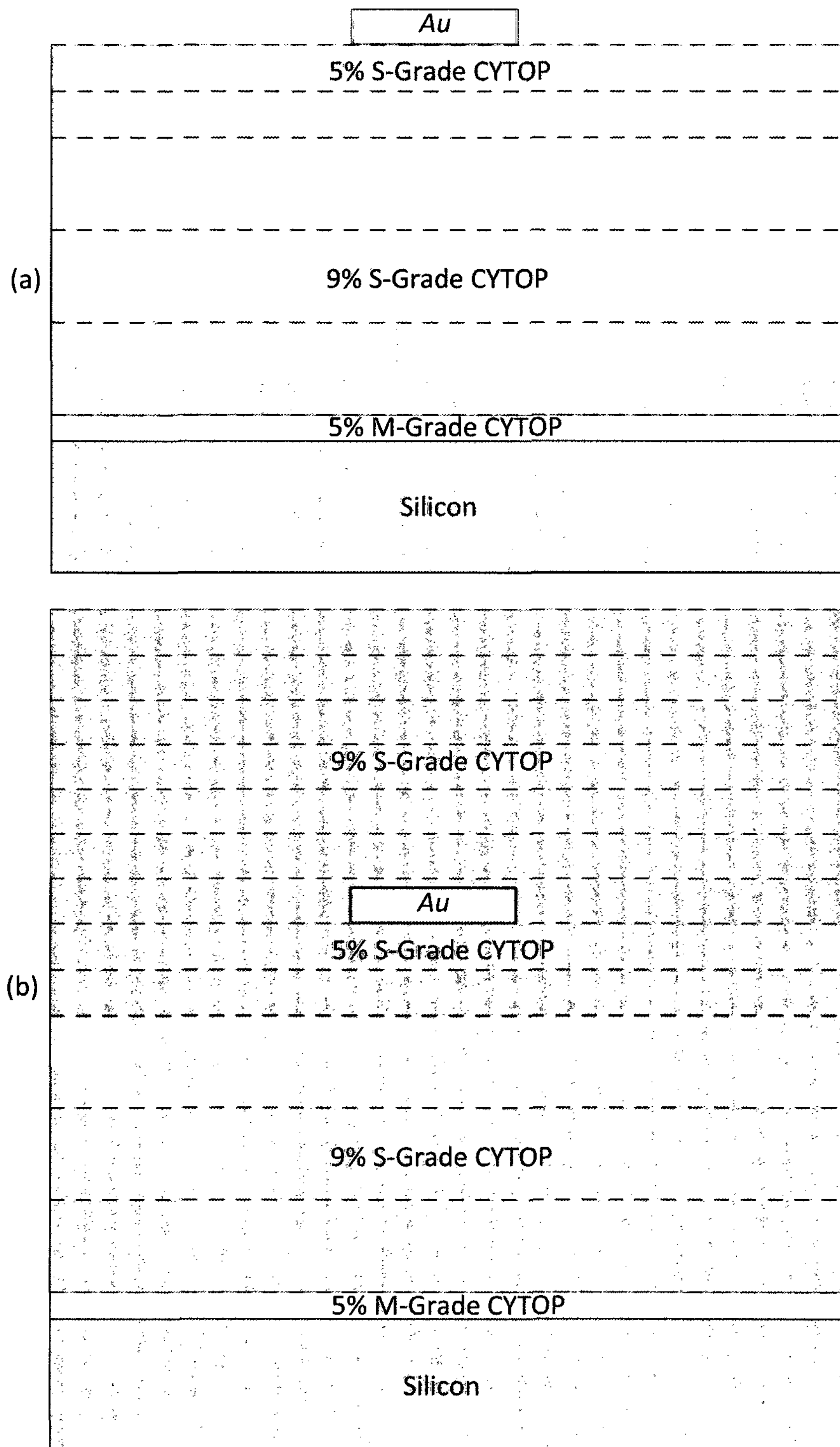

Figure 13: (a) bottom *CYTOP* claddings with *Au* waveguide (b) 6x *1.35 μm* thin *CYTOP* top claddings

2.2-2 Heat and Solvent Issues

The development for the top layer coating process presented was not as straightforward as it was for the bottom layer. More specifically, it was noticed that directly cladding thick *CYTOP* layers deformed the metal waveguides due to two factors: thermal expansion and solvent interactions. As mentioned already, heating *CYTOP* above its T_g will deform the metal waveguide. This is shown in Figure 14 where stress points, rough surfaces and relocations are clearly visible. The reason for this behavior can be attributed to the thermal expansion coefficient (TEC); which is known to show sudden variations within the range of the glass transition temperature. Thus, the device deformation exacerbates as the bake temperature increases.

The second factor affecting the metal layer is *CYTOP*'s innate vulnerability to its solvent. *CYTOP* is a fluoropolymer that cannot be "cured" in the conventional sense. The hard-bake process (Table 2-Step 6) simply ensures that the *CYTOP* cladding is dry and robust; there is no chemical reaction during the bake. As a result, when new layers of *CYTOP* were coated, the mixed-in solvent diffuses to the layers underneath. This became problematic when the wafer was introduced to the intermediate soft-bake step between layers. When this bake evaporated the solvent, the leaking gas pressure could potentially damage the waveguide from underneath thus causing ripples as shown in Figure 15a. In addition, when the soft-bake temperature is too low, or if there is a lot of trapped solvent, the bottom *CYTOP* claddings start to form cracks as shown in Figure 15b.

(a)

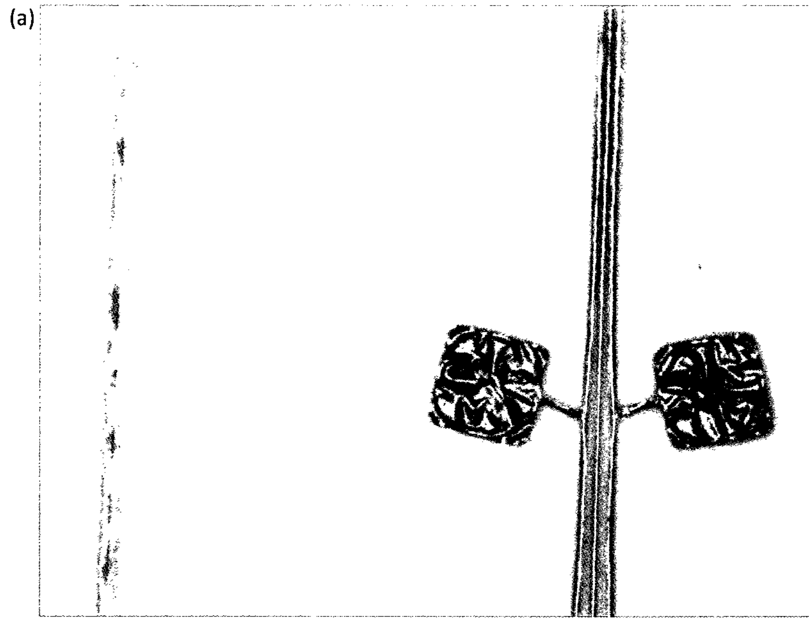

(b)

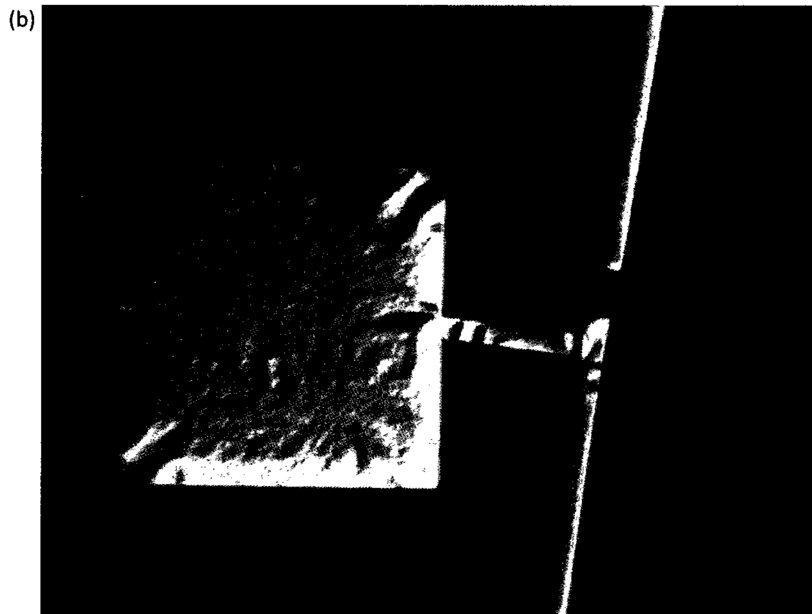

Figure 14: *Au* device deformation due to thermal expansion of top *CYTOP* cladding (a) *25x* magnification (b) *100x* magnification

Figure 15: *CYTOP*'s solvent vulnerability (a) *100x* magnification of rippled *Au* surfaces (b) *100x* magnification of lower cladding cracks

2.2-3 Solutions and Checks

Following the two problems mentioned above, it was necessary to design a procedure which involved: 1) as little solvent as possible, and 2) a baking process below T_g. To address the first point, all top *CYTOP* layers were cladded with *9%* concentration and spun with a very fast spin speed (*4000 RPM*) to attain a

very thin, non-viscous *CYTOP* layer. To address the second point, all soft-bakes were done at *50 ^0C* and the hard-bake temperature never exceeded *90 ^0C*. It was determined through experimental trials that *90 ^0C* is a temperature of which the bottom cladded wafers can be baked for more than 10 hours without any observable effect on un-embedded waveguides. In an effort to reduce damage caused by gas leakage, a very slow temperature ramp of *20 $^0C/hr$* was used to raise the temperature to *90 ^0C*. Once the wafer reached *90 ^0C*, it was held there for an additional 2.5 hrs to make sure all the solvent has evaporated from the *CYTOP*. The result from these cladding conditions is shown in Figure 16. There is still some surface bulging, but only at large metal areas (i.e. contact pads) and arm joints. There are no obvious observable deformities across the length of the waveguide devices.

The thickness requirement for the top *CYTOP* cladding is the same as the bottom cladding. Specifically, it has to be above *7 μm* for similar mode confinement to that provided by the bottom cladding. However, the derived cladding process in Table 4 suggests that it is only possible to spin one thin *CYTOP* top layer at a time; as opposed to thick bulk layers in the lower cladding. Therefore, the thickness for different layers was also measured with the prism-coupler as shown in Table 5. The thickness for each *9% S*-grade *CYTOP* layer spun at *4000 RPM* is around *1.3 μm*. This is quite different than the value provided by the manufacturer which is *1 μm*. This can be attributed to the unsuitability of spinning concentrated, viscous liquid at high speed. It was observed that during spinning, thin threads of *CYTOP* spun off the wafer; instead of liquid drops. However, this was the only way of coating *CYTOP* while delivering the least amount of solvent. Following Table 5, we see that 6 layers yielded *8 μm*, which satisfied the non-radiating condition. It was not necessary to conduct studies of the roughness of the top cladding surface since no devices were to be built on top.

(a)

(b)

Figure 16: *CYTOP* cladding with thin layers and low temperature (a) subtle surface bulges at joints and contact pads (b) unaffected waveguide devices

Wafer ID	9% S-Grade Layers	Index	Thickness (µm)	% Standard Deviation	Target Thickness (µm)
CLT 8	6	1.3387	8.02	0.49	6.0
CLT 9	8	1.3386	10.174	0.84	8.0
CLT 10	9	1.3386	11.707	0.71	9.0

Table 5: Thickness and optical index measurement of top *CYTOP* claddings. Measured with Metricon 2010/M prism waveguide coupling at *λ = 632.8 nm.*

3. Lithography

3.1 Bi-layer Lithography

3.1-1 Layout and Mask

The first level of the lithography process starts after the bottom *CYTOP* cladding has been coated. The lithography patterns put down in this layer were designed in [34]. Some example devices are shown in Figure 17-Figure 19. Since the proposed application for these devices are for biosensing, most devices in the layout are Mach-Zehnder interferometers and waveguide couplers. Figure 17a and Figure 18b are simple MZI structures with single input and output. The function of these devices was explained in Chapter 1.1. Figure 18a shows a MZI where the sensing arm is curved thereby creating a different path length between itself and the reference arm. This path difference introduces a constant 90° phase offset which is the most sensitive region of a MZI sensor. This makes the device more sensitive to temperature and bulk environment changes because the slightest fluctuation will trigger a detectable power output. Figure 17b and Figure 19a shows a MZI with dual/triple output. The sensing and reference arms are directed to a four/five port coupler which allows for differential sensing. This is done by observing and comparing the fraction of power transferred from one output to the other. Consequently, the couplers in Figure 19a represents the smallest feature size of the entire layout. This area is magnified in Figure 19b and is revealed to be three parallel stripe waveguides. These triple waveguides are *5 μm* in width and *2 μm* apart. It will be shown later that this area will serve as a reference for dimension accuracy studies.

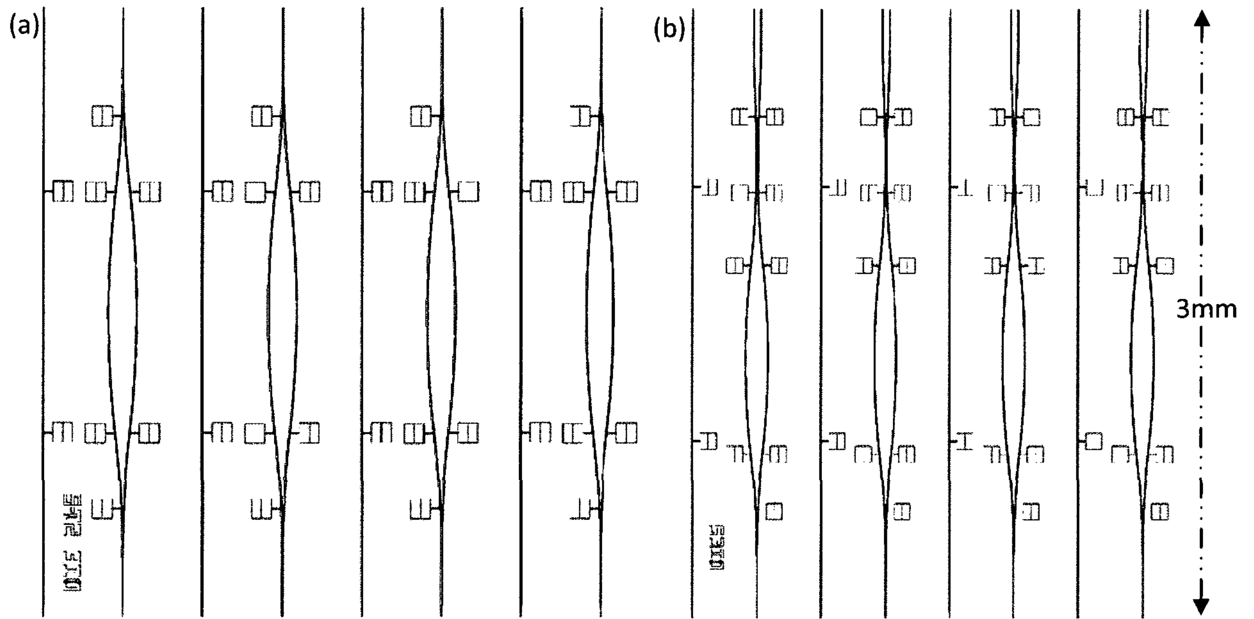

Figure 17: ***3 mm*** **long waveguide devices (a) straight waveguides and MZIs (b) Straight waveguide and MZI with dual coupling output**

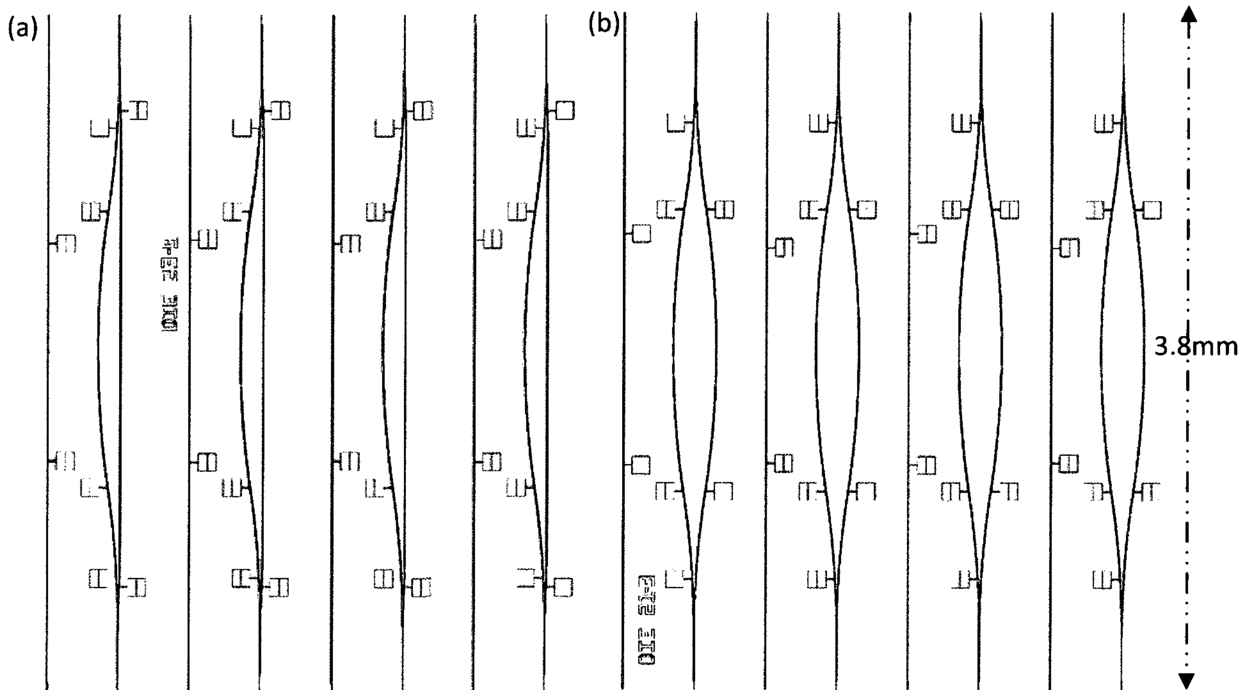

Figure 18: ***3.8 mm*** **long waveguide devices (a) straight waveguides and path adjusted MZIs (b) Straight waveguide and MZIs**

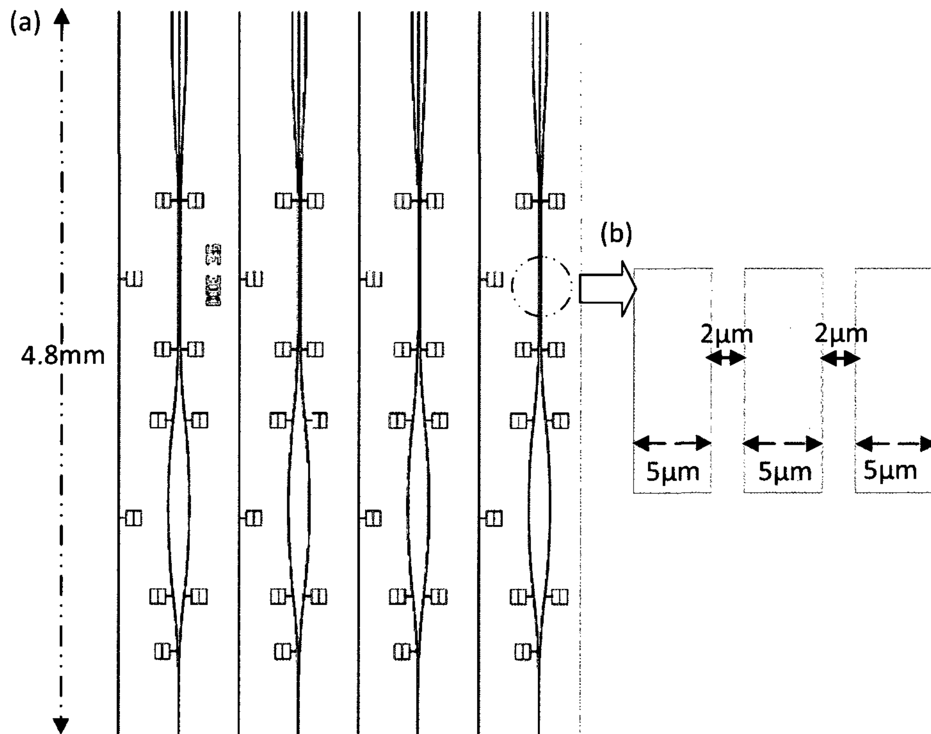

Figure 19: ***4.8 mm*** **long waveguide devices (a) straight waveguide and MZI with triple coupling output (b) triple waveguide feature size**

3.1-2 Device Level Lithography Process

A bi-layer lithography process is a common method of patterning metal devices on substrates. This method involves spinning two different resists on the wafer: liftoff resist (Figure 20b) and photoresist (Figure 20c). Only the photoresist is photo-sensitive to ultraviolet (UV) radiation exposure, but both materials are susceptible to developer etching. Once the wafer has been UV-exposed and immersed in the developer solution; the UV-exposed photoresist will first be etched away, then the exposed liftoff resist will also start to etch (Figure 20d). Depending on the liftoff resist etch time, an under-etch will occur beneath the patterned edges. The resulting side-wall profile prevents the deposited metal devices from being in contact with the adjacent bi-layer structures (Figure 20e). This is important because it helps to eliminate metal "wings" which occurs due to accumulation of metal at the corners and

sidewalls. The proposed bi-layer procedure for fabricating *CYTOP* cladded LRSPP devices is described in Table 6.

Step	Description	Details
1	Ash *CYTOP* wafer in O_2 plasma to roughen the surface	*5 sec.* for 2" wafers, *10 sec.* for 4" wafers
2	Spin coat hexamethyl disiloxane (HMDS) for resist adhesion	*1000 RPM* for *10 sec.*
3	Soft-bake on hotplate	*105 °C* for *1 min.*
4	Spin coat *LOR-1A* for liftoff resist layer (Figure 20b)	*1000 RPM* for *10 sec.*, followed by *4000 RPM* for *30 sec.* (*~105 nm*)
5	Soft-bake on hotplate	*180 °C* for *3 min.*
6	Spin coat *S1805* for photoresist layer (Figure 20c)	*1000 RPM* for *10 sec.*, followed by *4000 RPM* for *30 sec.* (*~500 nm*)
7	Soft-bake on hotplate	*115 °C* for *3 min.*
8	load bio-senor mask (1st level) in mask aligner	Align markers to flat of wafer
9	UV Exposure	*6 sec.* for thick, *~10 μm CYTOP* wafers. Exposure time adjustments depend on thickness of *CYTOP* wafer and current lamp intensity
10	Development in *MF-321* (Figure 20d)	*1'40 min.* with light agitation. Liftoff resist etch rate is *5.63 nm/s*
11	Inspection	Check small tight features under microscope. Look for edge smoothness and structural deformities. If necessary, strip entire resist coatings and repeat form step 2

Table 6: Bi-layer lithography process flow for patterning *Au* waveguide devices on *CYTOP*

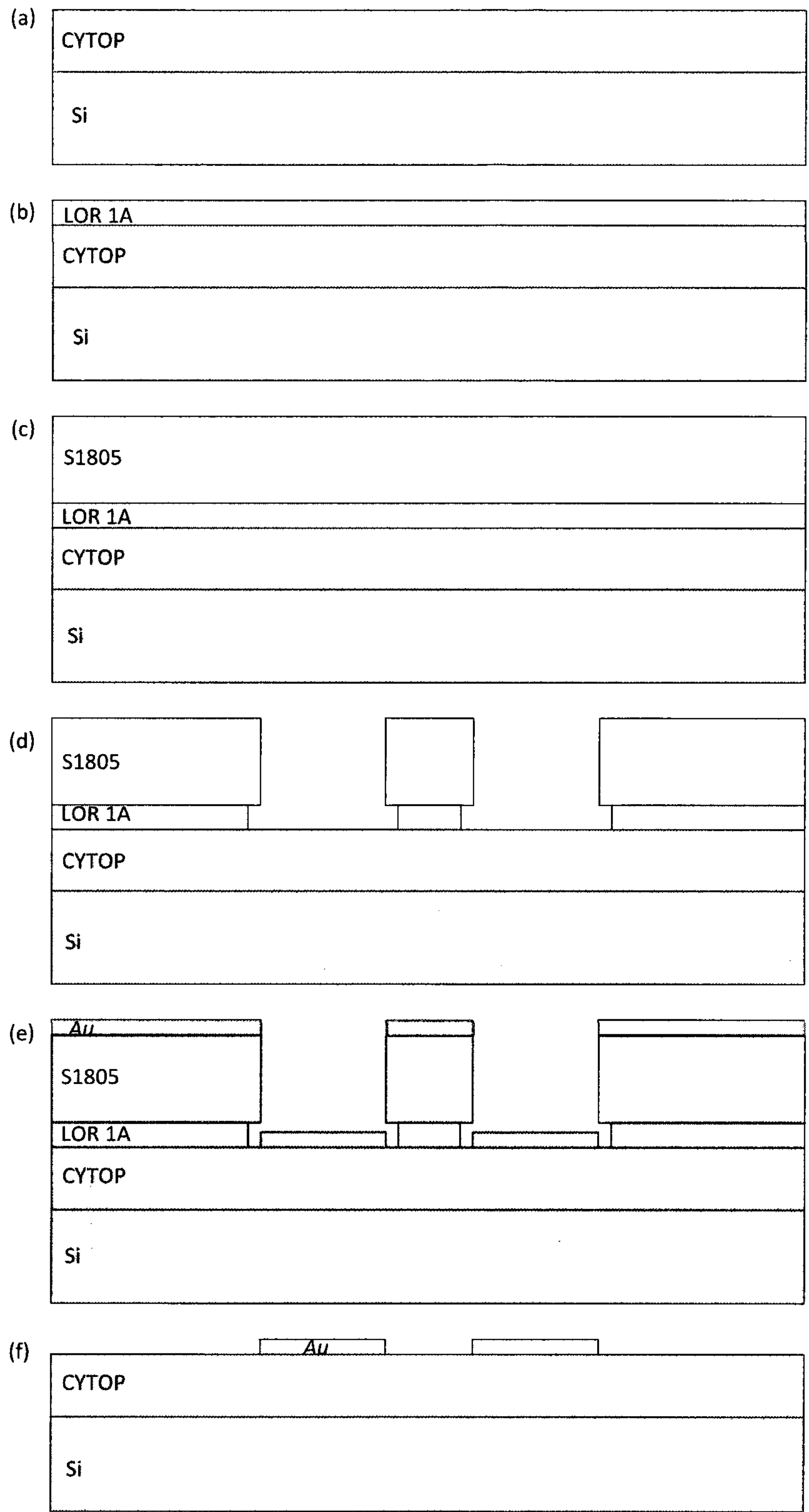

Figure 20: Process diagrams for Table 6 (a) lower *CYTOP* cladding on Si wafer (b) liftoff resist coating (c) photoresist coating (d) patterning of resists (e) gold layer deposition (f) device after resist strip

3.1-3 Past Issues

It should be noted that a previous bi-layer process was developed and used in [34]. However it was later determined that it produced slightly incorrect dimensions. This is shown in Figure 21 where the waveguides were at most *10%* wider than target (*5 μm*).The reason behind this slight error was that this process was adapted from [41] and [42] where it was used for metal waveguides on oxides. Now that *CYTOP* is the main cladding material, exact procedures for the lithographic process were revised. To start off, there is now a *5 sec.* plasma ashing step before any spin coating can be done on the claddings (Table 7: Step 1). This step cleans the *CYTOP* surface so that the resists can better adhere to the wafer. This was necessary because *CYTOP* is a fluorine-based polymer similar to Teflon; this means that it is extremely hydrophobic. Any direct spin-coat on the surface would result in patches of uneven adhesion. The next step was to revise the bi-layer process according to the manufacture technical sheets ([46], [47]) . A summary of this process is listed in Table 6. The liftoff resist and photoresist in this procedure were targeted to be *105 nm* and *500 nm* respectively (Table 6: Step 5-8). With a hard-bake temperature of *180 ^{0}C*, the liftoff resist etched at a rate of *5.63 nm/s* when immersed in the developer solution. This left *0.564 μm* of undercut beneath the patterned resists; which translated to *0.875 μm* of support width for the *2 μm* space between the triple waveguides (Figure 19b). It was important that the wafer does not get developed for too long; the reason being that the liftoff resist between the triple waveguides will eventually be completely etched away, thus destroying the desired features. This is shown in Figure 22 where it is obvious that the photoresist pattern has been either thrown "off-track" or completely collapsed. It is worthy to note that this was one of the recurring problems with the old bi-layer process; due to a faster etch rate caused by a lower hard-bake temperature (*105 ^{0}C*).

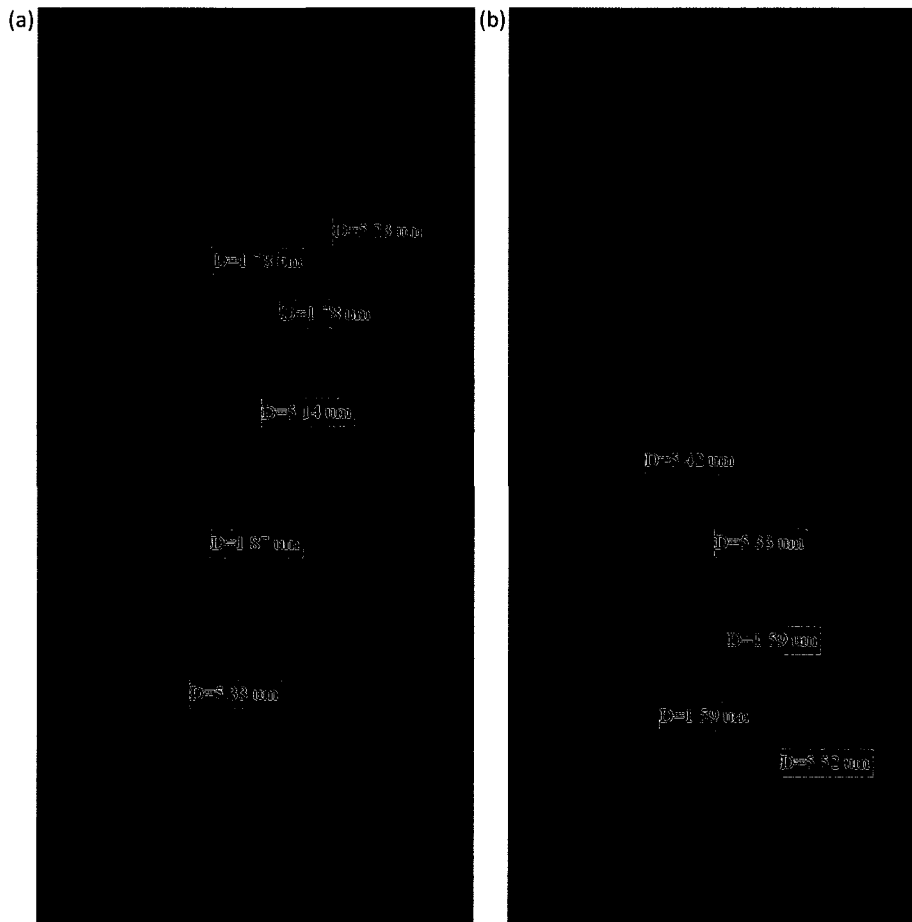

Figure 21: Off-target (wider) dimensions (a) resist patterns (b) *Au* devices.

Figure 22: Over-develop of *LOR1A* liftoff resist. Triple waveguide pattern has collapsed. Image collected by Richard Daviau.

3.1-4 Metal Liftoff

After the lithography patterns had been properly realized, the wafers were immediately subjected to metal deposition (Table 7: Step 1). It was desirable to perform this step as soon as possible in order to keep the wafer clean. Since CTYOP is known to be easily etched under plasma ([38], [43]), the wafer could not be de-scummed to eliminate surface contaminants. Gold was deposited using an electron-beam metal evaporator under vacuum. The deposition rate and thickness is controlled automatically through a power controller. Since the target thickness is very thin (*35nm*), the deposition was set low at a low rate of *2 nm/s*. The procedure was carefully monitored to make sure that the metal did not "spit" large spots of gold due to sudden changes in power. After depositing a layer of gold, the wafer was immersed in a solution of resist stripper, *Microstrip 1165* [45], and agitated within an ultrasonic basin. The combination of chemical solution and physical agitation easily lifted off the bi-layer resists and the gold layer. The details for this lift-off process can be found in Table 7: Step 4 - 9. It is worthy to note that the temperature of the baths should be monitored carefully so that the waveguides do not get deformed due to *CYTOP* thermal expansion as discussed in Chapter 2.2-2.

Step	Description	Details
1	load wafers into electron-beam metals evaporator	Vacuum chamber to below $2x10^{-6}$ *Torr*, deposit *35 nm* of gold with a rate of *2 nm/s*
3	Prepare two separate baths (1 & 2) of *Microstrip 1165* to strip resist layers	Pre-heat to *80 °C*
4	Immerse wafer in bath 1 to liftoff 90% of metal and resists	Static dip, *10 min.*
5	Perform ultrasonic agitation on wafer	10 sec.
6	Immerse wafer in bath 2 to liftoff remaining metal and resists	Static dip, *10 min.*
7	Perform ultrasonic agitation on wafer	*10 sec.*
8	Immerse wafer in isopropyl alcohol (IPA) bath	Static dip, *10 min.*
9	Immerse wafer in de-ionized (DI) water bath	Static dip, *10 min.*

Table 7: Metal and resist liftoff process

3.1-5 Bi-layer, Sidewall and Dimension Problems/Solutions

The fabricated device from following Table 6 and Table 7 were qualitatively checked for various factors. First, the bi-layer over-hang profile was examined under a scanning electron microscope (SEM) shown in Figure 23. We see that a thicker photoresist layer sits on top of the thinner liftoff resist layer. The liftoff resist sidewall is obviously recessed compared to that of the photoresist. This shows that the over-hang profile was properly constructed. This result was duplicated every time without any reoccurrence of the collapse of the triple waveguide features shown in Figure 22. This shows that the proposed spin, bake and development processes were robust and effective.

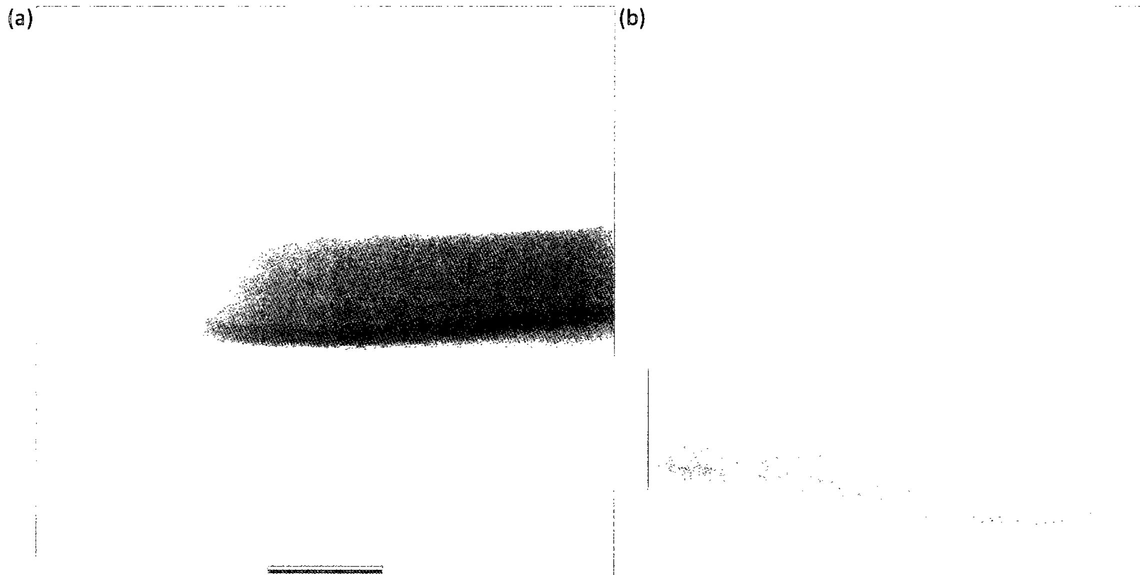

Figure 23: Bi-layer lithography development profile. (a) photoresist overhang (b) liftoff resist under-etch.

The second factor to be examined is the quality of the wall-edge profiles. During lithography trials, it was discovered that the patterned wall edges were rough and "bumpy"; as shown in Figure 24a. It was suspected that the cause of these rough edges is over-exposure from reflection of the silicon substrate through *CYTOP* claddings. From [38] we see that *CYTOP* is quite transparent in the UV spectrum, thus, any UV radiation incident on the thick *CYTOP* cladding will be transmitted and reflected without much decay in intensity. This effectively double exposes the resist, thereby resulting in rough edges from over-exposure. To solve this issue, the exposure time was carefully tuned through multiple trials to attain the optimum time for specific lamp intensities. This turned out to be *6 sec.* for UV intensities of $6.6m\ W/cm^2$ at *365 nm* and $12\ mW/cm^2$ at *400 nm*. An example of a well-tuned exposure lithography pattern is shown in Figure 24b where it is obvious that the rough edges have been eliminated.

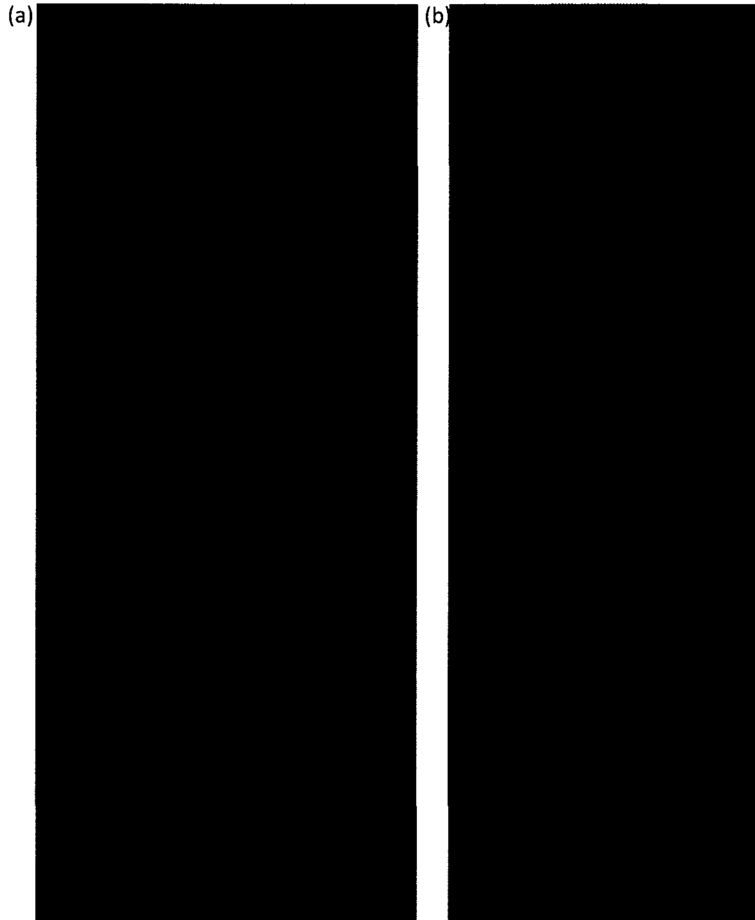

Figure 24: (a) rough edges caused over-exposure (b) smooth edges from correct exposure

The third quality check is dimension accuracy. To accomplish this, both the resist and waveguide patterns were examined with a microscope and SEM. It was revealed that even with the revised bi-layer process and tuned exposure time, the dimensions were still slightly off target. This is shown in Figure 25a, b and Figure 26a, b. The patterned stripes were narrower than the target feature sizes (*5 μm* stripes, *2 μm* spacings). The immediate solution was to increase the development time and etch the patterns wider. Thus, multiple trials were conducted to determine the proper development time. This turned out to be *1:40 min*. SEM inspections of the resulting photoresist pattern are shown in Figure 25c, d. The same pair of figures for metal devices is shown in Figure 26c, d. By placing the *1 μm* bars across the images, the dimensions were measured to be within the correct specifications. Further dimension

characterization was done through AFM measurements shown in Figure 28c, where it is again confirmed that the waveguides are 5μm wide.

The AFM measurements also served as a check for the metal thickness and surface roughness; which was *37 nm* and *0.92 nm RMS* respectively. The metal thickness was about *5%* thicker than the target *35 nm*. This can be fixed by adjusting the deposition instrument's controller sensor to compensate for the overshoot. The metal's surface roughness is very similar to the *CYTOP* lower cladding roughness of *0.82 nm RMS* mentioned in Chapter 2.2-3. The metal roughness is still less than the requirement of *<1 nm*. This suggests that the metal deposition process is a very surface-smooth procedure. It should be noted that the precision of the metal thickness and roughness is limited by the performance of the e-beam evaporator. No further manual adjustment could be made to improve this instrumental precision.

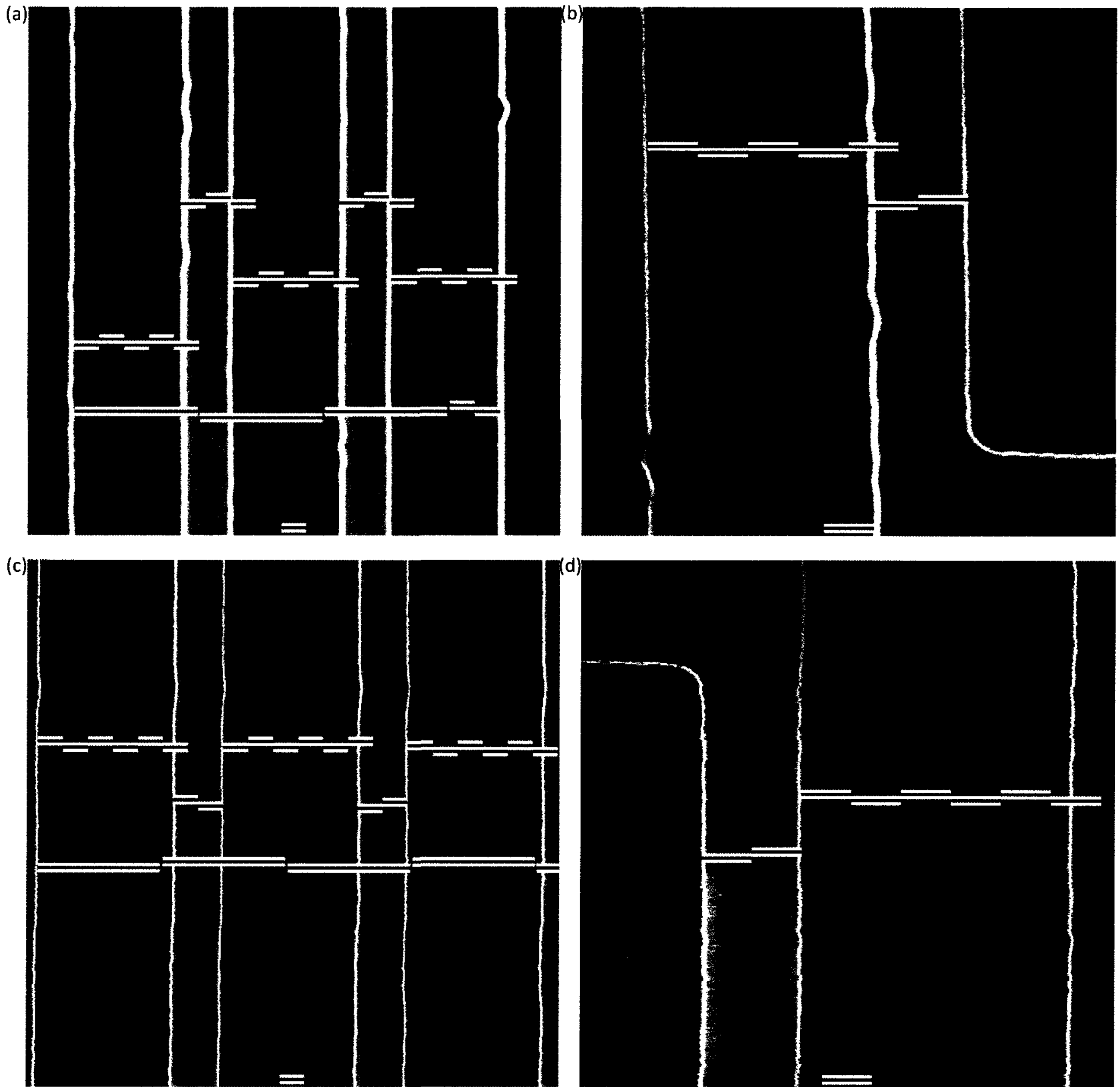

Figure 25: Post-development lithography SEM dimension profiles. Short bar markers = *1* μm, long bar markers = *5* μm. (a), (b) under-development etch. Waveguides = 4.3 μm. Spacings = *2.1* μm. (c), (d) correctly tuned development etch. Waveguides = 5.2 μm. Spacings = 2 μm.

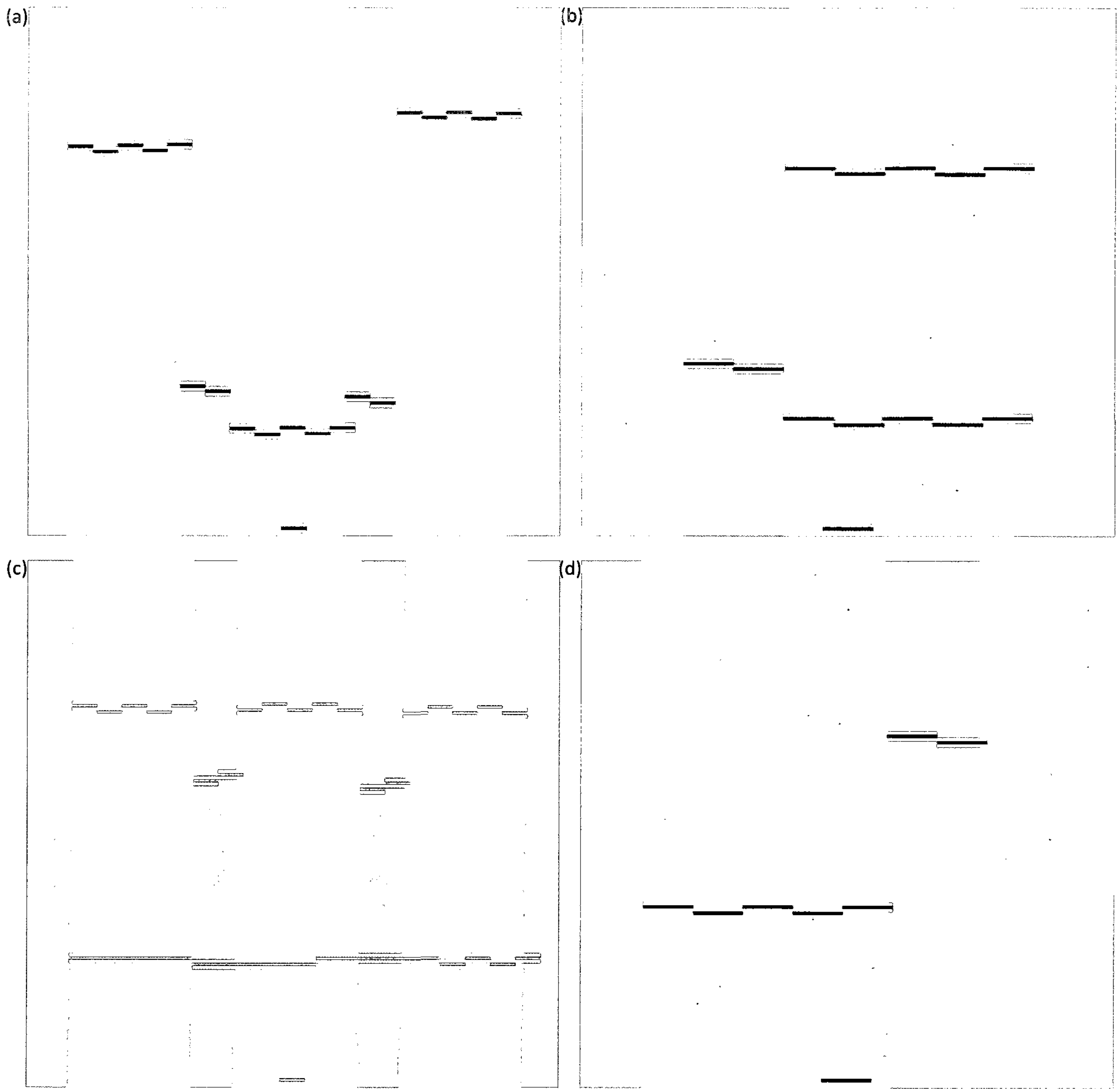

Figure 26: ***Au*** **stripe waveguide SEM dimension profiles. Short bar markers =** ***1 µm*****, long bar markers =** ***5 µm*****. (a), (b) under-development etch. Waveguides = 4.6** ***µm*****. Spacings =** ***2.0 µm*****. (c), (d) correctly tuned development etch. Waveguides = 5.1** ***µm*****. Spacings = 2.2** ***µm*****.**

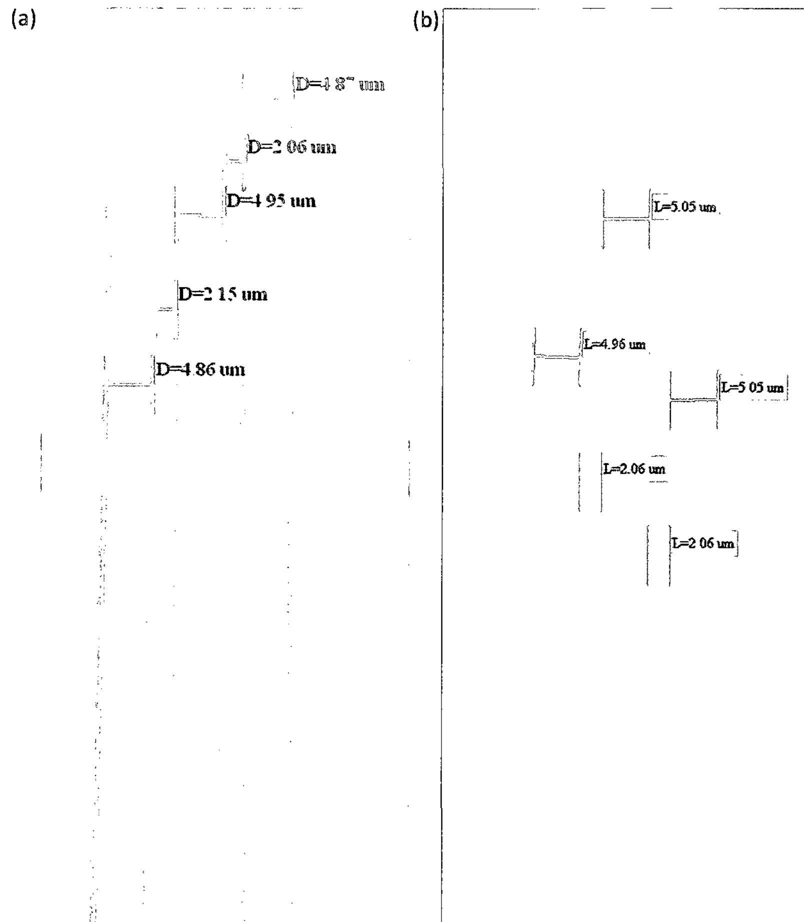

Figure 27: Microscope dimension measurement –correctly tuned. (a) post-development lithography pattern (b) *Au* stripe waveguides

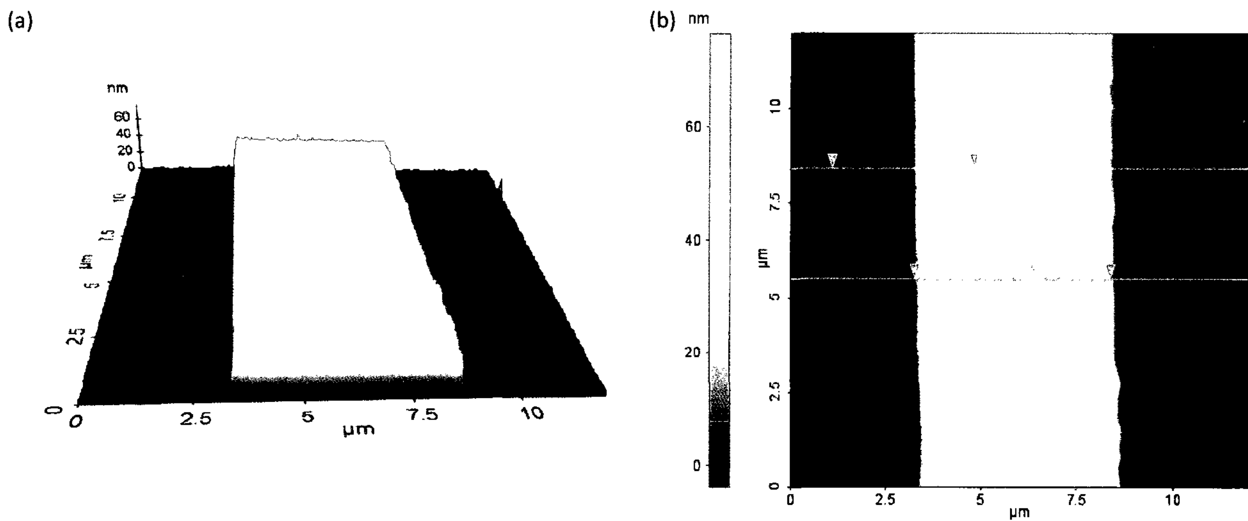

(c)

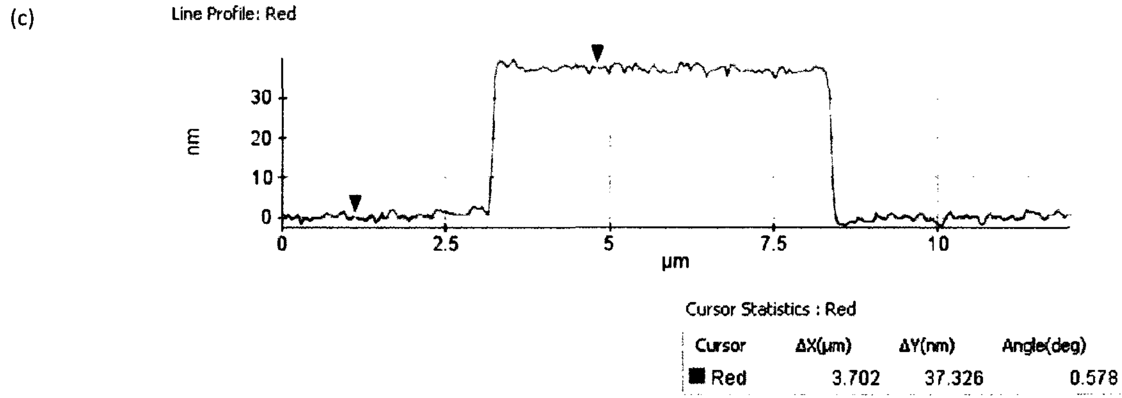

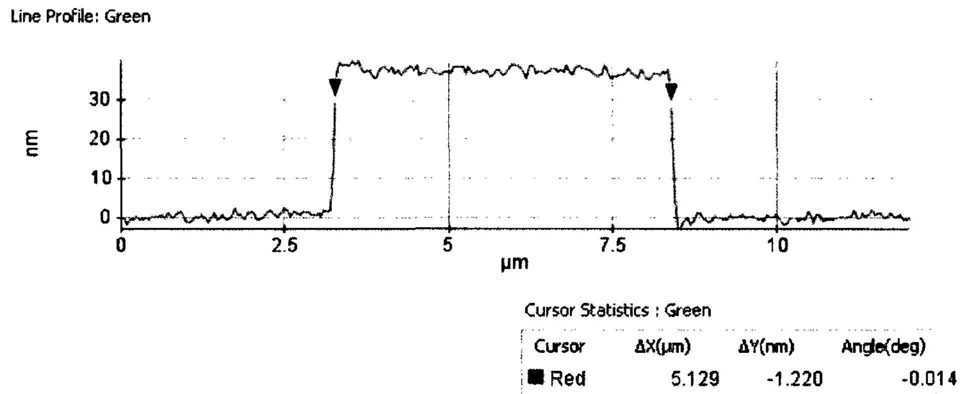

(d)

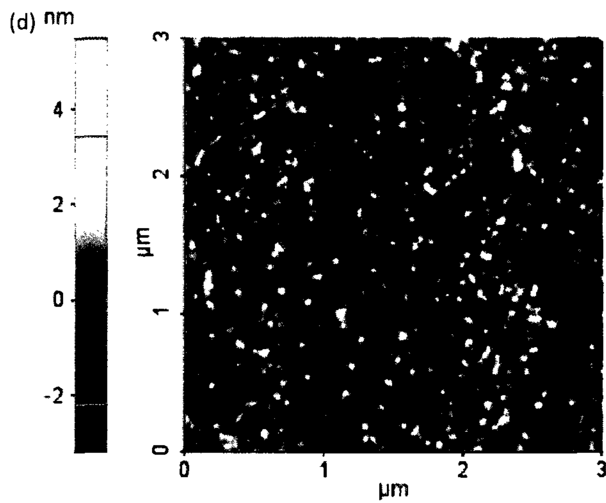

(e)

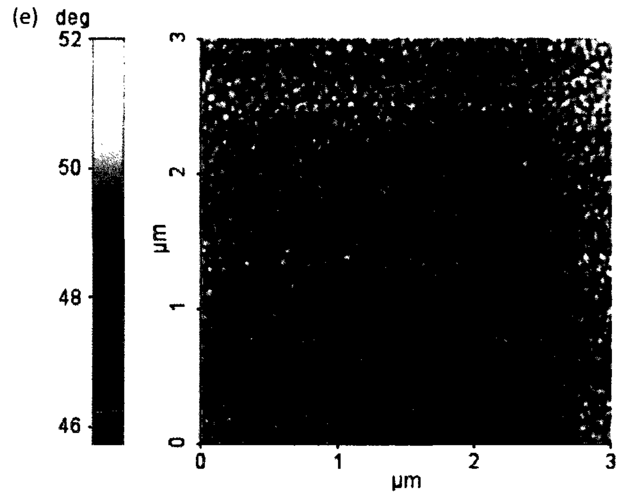

Figure 28: AFM surface and dimension profiles of *Au* stripe waveguides. (a) 3-D visualization. (b), (c) 2-D surface profile scan. (d) *Au* surface amplitude measurement. Roughness = *0.92 nm* RMS, *0.72 nm* average. (e) *Au* Surface phase shift measurement

3.2 Channel Lithography

3.2-1 Layout and Mask

The lithography step for creating microfludic channels follows after the top *CYTOP* claddings have been coated as explained in Chapter 1.4. The purpose behind this second level of lithography is to pattern selective arms of the MZI devices and then expose them from the top cladding through plasma etching. This is a necessary step for biosensing because the exposed waveguides can then be functionalized and immersed in buffer aqueous solutions. Microfluidic channel masks were designed with the commercial software DW-2000. This is shown in Figure 29 with the first level devices overlaid on top of the proposed openings. Four types of patterns were designed for each die: no openings, one arm open, two arms open separately and two arms open together. The MZI with no openings are completely embedded in *CYTOP* and cannot be used for sensing. These devices are present for embedded waveguide optical characterization. The MZI with one arm open has the advantage of being physically isolated from the sensing fluid. This provides for convenient surface chemistry since no device selectivity is required. The MZI with both arms requires more complex steps when applying surface chemistry to only the sensing arm. However, since both arms will be submerged in the sensing fluid, the output is protected from differential changes in the environment of each arm. The variety of having separate and combined openings is present for studying liquid flow effects. In addition to interferometric devices, straight waveguides were also patterned to be exposed. This was done for optical characterization tests on waveguide performance in *CYTOP* and the sensing fluid (Chapter 5). The singly exposed channels are all *55 μm* in width; the length varies between *1.231~1.631 μm*

(a)

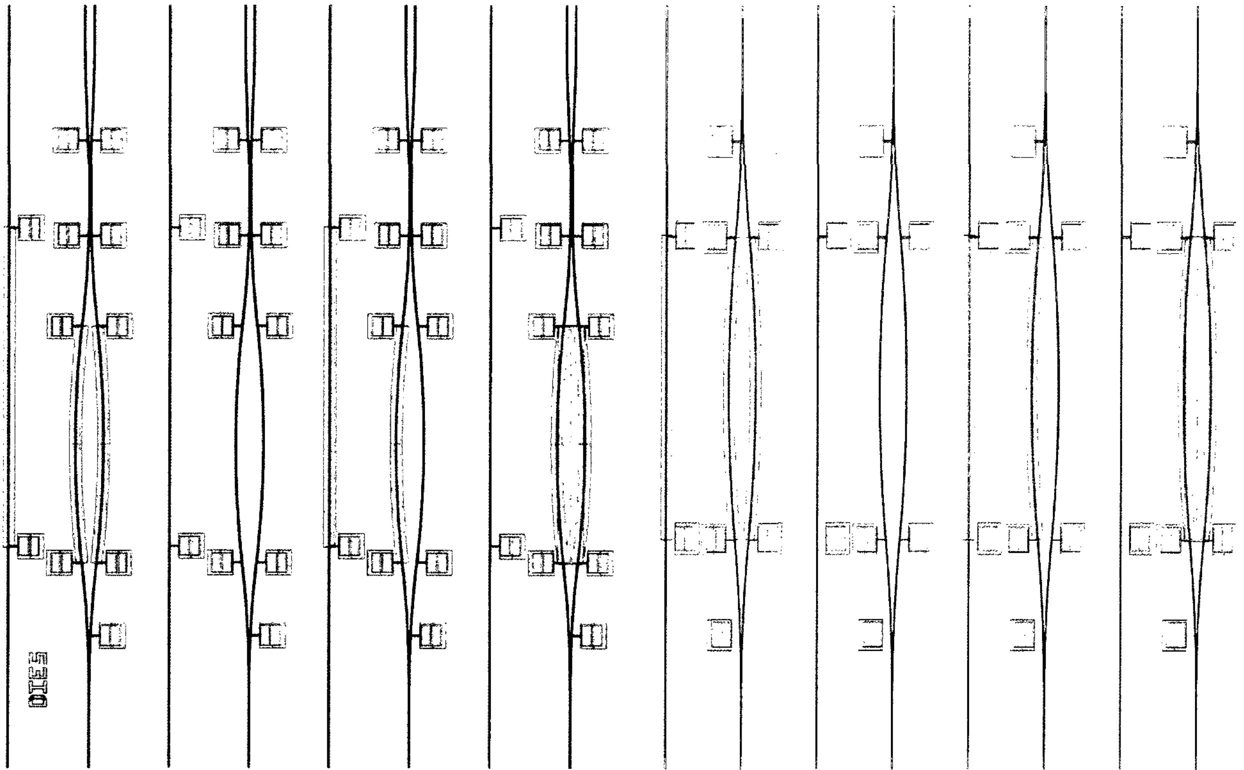

(b)

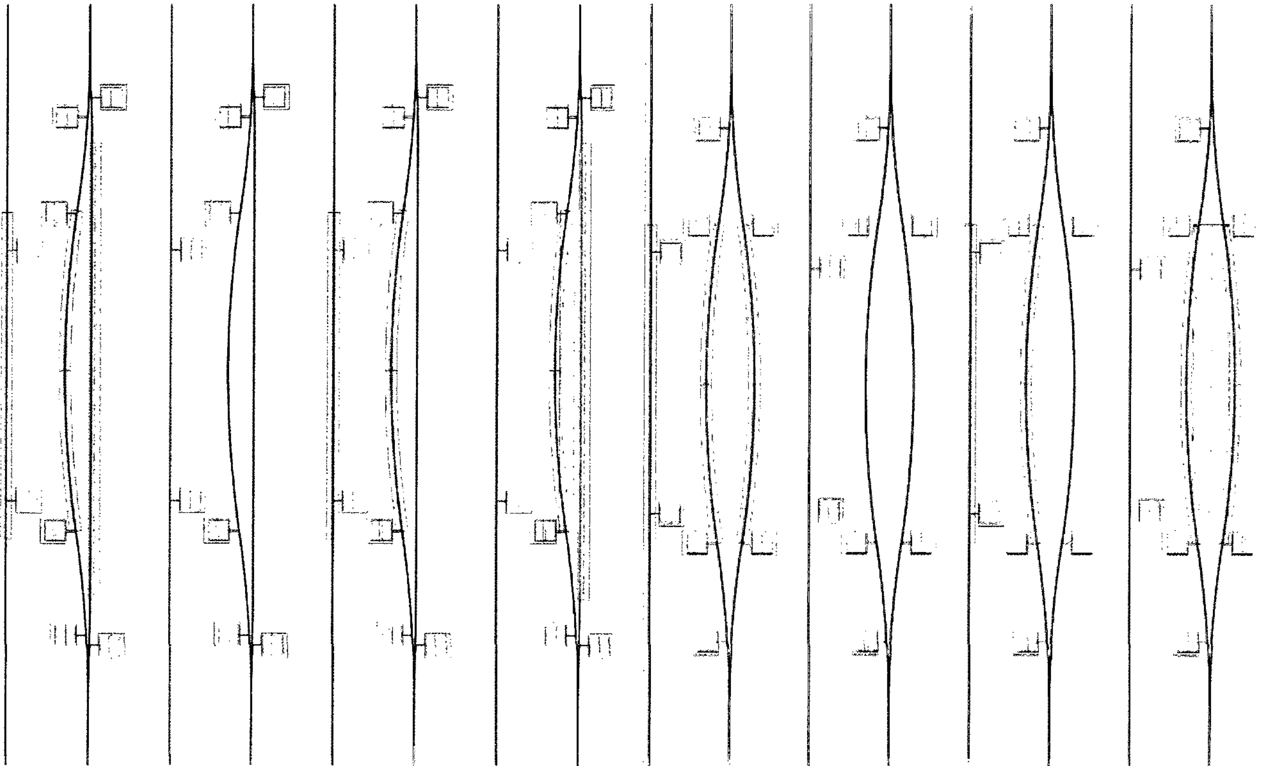

(c)

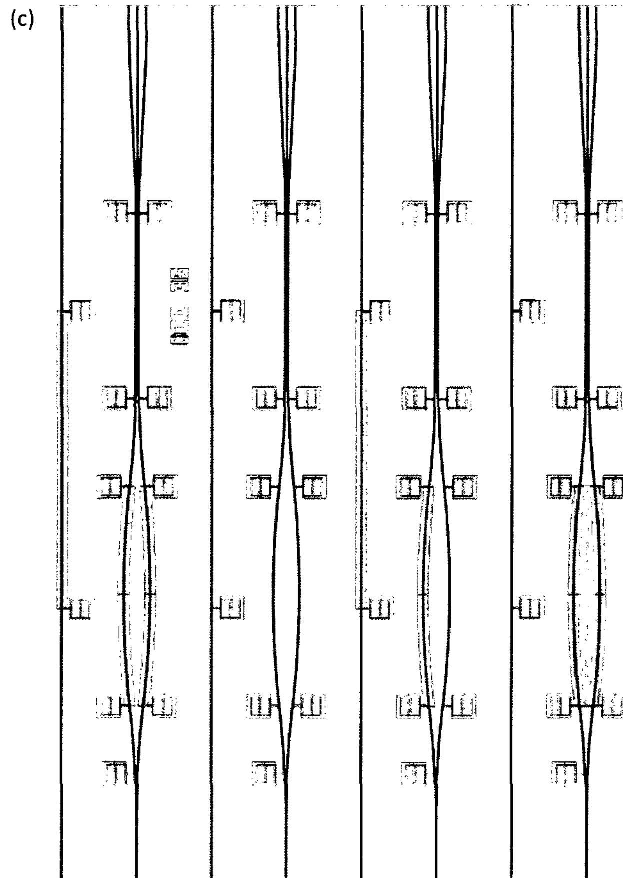

Figure 29: (a) *3.0* mm devices, *1.236 mm* channels (b) *3.8 mm* devices, *1.613* mm channels (c) *4.8 mm* devices, *1.613 mm* channels

(a)

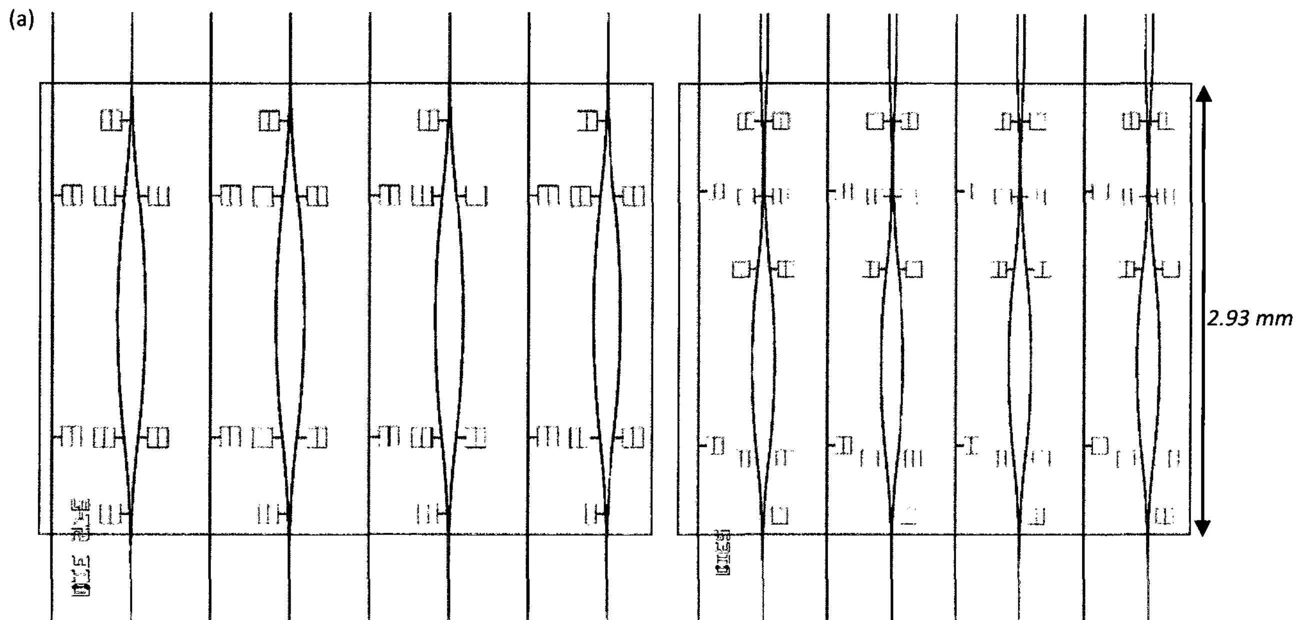

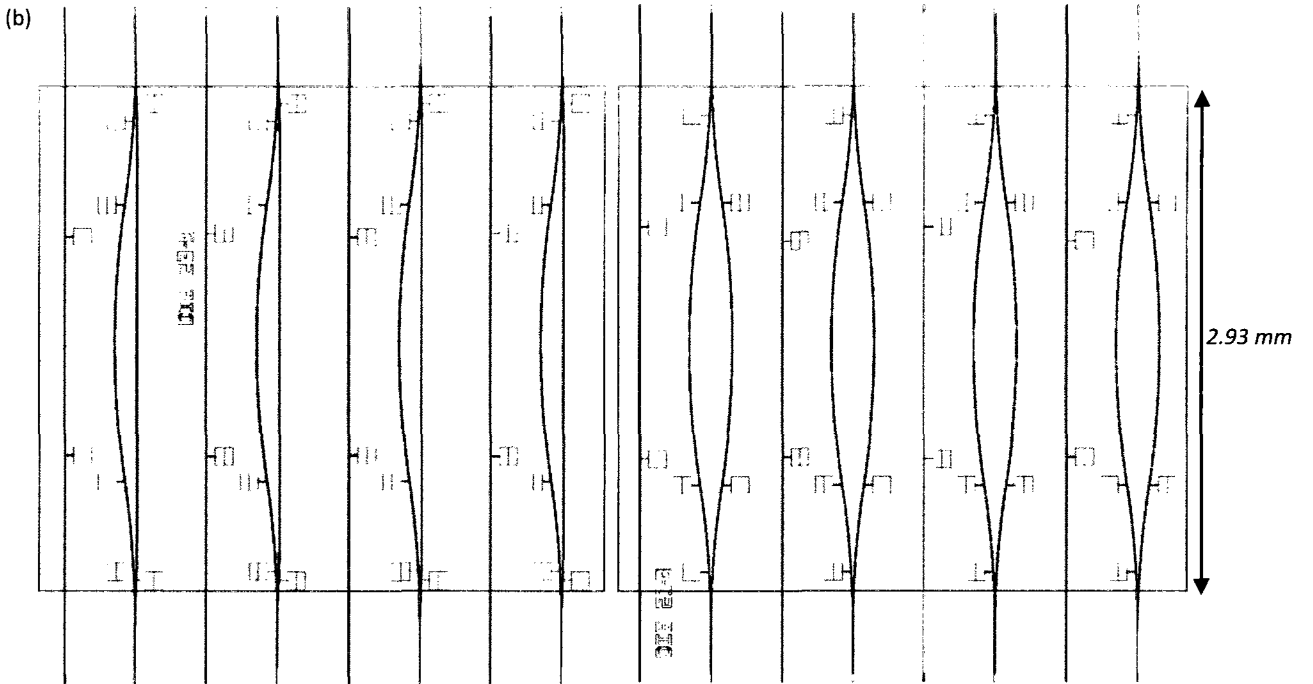

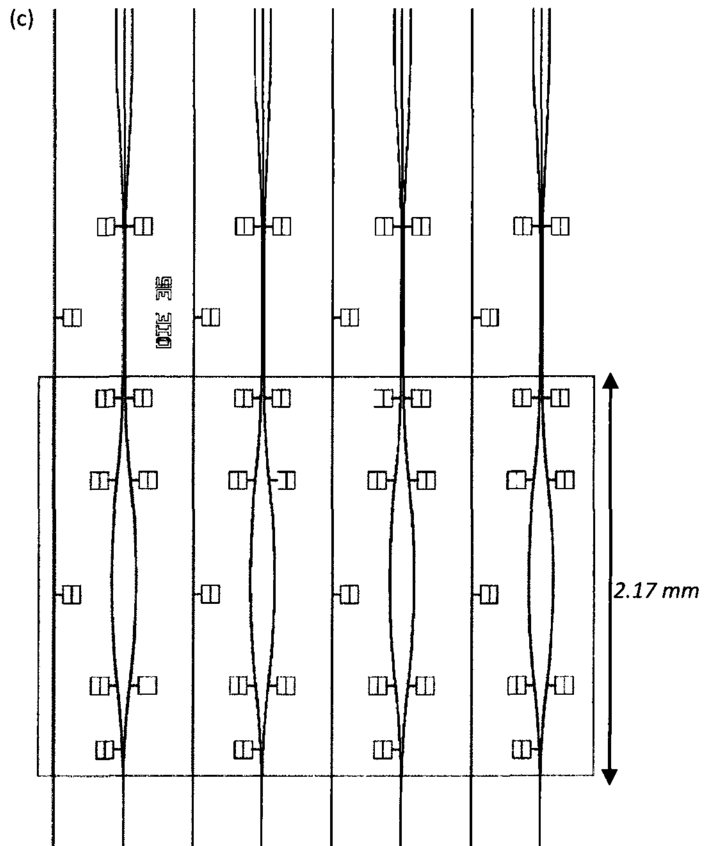

Figure 30: (a) *3.0 mm* devices, *2.93 mm* cavities (b) *3.8 mm* devices, *2.93 mm* cavities (c) *4.8 mm* devices, *2.17 mm* cavities

A second mask was also designed for simple optical characterization experiments. The pattern on this mask is basically a large rectangular cavity spanning across multiple devices. The lengths on these cavities range from *2.174~2.931 μm* (Figure 30). It should be noted that it is crucial to properly align the openings to the devices underneath because it is advantageous, from a experiment control point of view, to keep all exposed waveguide lengths and locations equal. Therefore, alignment marks were patterned in four opposite edges of the wafer to ensure correct alignment.

3.2-2 Channel Level Lithography Process

From Chapter 2.2-3 we know that the thickness of the top *CYTOP* cladding is approximately *9 μm*. Some preliminary etch trials were conducted with the same type of photoresist (*S1800* series) used in the device lithography level. The largest thickness attained for one spin coat was *2 μm*. This thickness was insufficient for the *9 μm* etch of top *CYTOP* cladding. In an attempt to make the resist thicker, more resist layers were coated. However, it was revealed that multiple layers yielded bad exposure /development results. This is because each layer must go through a *105 ^{0}C* soft-bake for *1 min.* Thus, the bottom-most layer would likely have gone through four soft-bakes in total. This effectively hard-baked the photoresist and made it less photosensitive to UV-exposure. It was clear at this point that a different photoresist should be utilized for this application. Hence, the photoresist SPR-220-7 was chosen because it was possible to coat above 15 μm with one spin. Several experiments were conducted to obtain a procedure which yielded a 9 μm thick resist layer. This process is outlined in Table 8; which was derived from referencing the manufacturer technical sheets. Three prominent differences between the device level and channel level lithography were: two-stage soft-bake (Table 8-Step 5), lengthened exposure time (Table 8-Step 7) and post-exposure hold/hard-bake (Table 8-Step 8~9).

Step	Description	Details
1	Ash *CYTOP* wafer in O_2 plasma to roughen the surface	*5 sec.* for 2" wafers, *10 sec.* for 4" wafers
2	Spin coat hexamethyl disiloxane (HMDS) for resist adhesion	*1000 RPM* for *10 sec.*
3	Soft-bake on hotplate	*105 °C* for *1 min.*
4	Spin coat *SPR-220-7* for thick positive resist layer	*1000 RPM* for *30 sec.*, followed by *2300 RPM* for *10 sec.* (~*10 μm*)
5	Soft-bake on hotplate	*35 °C* for *30 sec.*, then *115 °C* for *90 sec.*
8	load microfluidic channels mask (2nd level) in mask aligner	Align markers to flat of wafer
7	UV Exposure	*70~80 sec.* for thick, ~*9 μm* top cladded *CYTOP* wafers. Exposure time adjustments depend on thickness of *CYTOP* wafer and current lamp intensity
8	Photo-reaction hold	Let sit at room temp. for *2 hr.* to allow water to diffuse back into photoresist film.
9	Post-exposure hard-bake	*115 °C* for *90 sec.*
10	Development in *MF-24A*	*1'20 ~ 2 min.* with strong agitation.
11	Inspection	Check alignment under microscope. Look for colour fringes that suggest incomplete etching of resist.

Table 8: Microfluidic channel lithography process

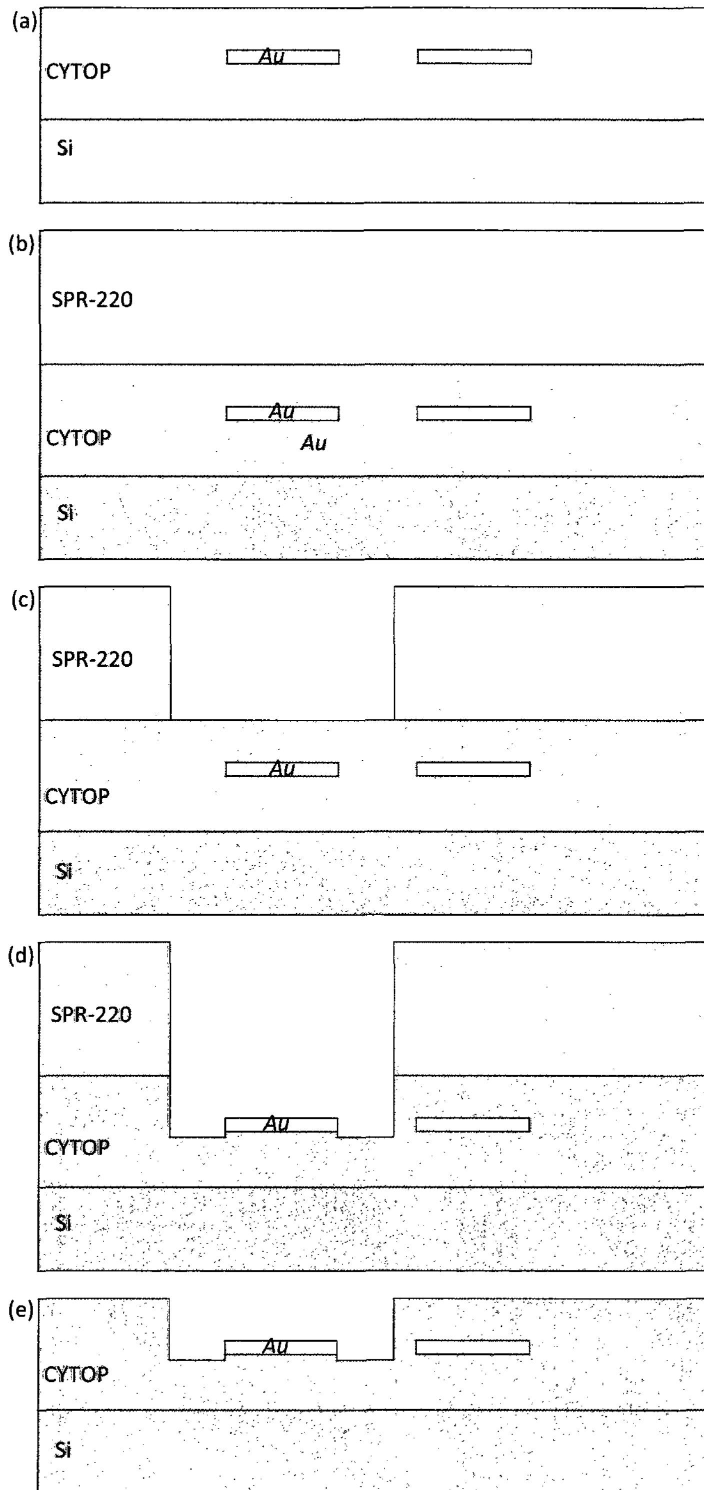

Figure 31: Process diagrams for microfludic channel lithography and etch (a) *Au* devices embedded in *CYTOP* (b) *SPR-220* (photoresist) coating (c) microfludic channel pattern (d) O_2 cavity etch (e) resist strip

The soft-bake required a two-stage step-up in temperature from *35 °C* to *115 °C*. This was necessary because sudden thermal shock at *115 °C* resulted in the resist forming uneven "puddles" across the surface. It was suspected that this was due to uneven thermal distribution coupled with the high thickness and viscosity of the resist. Letting the resist to be baked at an intermediate temperature helped to slowly distribute heat evenly across the wafer. It was experimentally determined that *35 °C* for *30 sec.* eliminated the localized "puddles" completely. As per instructed by the manufacturer ([44]), the resist was then soft-baked at *115 °C* for *90 sec.* to prepare it for exposure.

Table 8 lists an exposure time of at least *70 sec.*, which is much longer than the device level exposure of *6 sec.* Naturally, this is a direct consequence of having a much thicker resist (*0.5 μm* versus *9 μm*). In order to determine this exposure time, multiple experiments were conducted. First, it was necessary to be sure that *SPR-220* was suitable for the same UV-exposure tool used for the device level resist (*S1800* series). Comparison of the resist photo-absorbance spectra between *S1800* series [46], and *SPR-220* series [44] showed that both spectra exhibit similar patterns. Specifically, local maximums were at found *350 nm* & *410 nm*, and a local minimum at *380 nm*. The only difference is the absorbance magnitude; which can be compensated by adjusting the exposure time. Having confirmed that the same UV-exposure tool can be utilized, arbitrarily timed exposure trials were conducted on samples between *50 sec.* to *2 min.* For each sample, the corresponding development time was recorded. The results are shown in Table 9. From this result, it is safe to conclude that exposure times above *70 sec.* were over-exposures, and the minimum amount of time required to develop the pattern completely is *1:20 min.* One of the difficulties in this experiment was to ensure that all the patterned resist have been etched away after development. Since the resist is very thick, it was possible to leave a residue layer of resist on top of the patterned openings. Therefore, the patterned openings were subjected to a roughness test using a surface profiler. The surface roughness between *CYTOP* and the photoresist is substantially different and it served as a good indication of completed development. A visual check can also be

performed by carefully checking for the existence of optical fringes or colour variations on the patterned surface.

Wafer ID	UV Exposure Time (sec.)	Development Time (min.)
CLT 10a	45	5'00
CLT 10b	50	3'00
CLT 10c	55	2'00
CLT 10d	60	2'20
CLT 9a	70	1'20
CLT 9b	80	1'20
CLT 9c	85	1'10
CLT 9d	90	1'10

Table 9: *SPR-220* exposure-development trials. UV lamp intensities: *6.6 mW/cm²* at *365 nm* & *12 mW/cm²* at *400 nm*

In between exposure and development, there is a photo-reaction hold time of *2 hr.* and then a post-exposure bake at *115 °C* for *90 sec.* This step was followed in direct accordance to the manufacture technical sheets. The explanation provided was that thicker resist required a longer hold time in order for water to diffuse back into the film and complete the photo-reaction process [44]. No specific explanation was provided regarding the necessity of the post-exposure bake. However, it was observed that bypassing the two recommended steps yielded longer or incomplete development etches.

3.2-3 Post Development Check

The quality check conducted for channel-level lithography was the wall-profile of the resist after the development etch. The thickness was measured on several samples with a surface profiler and showed consistent results around *10 μm*. The wall-profile was examined under SEM shown in Figure 32. We can see that the sidewalls have an inclined slope, and the edges are a bit rough. However, this did not turn out to be an issue for the ensuing plasma etch process as it will be explained in Chapter 4.

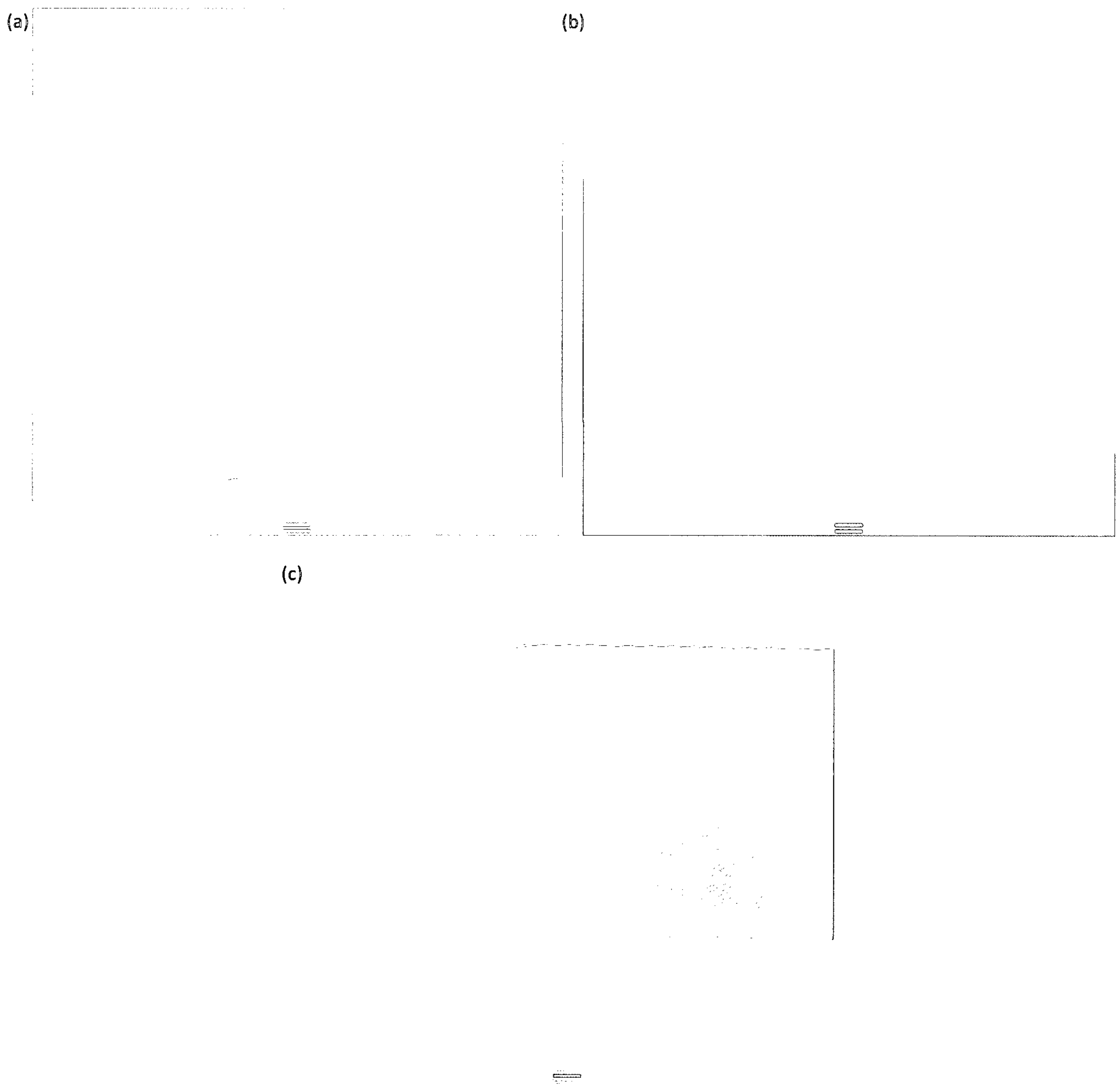

Figure 32: Post-development SEM structure profile of *SPR-220* (a) vertical sidewall view (b) 3-D sidewall view (c) patterned corner

4. *CYTOP* Etching

4.1 CF_4/O_2 Etching

4.1-1 Etch Rate Tests

In order to deliver sensing fluids to the waveguide devices, the top cladded *CYTOP* must be removed to expose the sensing waveguide arms. The resulting opening would then serve as the main structure for microfluidic channels. One way of removing *CYTOP* is to dry etch it with plasma as shown in Figure 31d - e. Reported work on etching *CYTOP* with O_2 and O_2/CHF_3 can be found in [43]. A similar set of experiments were performed on *CYTOP* wafers to determine the etch rate of *CYTOP* with O_2 and CF_4/O_2. Etching was performed with anisotropic RIE plasma.

In an attempt to create a fast etch process, CF_4/O_2 etch rate experiments were first conducted. This set of experiments had to be done on actual patterns and consistent wafer sizes. This is because reactive gas etching is known to have a loading effect dependent on the material to be etched. Therefore, the etch rate experiments were conducted on separate equal sized wafers which were all fabricated at the same time. The ratio between CF_4 and O_2 was not adjustable because we had access only to pre-mixed gas cylinders. The only factor which was adjustable was the flow rate and maximum RF power. In this case, the chosen RF power was set to 200W where it is known to be sufficient to maintain the plasma [48]. The etch rate results for different flow rates can be found in Figure 33. This was done by taking separate, but identical wafers, and subjecting them to different etch times at each arbitrary picked flow rate. The resulting *CYTOP* thickness was then measured with the prism coupler tool mentioned in Chapter 2. By fitting the data and observing the slope (etch rate), it is safe to conclude that the there is a range of flow rates *(10~40 sccm)* where the etch rate remained relatively the same. But when the flow rate is too high (*80 sccm*), it will start to drop.

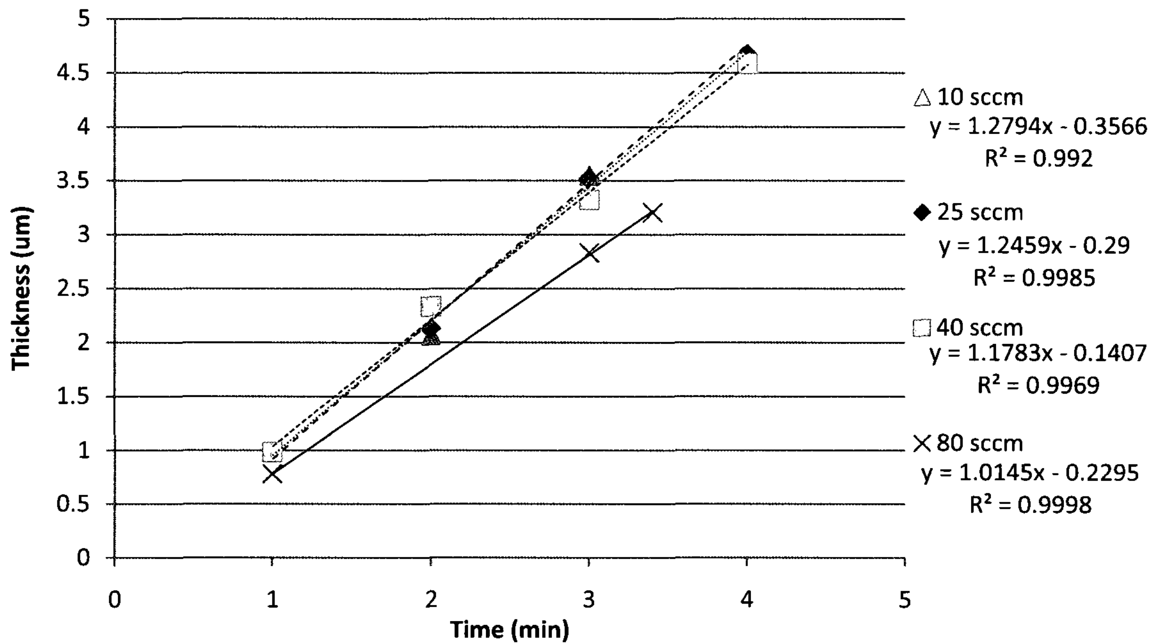

Figure 33: CF_4/O_2 etch test on *CYTOP* with varying etchant flow rate

4.1-2 Etch Profile

The etched wafer was then examined under the SEM to view the etch profile for both the photoresist and the *CYTOP* openings. The etched photoresist profile can be seen in Figure 34. This image revealed a very unusual profile where the etch seemed to be "eating" into the sidewalls centered at the interface between the *CYTOP* and the resist. According to Figure 35 it is suspected that the etch chemistry may be hostile to *CYTOP*. Etch profiles of the CTYOP opening (after resist removal) can be seen in Figure 35. The sidewalls have an obvious slope, and it is obvious that this is not a suitable etch process to create deep, rectangular channels. Further etch experiments using CF_4/O_2 as an etchant was not conducted because it is beyond the scope of this thesis to perform detailed study of the etch dynamics between *CYTOP* and CF_4/O_2.

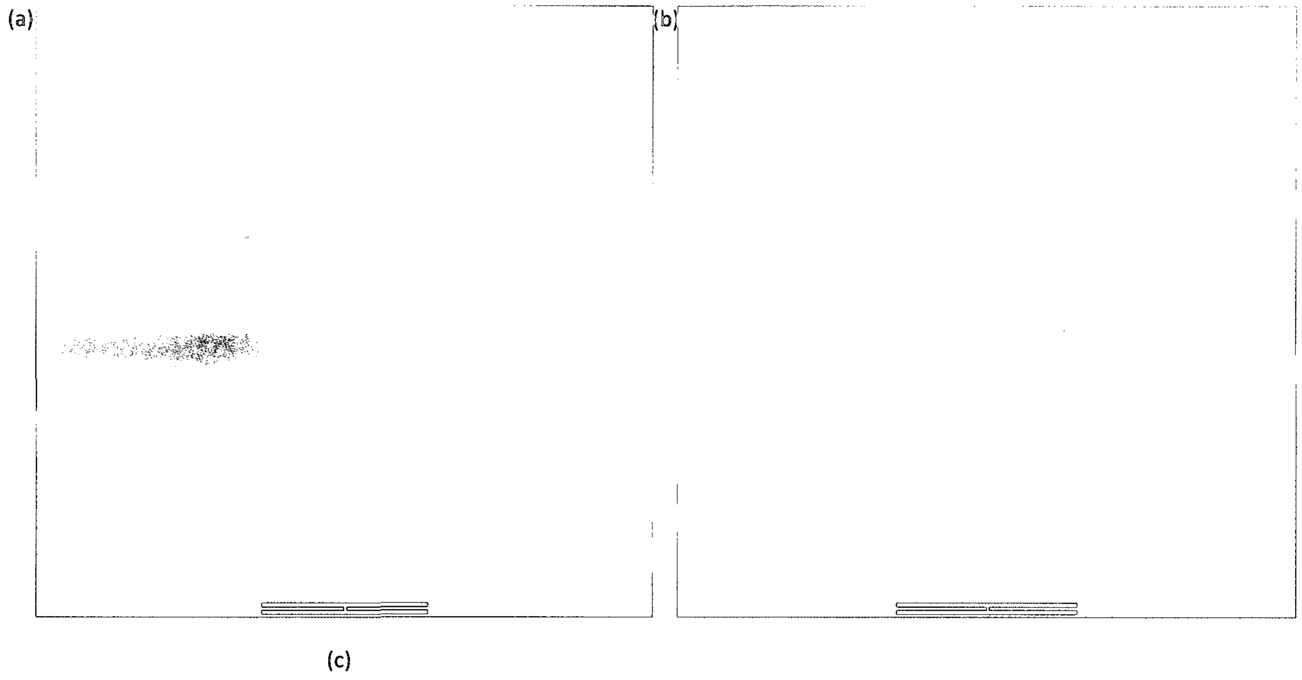

Figure 34: (a), (b) CF_4/O_2 etch SEM profile with resist of vertical sidewall view (c) patterned corner

(a)

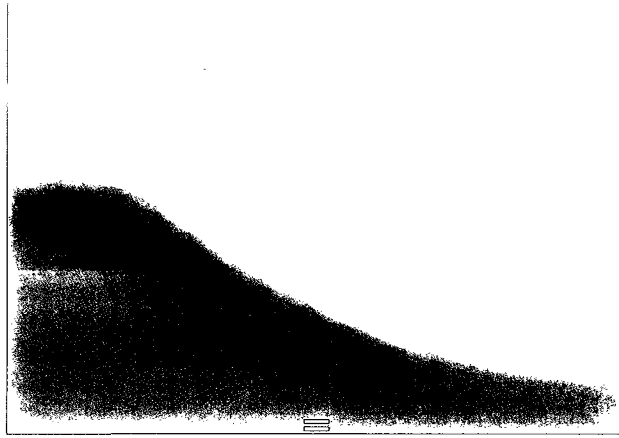

(b)

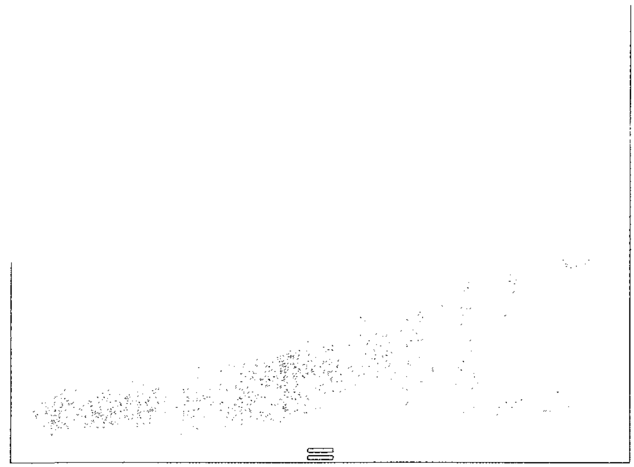

(c)

Figure 35: (a), (b)CF_4/O_2 etch SEM profile with resist removed of vertical sidewall view (c) patterned corner

4.2 O_2 Etch

4.2-1 Etch Rate Test

Pure O_2 etch experiments were conducted in hopes of creating a more anisotropic etch result. According to [43], an O_2 etch can be done, but it is slower without reactive ions. However, it was worth investigating what the actual etch rate and etch profiles would be. Following that, etch experiments were done on separate wafers with equal flow rate (*100 sccm*) and power (*200 W*). These parameters were chosen arbitrarily based on known factors of maintaining stable O_2 plasma. The results are shown in Table 10, where the etch rate averages to be around *0.92 µm/min*.

Wafers ID	Etch Time (min)	Etch Thickness (µm): 5-point wafer average	Etch Rate (µm/min)
CWS12	8'15	7.55	0.915
CLT13	9'30	8.62	0.907
CWS13	9'48	8.95	0.913
CWS24	10'00	9.16	0.916
CWS21	10'30	9.68	0.921
CWS19	11'30	10.37	0.902
CWS22	11'00	10.51	0.955
		Average Etch Rate (µm/min)	**0.918**

Table 10: Timed O_2 etch test on *CYTOP*. Thickness measured with surface probe profiler.

4.2-2 Etch Profile

The resulting etched wafers were again examined under SEM; shown in Figure 36 and Figure 37. This time, it was obvious that the etch profile was much more ideal. There appeared to be a slight slope on the sidewalls of the photoresist. However, this was already observed after the lithography step in Chapter 3-2.3. This sidewall slant did not affect the *CYTOP* etch as it is clear that the sidewalls are deep and anisotropic.

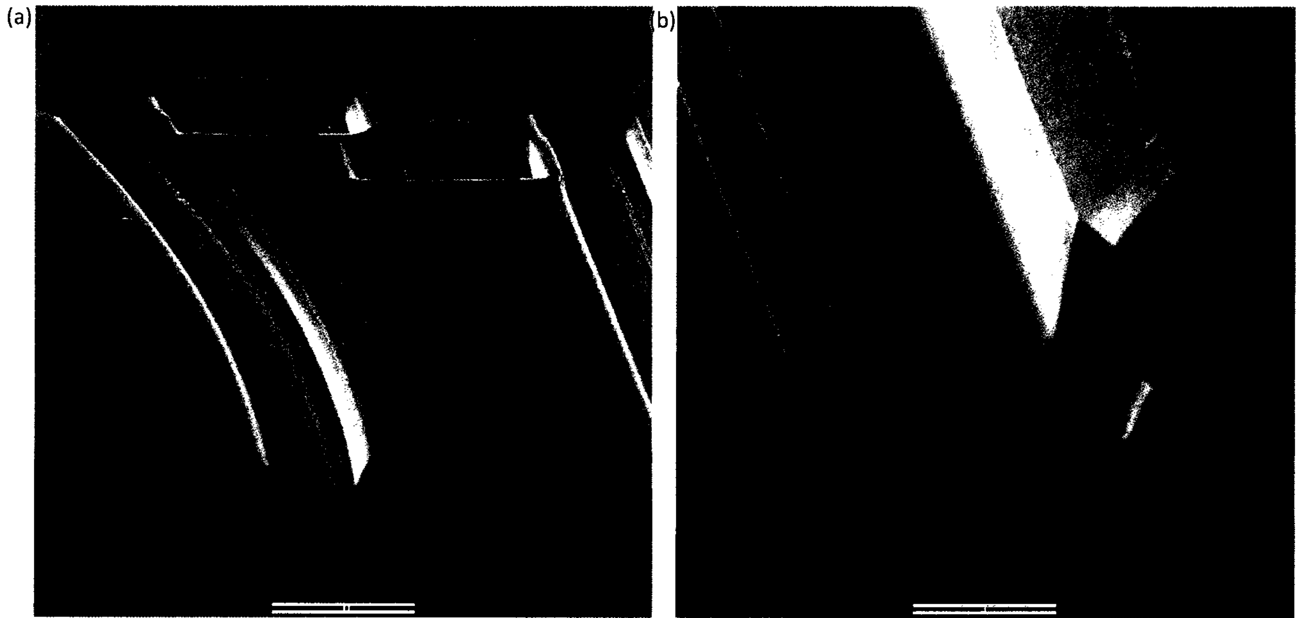

Figure 36: O_2 SEM profile with resist (a) overall device and channel view (b) etched sidewall view

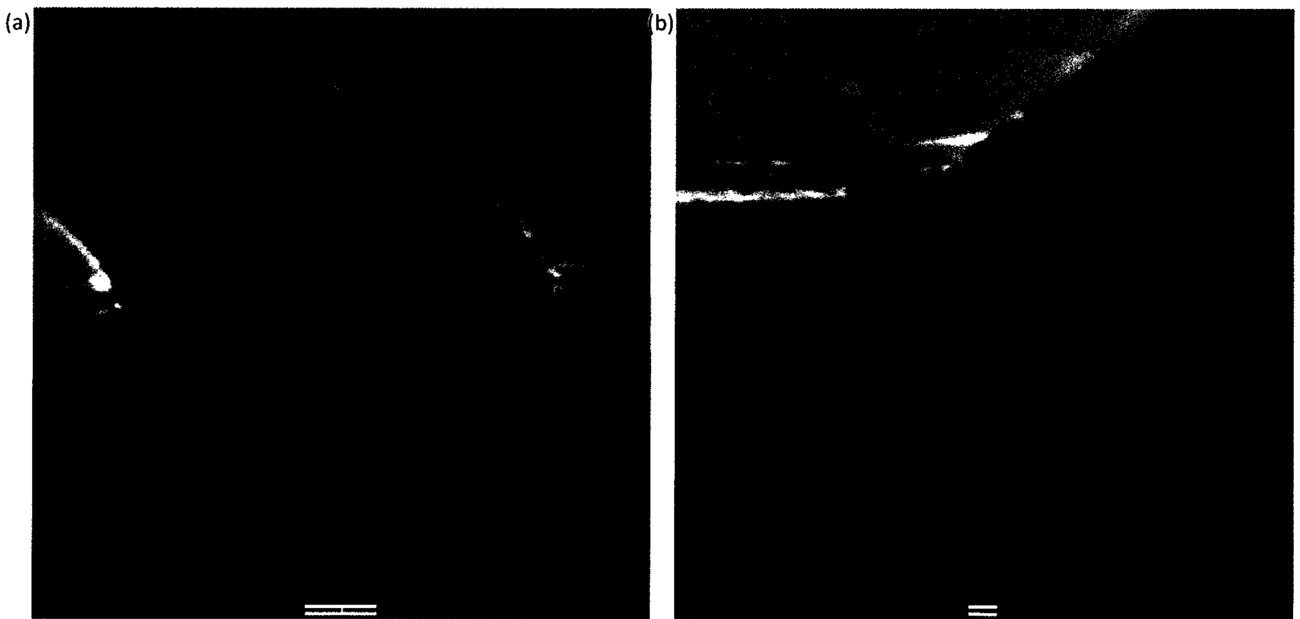

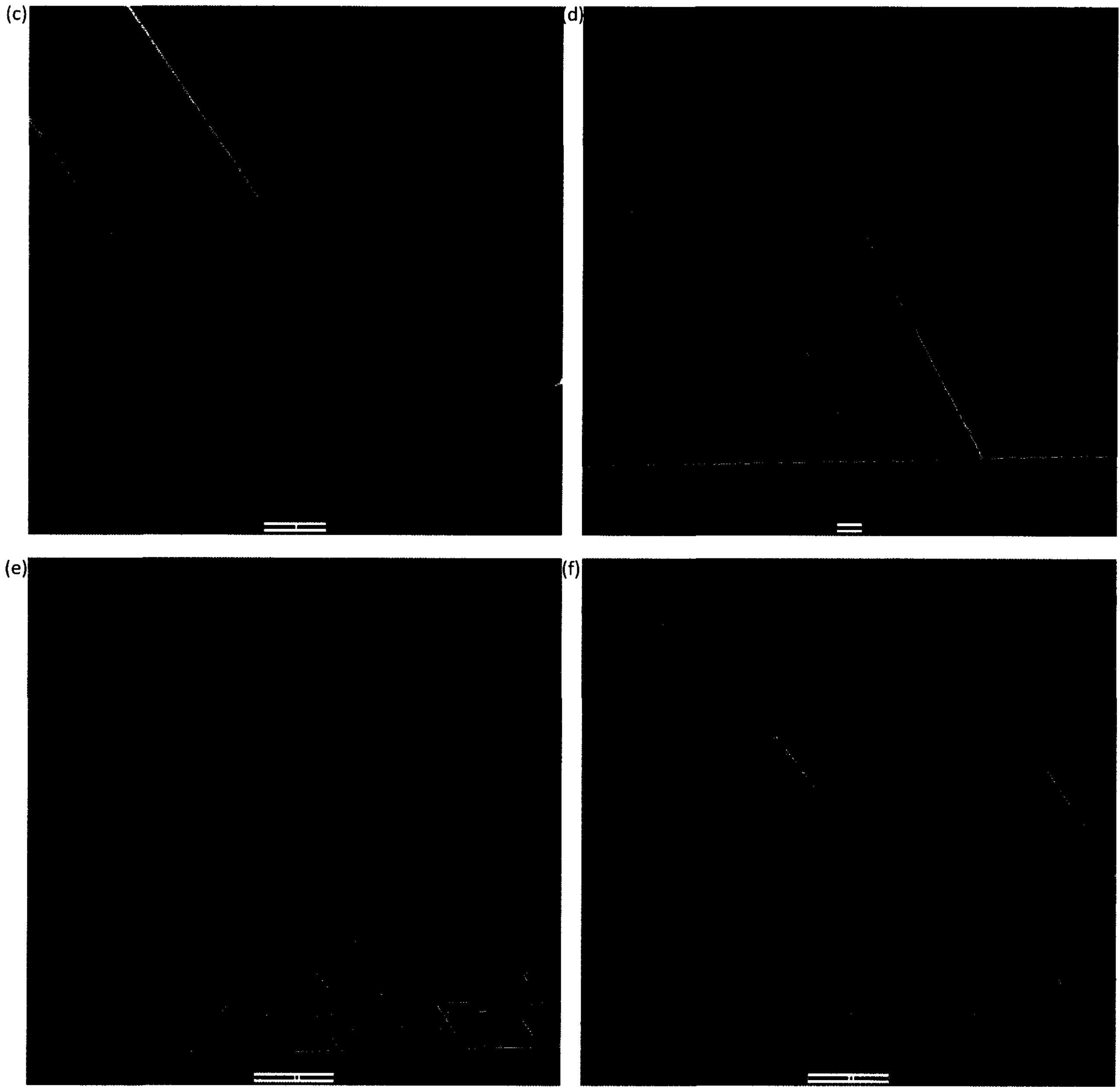

Figure 37: (a), (b) O_2 SEM profile with resist removed: vertical sidewall view. (c), (d) magnified waveguide view. (e), (f) overall device and channel view

4.2-3 Etch Quality Check

It is shown in Figure 37a that the waveguides have been exposed from the *CYTOP* claddings. However, the waveguides being visible at this scale means that the plasma has clearly over-etched the *CYTOP*. Intuitively, it is desirable to stop the etch at the instant the metal is exposed. This is very difficult

perform because the metal is only *35 nm* thick, while the etch rate is around *920 nm/min*. This means that the precision of the timed etch would have to be down to the seconds. Though this is not impossible to do, there are two other factors affecting the precision of the etch process: cladding thickness estimation and etch uniformity. It was discovered experimentally that the spin-coating of *CYTOP* to obtain a target thickness is accurate to within *0.05 μm*. In addition, the etch uniformity was discovered to vary by 0.5 μm. From propagating the two errors, it is most difficult to stop the etch process right after the waveguides have been exposed. From an optical point of view, the propagating mode will remain unaffected by the over-etch; since the *CYTOP* cladding is index-matched to the sensing fluid. What's more important is that the metal waveguides survive the etch process. This is a non-issue because metal does not get etched in O_2 plasma ([37]). However it is still desirable to control the etch process to reduce the over-etch as much as possible. The only way to accomplish this is to first allow the etch to stop at a safe under-etch time. It would be best to stop *1 μm* away from the point of release. Then, the etch would continue at *20 sec.* intervals. Each time the etch is stopped, the wafer would be subjected to a surface profiler examination to see if any of the waveguides have already been exposed. This procedure should be repeated until all the waveguides are exposed and hopefully, the over-etch would been brought to a minimal. The best result attained with this etch-and-check method is shown in Figure 38a with an average over-etch of *0.75 μm*.

A more ideal method of preventing over-etch is to create a thin etch stop layer (typically SiO_2) between the bottom and top *CYTOP* claddings. The direct undesired consequence is that this layer will be in the optical path of the LRSPP mode, thereby creating an asymmetric structure. This will potentially increase propagation attenuation, thus an etch stop layer was not used to prevent over-etch.

(a)

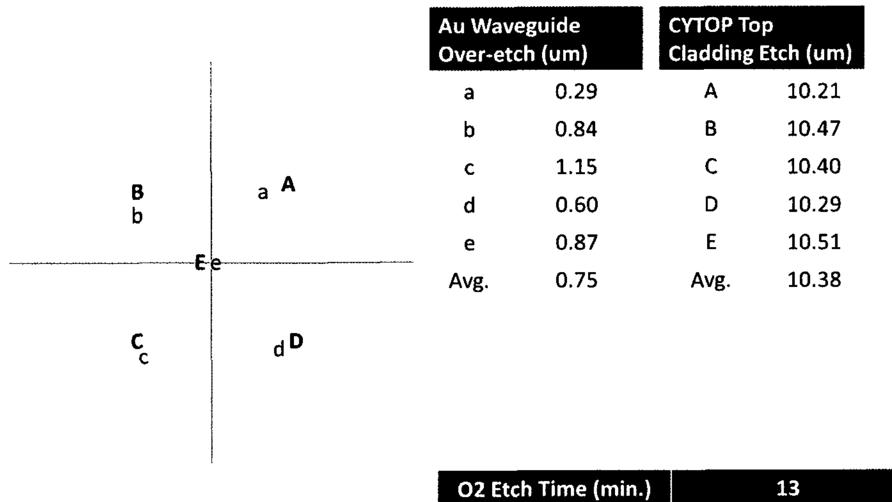

Au Waveguide Over-etch (um)		CYTOP Top Cladding Etch (um)	
a	0.29	A	10.21
b	0.84	B	10.47
c	1.15	C	10.40
d	0.60	D	10.29
e	0.87	E	10.51
Avg.	0.75	Avg.	10.38

O2 Etch Time (min.)	13

(b)

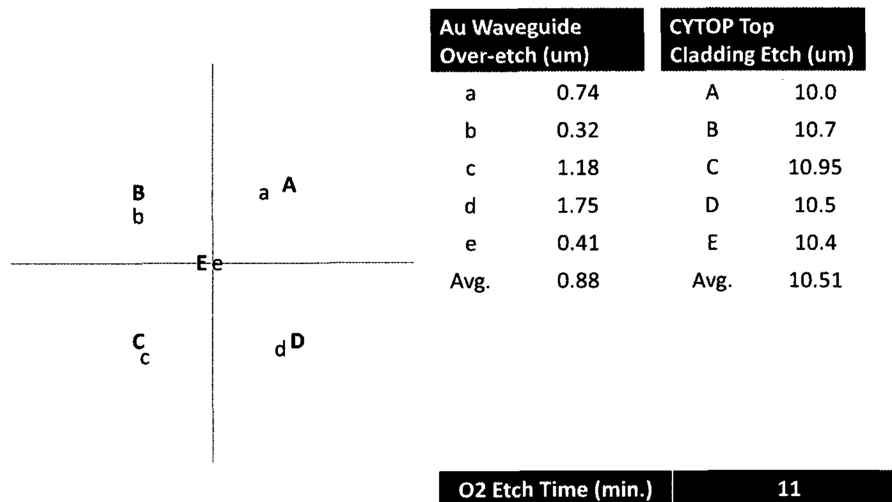

Au Waveguide Over-etch (um)		CYTOP Top Cladding Etch (um)	
a	0.74	A	10.0
b	0.32	B	10.7
c	1.18	C	10.95
d	1.75	D	10.5
e	0.41	E	10.4
Avg.	0.88	Avg.	10.51

O2 Etch Time (min.)	11

Figure 38: typical over-etch and uniformity of exposed *Au* devices

The etch exposed waveguides were examined with AFM. In Figure 39c, we see that the width of the waveguides remained the same with the design specification of *5 μm*. The over-etch for this die is *1.25 μm* which agreed with surface profile variations of the entire wafer as shown in Figure 38b. However, the contour of the waveguide is now curved, and not flat as seen in Chapter 3: Figure 28. Furthermore,

this curve has a peak height of ~*365 nm*, which is much larger than the deposited thickness of *35 nm*. One possible explanation of this leap in thickness is to attribute it to lower *CYTOP* swelling during the top cladding process. As mentioned before in Chapter 2.2-2 and seen in Figure 15, Figure 16, *CYTOP* will always be susceptible to its solvent. Thus, it is not hard to imagine that during the top cladding soft-bakes, the pressure of the evaporating solvent would push the waveguides up in the shape of the observed curvature. As a direct consequence, it remains impossible to determine the actual thickness of the metal since AFM captures the entire profile of metal and the over-etched lower *CYTOP* claddings. One other result from AFM is the surface roughness of the metal and etched *CYTOP* channels which is *8 nm* and *23 nm* respectively. This is shown in Figure 39d - g. This is in contrast to the non-etched wafer which was *0.92 nm* and *0.81 nm* (Figure 12a, Figure 28d). From visual inspection of the phase shift images, it appears that the surface is filled with "clumps" of material. This is most likely caused by etched *CYTOP* particles re-sputtering on itself and the waveguides. As mentioned before, since *CYTOP* and the sensing fluid are index matched, the presence of these *CYTOP* particulates will not affect the performance of the devices optically. However, if the waveguide surface is indeed filled with *CYTOP* particulates, then it is problematic when trying to functionalize the waveguides for sensing. For the scope of this report, it is sufficient to optically characterize the devices without chemical functionalization, thus no further work was done to eliminate the *CYTOP* particulates from the metal surface.

(a)

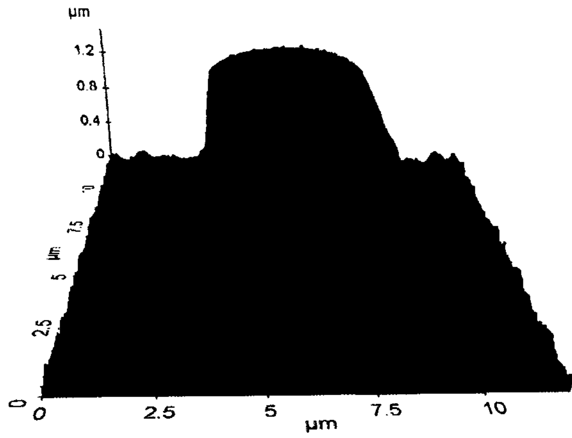

(b)

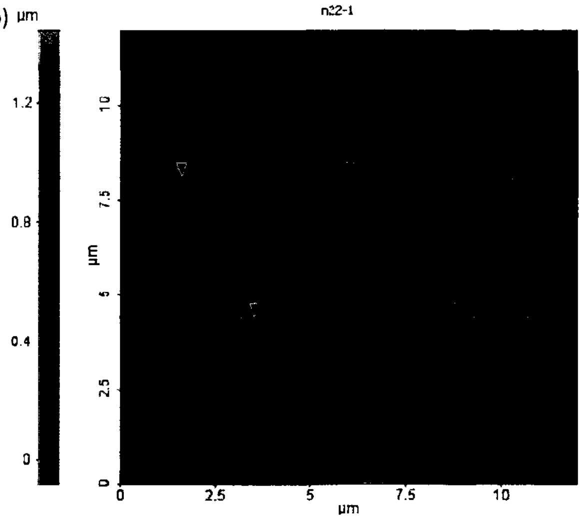

Line Profile: Red

(c)

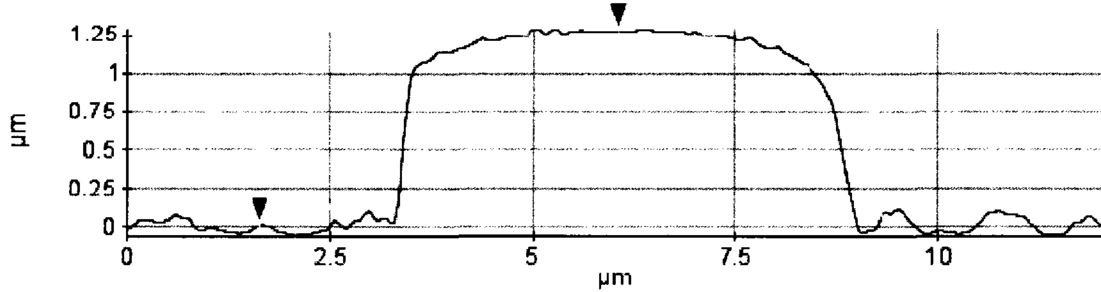

Cursor Statistics : Red

Cursor	ΔX(µm)	ΔY(µm)	Angle(deg)
■ Red	4.427	1.270	16.002

Line Profile: Green

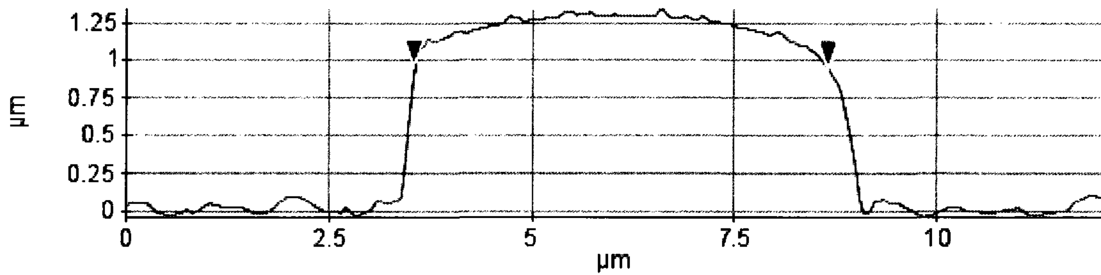

Cursor Statistics : Green

Cursor	ΔX(µm)	ΔY(µm)	Angle(deg)
■ Red	5.129	-0.010	-0.113

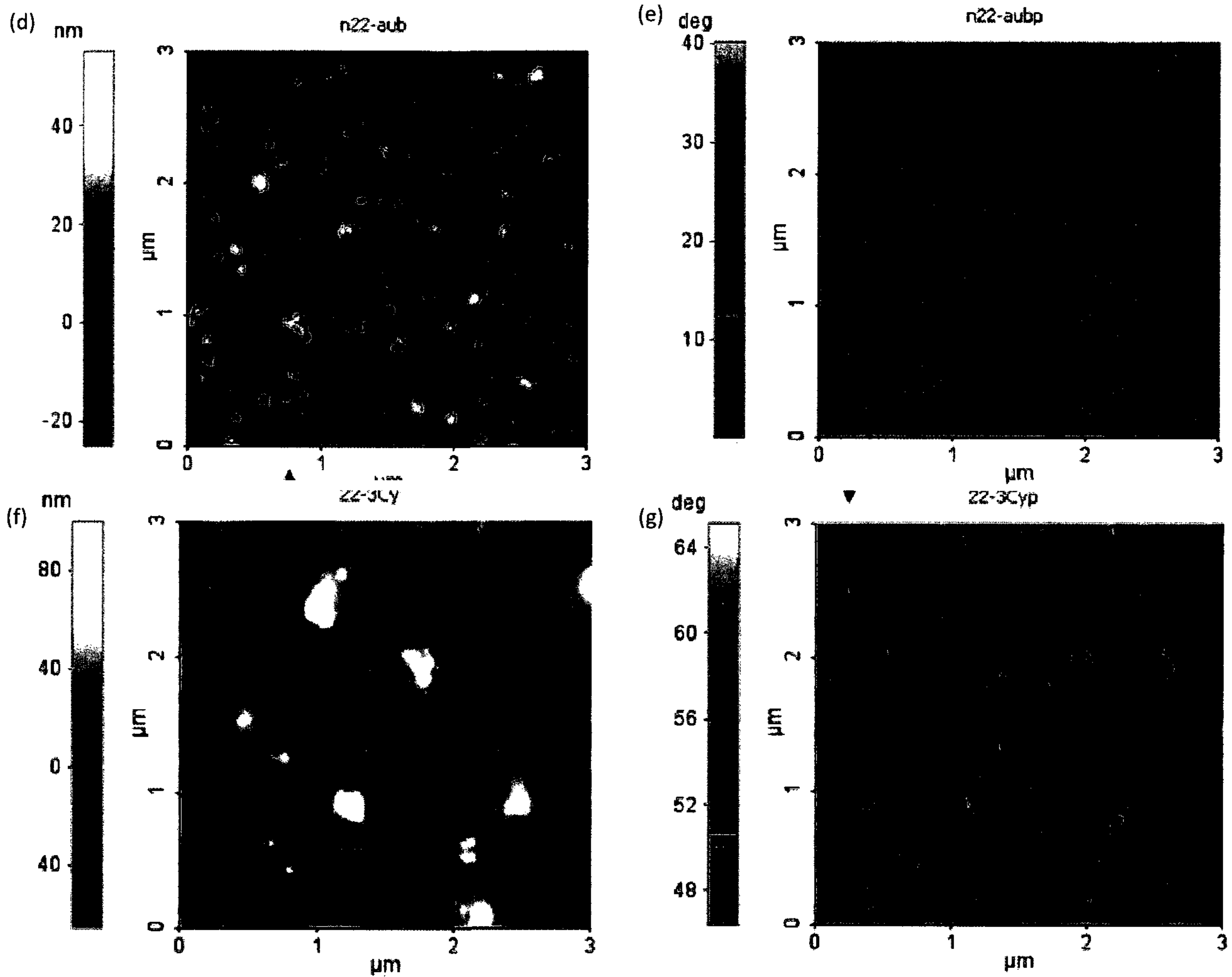

Figure 39: AFM surface and dimension profiles of *Au* waveguides and etched *CYTOP*. (a) 3-D visualization. (b), (c) 2-D surface profile scan. (d) *Au* surface amplitude measurement. Roughness = *8 nm* RMS, *5 nm* average. (e) *Au* Surface phase shift image. (f) *CYTOP* surface amplitude measurement. Roughness = *23 nm* RMS, *18 nm* average. (g) *CYTOP* Surface phase shift image.

4.3 Final Devices

The successful etch of the microfluidic channels mark the end of the fabrication process for LRSPP *Au* waveguide biosensors. Recall that the process details presented in this thesis are not in sequential fabrication order. The actual process steps were outlined in Table 1. Nevertheless, the process details in this chapter coincide with the last channel etching step. Thus it is appropriate to present microscope inspections of the final devices before proceeding to optical characterizations. These are shown in Figure 40.

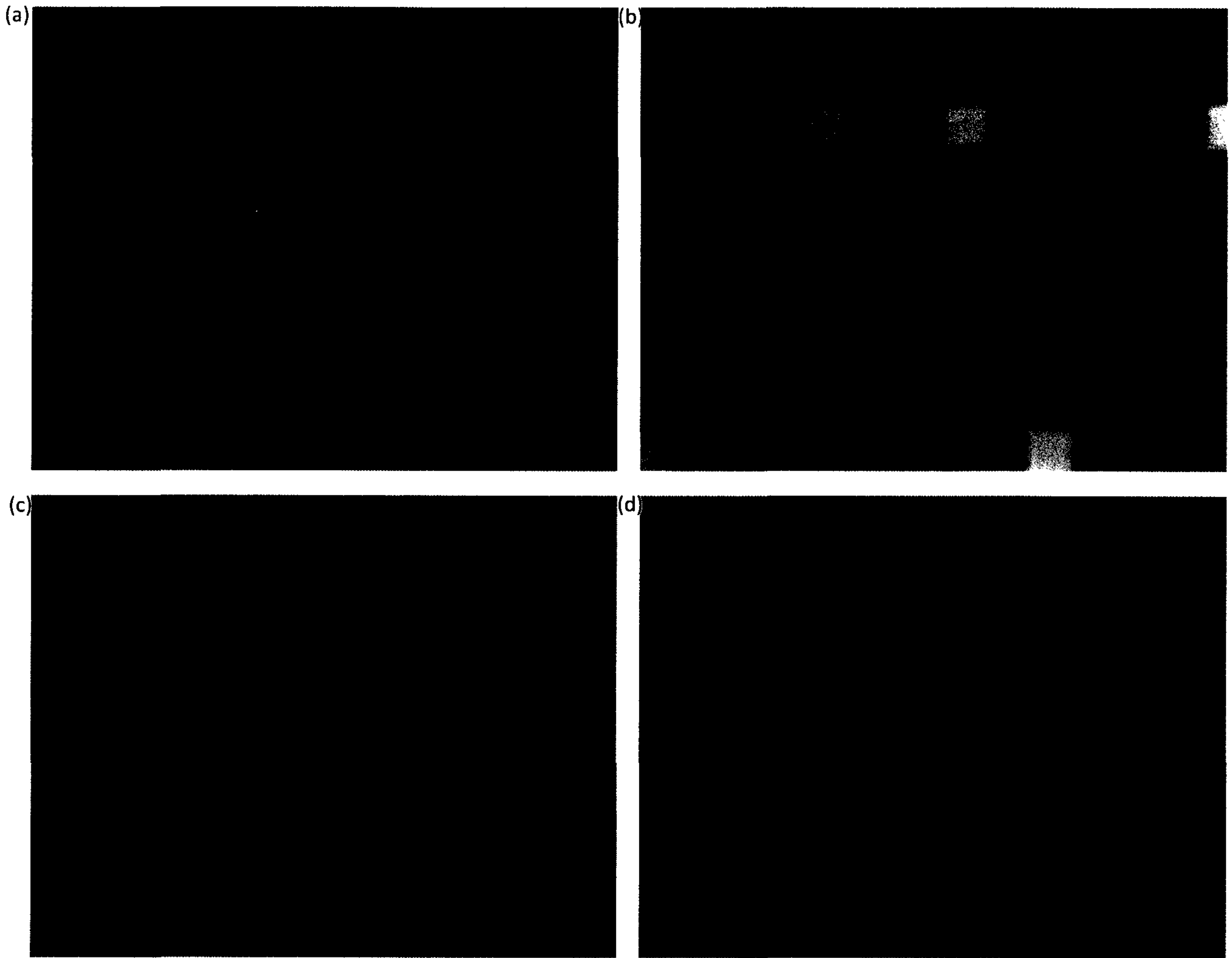

Figure 40: Microscope images of final waveguide devices with etched channels. (a) *10x* mag. MZI and straight waveguides (b) *20x* mag. two arm exposed channel (c) *50x* mag. focused on embedded waveguides(d) *100x* mag. focused on exposed waveguides in channel

5. Optical Characterization

5.1 Setup Description

There are a couple methods of exiting LRSPP modes on metal waveguides. Tapered fiber is one method and was used in [34] where the devices were only bottom cladded with *CYTOP*. In order to test those devices, it was necessary to immerse the devices in a basin filled with liquid which is index-matched to *CYTOP*. This is because one of the main requirements for exciting LRSPP is index matching the top and lower surrounding materials. This setup required using tapered fibers and placing them so that the incident light could couple onto the waveguide at an angle. However, this excitation method presents a big loss in power coupling efficiency.

The devices fabricated in this report are either completely embedded in *CYTOP*, or partially exposed within *CYTOP* cavities. In addition, the channel mask was designed so that when the wafer is diced into dies, all the device facets would be embedded in *CYTOP*. This is shown in Figure 29. Thus end-fire excitation was possible because it did not require a restricting set-up designed to index-match the entire die. It should be noted that the only way of segmenting the wafer into dies is to dice it with a dicing saw. Cleaving along the silicon substrate's crystal plane will not work because *CYTOP* is an amorphous polymer with no distinct long-range crystal structure. Thus, direct cleaving would result in unsmooth tear of the *CYTOP* claddings which pulls on the metal waveguides and destroys the facets.

After the dies have been diced, they were placed in an optical characterization setup shown in Figure 41. This setup involved two micro-positioners that mounted input and output optic fibers. The micro-positioners are spring based and are capable of adjustments in 5 degrees of freedom: the X-Y-Z axis, tilt and swing (Figure 43). The input fiber excites the LRSPP and the output fiber measures the propagated power output. The input fiber is a polarization-maintaining (PM) fiber which was orientated so that the H-field is polarized horizontally. The fiber ends are vertically cleaved with a precision blade cleaver.

This was a necessary step to excite the TM mode required for LRSPP light propagation [23]. The utilized laser wavelength was *1310 nm*. The output fiber is a single mode fiber which captures all the power output by the end facets. Both fibers were *7 μm* in diameter. The die was placed in between the fibers on top of a 2-degree micro-positioner. The adjustment allowed for the die is along the along the Z-X axis. On top of the die was a microscope used for visual alignment between the devices and the fibers. The setup described so far is sufficient to obtain MPA (mode power attenuation) measurements of *CYTOP* embedded devices. However, additional changes had to be made in order to introduce liquid onto the die. A glass lid was made to encapsulate the liquid on top of the die. This lid had drilled holes attached to rubber tubes (Figure 43b). One of the tube was connected to a syringe filled with an index-matched glycerol solution. The lid was glued to an arm and mounted on another 5-degree micro-positioner. A small latex spacer with a rectangular hole cut out in the center was placed between the glass lid and the die (Figure 43a). This latex spacer acted as an "o-ring" to prevent the liquid from leaking out. Creating this liquid-tight seal was very difficult because the glass lid had to be lowered in exact parallel plane with the die. In addition, the latex spacer had to be centered exactly so it does not extrude out the side and hinder fiber alignment at the facets. A temperature controlled sink was used as a mounting stage and placed underneath the die to allow for fine-tuning of the glycerol's optical index. This ensured that the solution's index was matched to that of *CYTOP*'s in order to attain the highest power output possible.

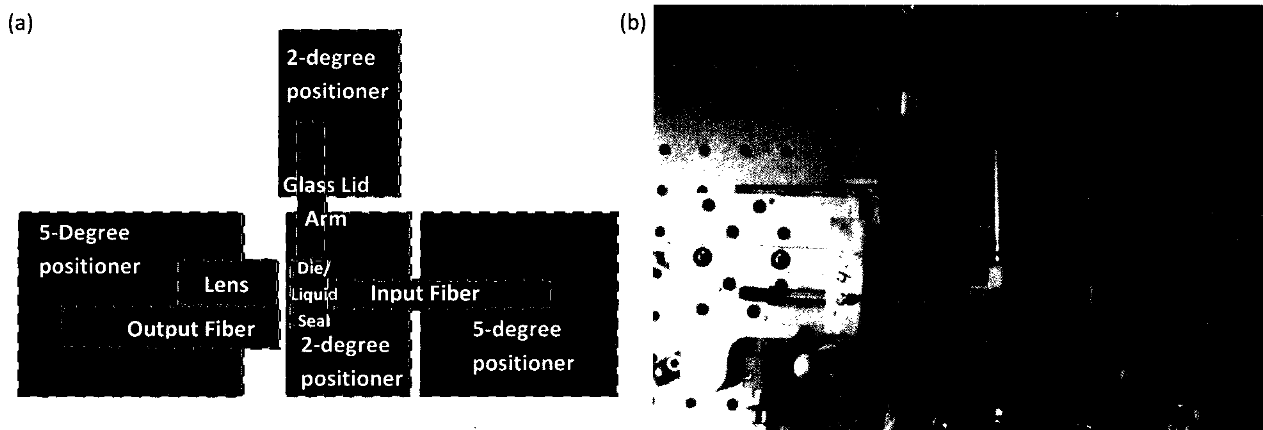

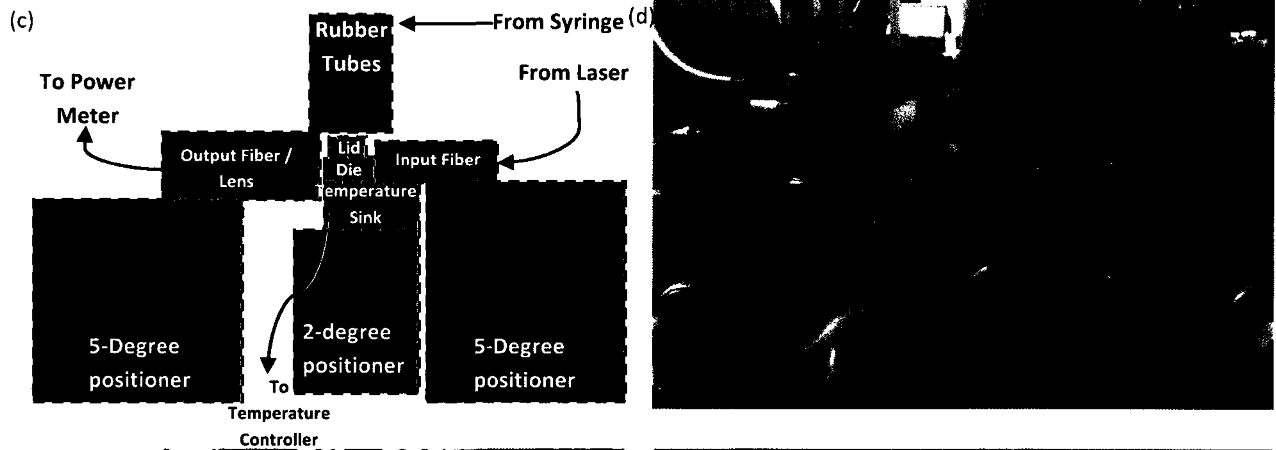

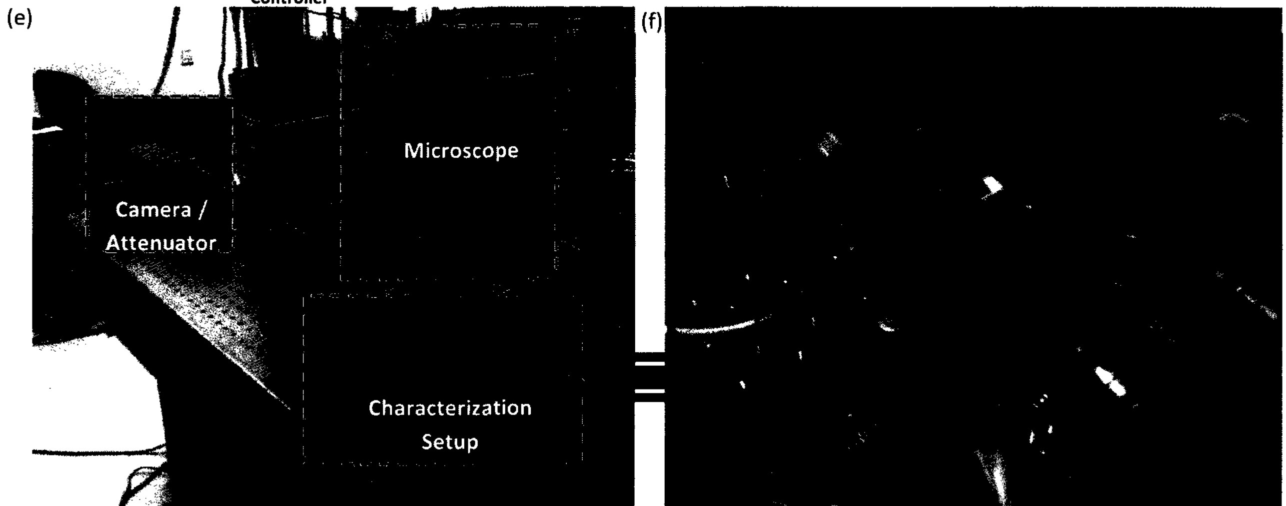

Figure 41: Optical characterization setup (a), (b) top view: schematic and photo. (c), (d) front view: schematic and photo. (e) overall configuration. (f) perspective view of main setup

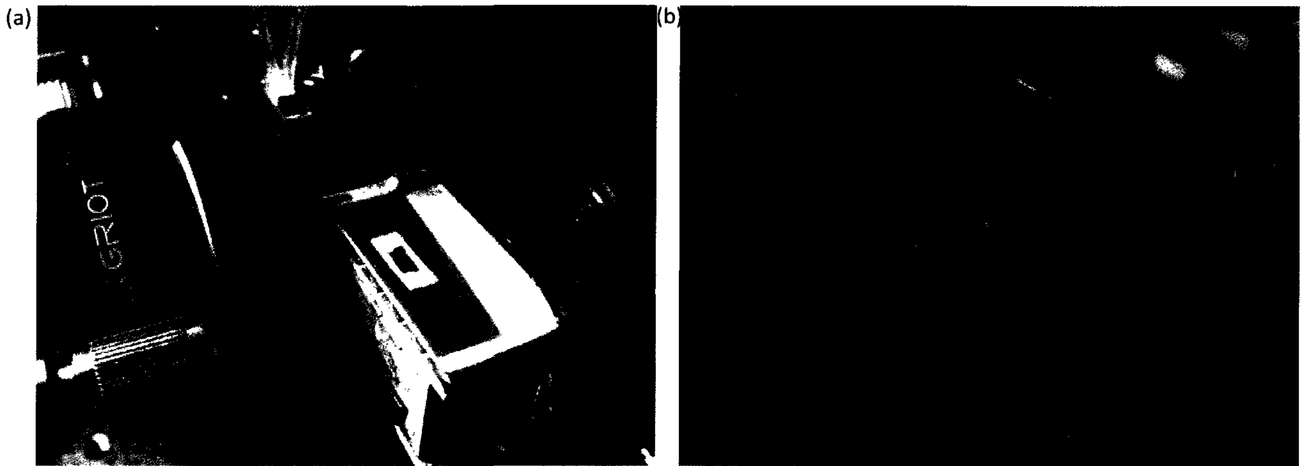

Figure 42: (a) sample die with liquid latex seal on top. (b) glass lid with rubber tubes pressed against seal.

(b) (c)

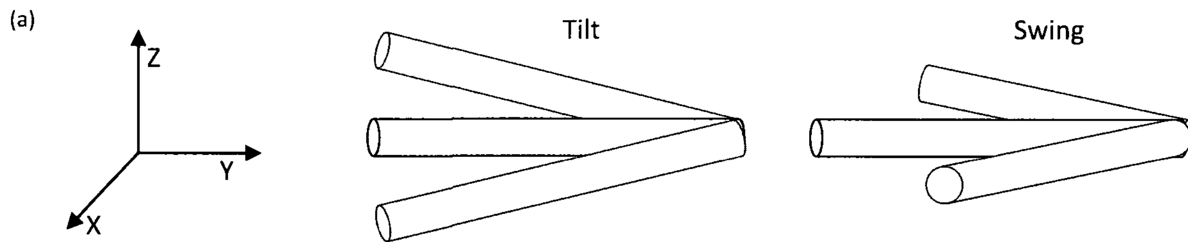

Figure 43: Fiber alignment degrees of freedom. (a) along X-Y-Z axis. (b) tilt in the Z axis. (c) swing along X axis.

5.2 Embedded Device

5.2-1 Measurement

A power cutback curve is a plot which allows us to determine the device MPA per millimeter; as well as the coupling loss for the two end facets. To construct this curve, multiple straight waveguide power outputs were measured. This was first done on fully cladded, *CYTOP* embedded waveguides. However, not all waveguides were of the same length. Waveguides belonging to dies of length *3 mm, 3.8 mm*, and *4.8 mm* were sampled. Having three different lengths is required to properly extrapolate a cutback curve. Before carrying out the optical measurement, a power calibration was first performed by measuring the laser power output from the input fiber. This was done by aligning the output fiber directly to the input fiber and bringing the two ends together as close as possible. This measurement served as the base calibration factor for any power losses incurred by the fiber ends and instruments. Then, the die under test was placed between the fibers. The input fiber was aligned to a single waveguide by carefully observing the output mode using a camera feed connected to a monitor. This mode was focused at the output facet with a lens placed in the optical path. During this visual alignment step, it was important to distinguish the real mode output from substrate/cladding scattering. It was very possible to focus on the wrong "speck" of light and mistake it for the mode. The proper mode output from correct input alignment is shown in Figure 44. This mode will have the characteristics of being strongly localized, sharply focused, brighter than scattered radiation, and easily extinguished when the fiber is moved slightly out of alignment. After the input fiber had been correctly aligned, the lens was replaced with the

output fiber. Approximate alignment was first done visually through the microscope mounted above the setup. The fiber output then was observed in real-time on a power meter. By fine tuning the fiber position and observing the corresponding power output, precise alignment could be accomplished when the reading was tuned to a maximum value.

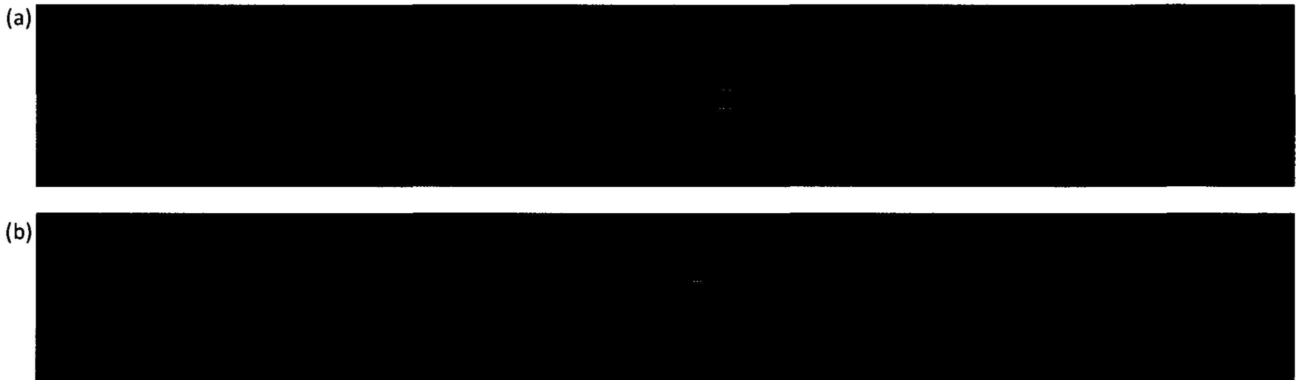

Figure 44: Examples of *CYTOP* embedded, LRSPP output mode profile

5.2-2 Analysis

The output power was recorded and subtracted (in decibels) from the initial fiber input power to determined the entire power loss caused by the inserted waveguides. This analysis is shown in Equation 1.

$$IL_{EW} = P_{IN} - P_{OUT}$$

IL_{EW} = Insertion Loss of Embedded Waveguides
P_{IN} = Measured Input Power from fiber
P_{OUT} = Measured Power Output from device

Equation 1: Insertion loss calculation for straight waveguide in *CYTOP*.

This insertion loss was plotted against its length to construct the power cutback curve. This is shown in Figure 45. The linearly extrapolated slope and y-intercept represent the MPA per millimeter and power loss at the facets (coupling loss), respectively. Two of these curves were constructed from dies of two different wafers. The results are summarized in Table 11 and compared to theoretical simulated values presented in [35].

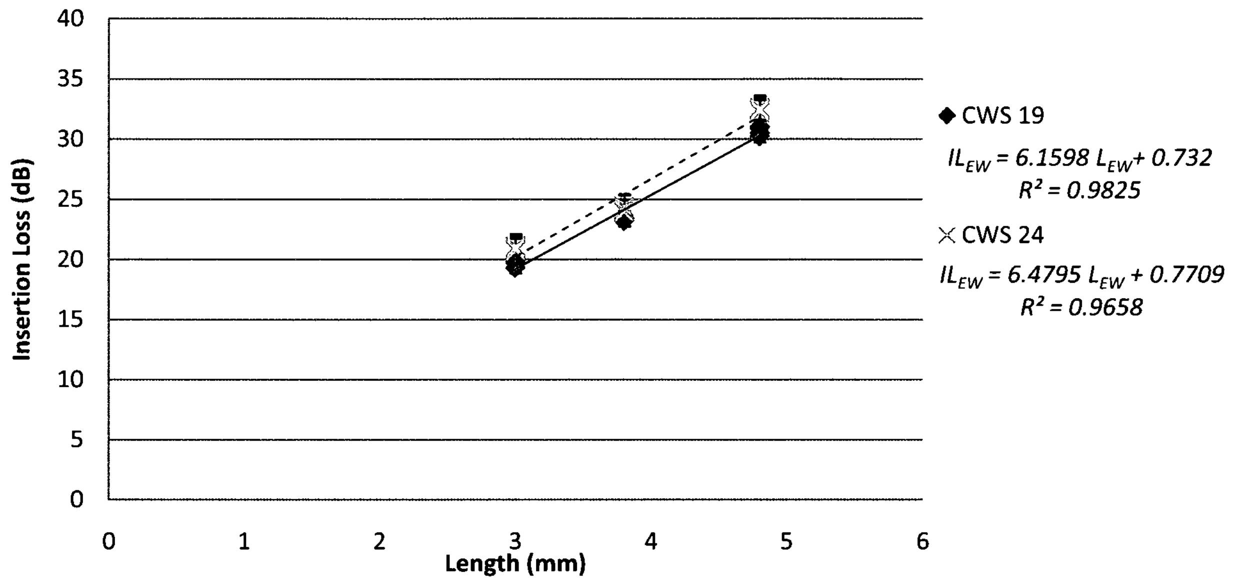

Figure 45: Two MPA cutback curves for straight waveguides embedded in *CYTOP*. IL_{EW} = insertion loss of embedded waveguide. L_{EW} = length of embedded waveguide.

	MPA (dB/mm)	Coupling Loss per facet (Fiber-*CYTOP*, dB)	Coupling Loss per facet (*CYTOP*-Glycerol, dB)
***CYTOP* Embedded (Average)**	6.33	0.38	--
Channel-filled	10.46	--	1.72
Theory [35]	7.2	0.89	0

Table 11: Comparison summary of propagation losses between *CYTOP* embedded, channel filled and theoretical devices

The immediate observation is that the both these values are lower than expected. The reduction in propagation loss can be attributed to the waveguide metal being thinner than the target *35 nm*. In Chapter 2, we have already seen evidence of the metal waveguides being distorted during the cladding process. Although the cladding process was optimized for minimal intrusion, slight distortion was still noticeable after being fully cladded. In addition, the AFM result from Figure 39 showed that the surface of the metal was curved instead of flat. Thus, it is logical to assume that the solvent pressure from the cladding process creates "bulges" on the waveguides. This means that the metal must be stretched horizontally, and compressed vertically in order to make up for the difference in surface length. This is demonstrated in Figure 46 where w_2 is now slightly wider than w_1 and t_2 is now thinner than t_1. An

estimation of w_2 was done by tracing the waveguide surface curvature found in Figure 39c with a CAD software. Assuming that the cross sectional area of the waveguide remains constant ($w_1 x t_1$), the thickness of the curved waveguide could be calculated: $t_2 = 32.8\ nm$. The theoretical MPA for *32.8 nm* thin stripes were calculated to be *6.40 dB/mm*, which is now closer to the measured result of *6.33 dB/mm* presented in Table 11. Since the waveguides are now wider than *5 um*, the excited mode is now of matching size to the fiber's core diameter (*7 um*). This means more power could be transferred from the fiber to the facet with less loss. Thus, the lowered coupling loss is a matching result with the lowered MPA due to thinner, stretched waveguides.

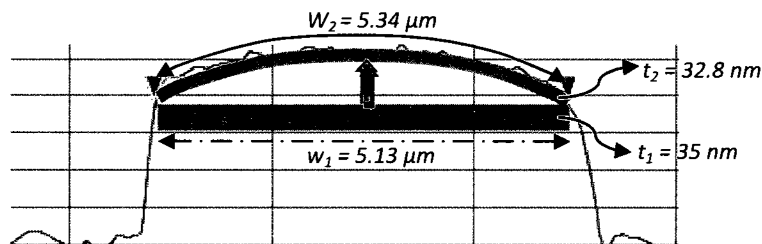

Figure 46: Stretching of waveguide due to *CYTOP* solvent evaporation pressure. Dimensions are now wider and thinner than before. Calculated MPA for flat and curved waveguide is *7.2 dB/mm* and *6.40 dB/mm* respectively. Assumed relevant values used in the calculation were: $w = 34\ nm$, $\varepsilon_{r,Au} = -86.06 - j8.322$, $\varepsilon_{r,CYTOP} = 1.3355$, $\lambda = 1310\ nm$. Calculation performed by Pierre Berini.

5.3 Channel-filled Device

5.3-1 Measurement

The next set of characterization was performed on channel-etched, liquid-filled devices. Again, an initial power output calibration was recorded in order to determine the proper insertion loss. Fiber alignment for both input and output was more difficult to perform on liquid-filled devices. Once the latex seal and glass lid has been lowered onto the die, the devices are no longer visible with the microscope mounted above. Thus, it was necessary to fabricate the seal and the lid to be narrower (in width) than the die. This will allow a narrow border of the die's devices to be visible for alignment. It should be remembered

that the dies were etched so that the devices near the facets are fully cladded. This means it was inconsequential to have those regions of the die excluded from the liquid seal. It should also be remembered that on each die, there are also straight waveguides which are fully cladded throughout their whole length. This means it was possible to conduct power output measurements on theses waveguides without adding on the seal and the lid. This was very helpful because exact alignment could be performed using the same procedure as the fully cladded dies. These waveguides were measured as a preliminary alignment step to eliminate errors in the least obvious degrees of freedom: the tilt and the swing (Figure 43). After those two factors have be tuned for alignment, it was possible to transfer that tuned state to adjacent waveguides by only adjusting the other three degrees of freedom along the X-Y-Z axis. The seal and lid were then placed at the center of die, and the channels were filled using the setup described in Chapter 5.1. Proper alignment along the X-Y-Z axis was possible even with the small border of devices showing. This was because any obvious misalignment would be clearly visible through the camera feed and power meter readings; due to improper mode excitation and high localization of the output. Following that, multiple straight waveguide MPA measurements were made. The observed optical modes were visually similar to that from embedded devices. Except that the intensity was lower and the mode size is smaller. This is shown in Figure 47. Some dies had etched channels and some dies had rectangular openings. This allowed for different lengths of glycerol-immersed waveguides to be sampled. The length of the channels was *1.63 mm* and the cavity lengths were *2.17 mm* and *2.93 mm.* The devices were measured in a similar manner as the process described for fully-cladded dies, with one extra step; the temperature of the heat sink was adjusted to tune the index of the glycerol. A summary of refractive indices for *CYTOP*, glycerol and water is shown in Table 12. The results were measured with the prism coupler tool with a wavelength of *1312 nm*. We see that there is an index mismatch of 0.003 between S-grade *CYTOP* (bulk claddings) and glycerol. Thus, electronic temperature control was required to minimize this mismatch as much as possible.

CYTOP (S)	*CYTOP* (M)	Glycerol 1S	Water
1.334	1.336	1.331	1.319

Table 12: Refractive index comparison between relevant materials. Index accurate for λ = *1312 nm*. Data collected by Ewa Lisicka-Shrzek.

(a)

(b)

Figure 47: Examples of channel-filled, LRSPP output mode profile.

5.3-2 Analysis

The goal of measuring liquid-filled waveguides was to construct a power cutback curve to analyze the performance of waveguides immersed in index-matched solutions. This curve can then be compared with that of *CYTOP* embedded devices. However, the channel/cavity dies had both fully cladded regions and metal exposed regions. The measured insertion loss contained power loss incurred by waveguides in both regions. The contribution made by the embedded regions had to be removed before comparisons can be made. To accomplish this, the lengths of the embedded regions were first determined by subtracting the channel/cavity length from its corresponding die lengths. Then, the loss incurred by the embedded waveguides was calculated using known values of MPA per millimeter and facet coupling loss; which were extracted from cutback curves in Figure 45. Thus, the insertion loss of the channel/cavity regions were determined by taking the measured values, subtracting it from the initial power calibration output, minus the calculated fiber-facet coupling losses and the propagation loss of the embedded regions. The described formula is shown in Equation 2.

$$IL_{CH} = P_{IN} - P_{OUT} - P_C - (P_{EW} \times L_{EW})$$

IL_{CH} = Insertion Loss of filled-Channels waveguide
P_{IN} = measured Input Power from fiber
P_{OUT} = measured Output Power from device
P_C = Fiber-to-*CYTOP* Coupling loss (input & output facets)
P_{EW} = Mode Power Attenuation of Embedded Waveguide (MPA)
L_{EW} = Embedded Waveguide length (millimeter)

Equation 2: Insertion loss calculation for straight waveguides in liquid-filled channels.

The result was plotted to extrapolate the power cutback curve for channel/cavity-filled straight waveguides. This is shown in Figure 48. The extrapolated fit shows that the MPA is *10.47 dB/mm*. This is about *4 dB/mm* higher than that of *CYTOP* embedded devices. Furthermore, the coupling loss incurred from the transition between *CYTOP* and glycerol media is *3.4 dB*. Both of these values are surprisingly high values and deviate from theory (Table 12). The channel-filled devices were expected to exhibit equal quantitative performance as the *CYTOP* embedded devices with zero coupling loss between mediums. The high loss results suggested that there are additional unforeseen factors. The quick explanation could be that the liquid remained optically mismatched, even with temperature control. Recall that in Table 12 there is a $\Delta n = 0.003$ default index mismatch between S-grade *CYTOP* and Glycerol 1S. It is possible that the temperature sink was not effective enough to offset this mismatch. In order to confirm this theory, the *Metricon* prism coupler will have to be modified to support sample index measurement with temperature control. However, it is unlikely that $\Delta n = 0.003$ mismatch can cause a *10 dB* difference between the two MPA curves.

One other explanation for high MPA values could be that the waveguides are not completely immersed in the glycerol solution. This can happen because the *CYTOP* surface is very hydrophobic. This is problematic because air gaps could potentially form within the channels which will greatly attenuate the propagating LRSPP. Possible sites for these air gaps are the corners between the raised devices and the *CYTOP* surface. This is illustrated in Figure 49. As mentioned in Chapter 4.2-3 the channels are over-etched by about *1 μm*, which means that the corners are comprised of two *CYTOP* surfaces meeting at a

right angle. The convergence of the two hydrophobic surfaces could very likely prevent liquid infiltration. Judging from the reproducibility of the collected data, it is reasonable to theorize that this is a non-random, localized phenomenon. This suggests that the corner air pockets could uniformly span across the entire length of the waveguides. No further work was done to confirm this theory.

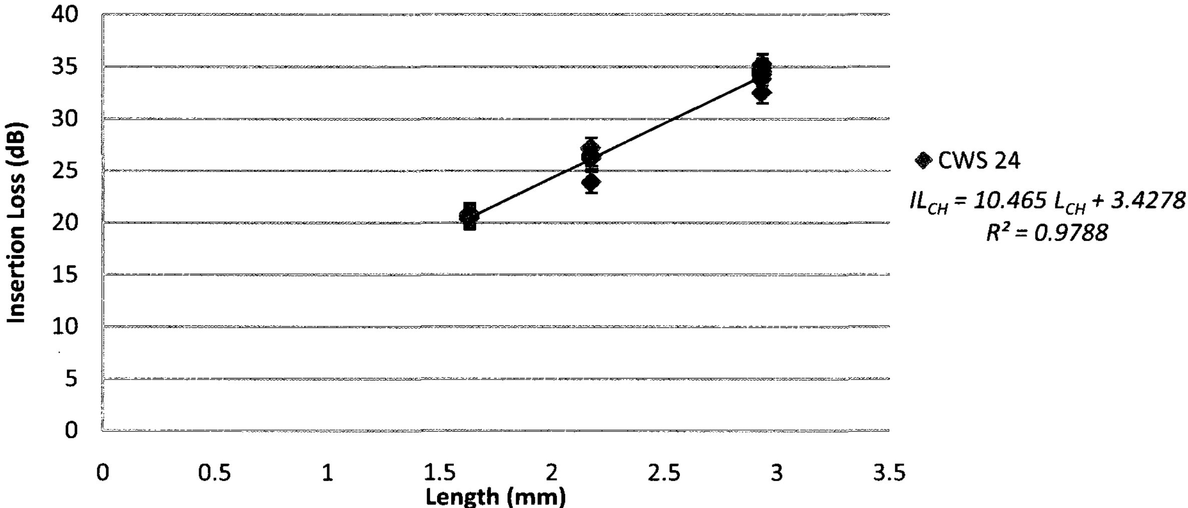

Figure 48: MPA cutback curve for straight waveguides in liquid-filled channel. IL_{CH} = insertion loss of liquid-filled channels. L_{CH} = length of liquid-filled channels.

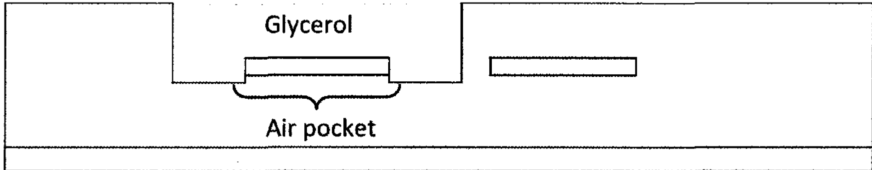

Figure 49: Possible locations for air pockets.

It is also suspected that large attenuation could have been caused by extraneous material left on the waveguide surface shown in Figure 39e & g. Material analysis will have to be conducted to determine the composition of the extraneous material and also how to remove it.

6. Concluding Remark and Future Work

This thesis extended the pursuit of realizing integrated LRSPP biochemical sensors. To that end, gold stripe waveguide devices were fabricated in *CYTOP* fluoropolymer claddings. The claddings were built through repeated spin-coats below and above the waveguide structures. Optical measurements were performed using a prism coupler to determine the optical index and thickness of the *CYTOP* claddings. The optical index was determined to be *1.334* (λ=*1312 nm*) for S-grade *CYTOP*; the top and bottom thickness was around *10 μm* and *8 μm* respectively. The waveguide devices were realized through a bi-layer lithography process and *Au* deposition with an electron-beam metal evaporator. The bi-layer procedure was developed and tuned to achieve the proper dimension accuracy. The waveguides were designed to be *35 nm* in thickness and *5 μm* wide. Actual structures were studied under SEM and AFM; the waveguide dimensions were *37 nm* in thickness and 5.1 *μm* in width. It was determined that the waveguide structure profile changed after being embedded in top *CYTOP* claddings. This was due to *CYTOP*'s solvent diffusing to the lower cladding and then creating pressure on the structures during the baking process. This issue was minimized as much as possible by coating thin layers top and baking with low temperatures. Once the waveguide devices have been embedded in *CYTOP*, a second level lithography was performed to pattern microfluidic channels. The channel structures were realized through O_2 plasma etching of top *CYTOP* claddings. The channels were *55 μm* in width and the length spanned across entire sensor arms (millimeters) of Mach-Zehnder interferometers (MZI). The etch rate was studied and determined to be *0.92 μm/min*. This was helpful in timing the etch process for exposing the waveguide devices without too much over-etch into the lower *CYTOP* claddings. The over-etch was minimized to be around *1 μm* below the *Au* surface. The fabricated wafers were then diced into small dies and subjected to optical testing. The characterization setup involved fiber optic excitation and detection through end-fire coupling. A power cutback curve was constructed for separate straight waveguides embedded in *CYTOP*, and those immersed in glycerol. The mode power attenuation (MPA)

per millimeter was extracted from curve fitting and determined to be *6.33 dB/mm* and *10.46 dB/mm* respectively. Both of these values did not match with the theoretical value of *7.2 dB/mm*. It was suspected that the *CYTOP* embedded waveguides have lower MPA because the waveguide thickness had decreased through stretching caused by *CYTOP* solvent pressure. Possible reasons for the glycerol immersed waveguides having a higher MPA include: index mismatch between *CYTOP* and glycerol, air pockets caused by *CYTOP*'s hydrophobic nature and extraneous material on waveguide surface.

This thesis contributed two milestones towards the advent of integrated LRSPP biosensors. These are the fabrication and characterization of: 1) LRSPP straight *Au* waveguides embedded in *CYTOP*, 2) utilization of integrated microfluidic channels to enable practical, selectable delivery of sensing fluid. Suggested future work to improve performance and practical implementation include: 1) process to prevent waveguide deformation due to *CYTOP* solvent, 2) confirmation of factors causing high MPA values in liquid-filled devices, 3) fabrication of fluidic lids with ports for robust device packaging and 4) integration of active devices such as lasers and detectors.

Appendix

I. Processed Wafer List

Wafer	CYTOP Grade	Wafer Size (in.)	Top cladd. thickness (um)	Bottom cladd. Thickness (um)	Litho. Process	Descriptions	Available Results
CWT10	M	2	12.00	9.00	Old	M-grade cladded waveguides w/ CF4/O2 etched channels	Microscope
CWT11	M	2	12.00	9.00	Old	M-grade cladded waveguides (not etched)	Microscope, SEM
CWT12	M	2	12.00	9.00	Old	M-grade cladded waveguides (not etched)	Microscope, Prowerpoint
CLT3	S	2	0.00	4.30	New	bi-layer litho. test wafer: first complete revision	Microscope, AFM
CLT4	S	2	0.00	3.76	None	Cytop thickness test wafer, spun at cold temp.	Metricon
CLT5	S	2	0.00	6.02	None	Cytop thickness test wafer, spun at cold temp.	Metricon
CLT6	S	2	0.00	7.70	None	Cytop thickness test wafer, spun at cold temp.	Metricon
CLT7	S	2	5.20	8.40	None	Cytop thickness, CF4/O2&O2 etching test wafer, spun at room temp.	Metricon, SEM, raw data
CLT8	S	2	0.00	8.49	None	Cytop thickness, thick resist litho test, spun at room temp.	Metricon
CLT9	S	2	10.17	8.50	None	Cytop thickness, CF4/O2 etching, thick resist litho. test wafer. Spun at room temp.	Metricon, SEM, litho. data
CLT10	S	2	10.42	8.88	None	Cytop thickness, thick resist litho. test wafer. Spun at room temp.	Metricon, SEM, litho. Data, Powerpoint
CLT13	S	4	9.49	10.40	Old	Cytop thickness test wafer with cladded waveguides & etched channels	Microscope, Metricon, Profiler data
CLT16	S	2	0.00	3.00	Old	bi-layer litho test wafer: varying spin speed	Microscope
CLT17	S	2	0.00	5.52	New	bi-layer litho test wafer: metal thickness/roughness adjustment	AFM
CLT18	S	2	0.00	5.52	New	bi-layer litho test wafer: metal thickness/roughness adjustment	SEM
CLT19	S	2	0.00	10.40	New	bi-layer litho test wafer: dimension adjustment	Microscope
CLT20	S	2	0.00	11.60	New	bi-layer litho test wafer: dimension adjustment	Microscope, SEM
CLT21	S	2	0.00	11.70	New	bi-layer litho test wafer: dimension adjustment	Microscope, SEM
CLT22	S	2	0.00	10.40	New	bi-layer litho test wafer: dimension adjustment (meant for AFM)	Microscope, SEM, Powerpoint
CLT23	S	2	0.00	9.80	New	bi-layer litho test wafer: dimension adjustment	SEM
CLT24	S	2	0.00	9.80	New	bi-layer litho test wafer: dimension adjustment	SEM
CLT25	S	2	0.00	9.80	New	bi-layer litho test wafer: dimension adjustment	SEM
CLT26	S	2	0.00	9.80	New	bi-layer litho test wafer: dimension adjustment	SEM, Powerpoint
CWS4	S	2	13.00	4.30	Old	S-grade cladding and etch tests	Microscope, SEM, Powerpoint
CWS5	S	2	11.70	4.30	Old	S-grade cladding and etch tests	Microscope
CWS6	S	2	11.70	4.30	Old	S-grade cladding and etch tests	Microscope, Powerpoint
CWS7	S	4	0.00	10.60	Old	uncladded waveguides on thick Cytop for AFM	Microscope
CWS8	S	4	0.00	10.60	Old	uncladded waveguides on thick Cytop for AFM	Microscope
CWS11	S	4	9.40	10.60	Old	etched channels w/cladded waveguides	Microscope, SEM
CWS12	S	4	7.55	10.60	Old	etched L1 openings w/cladded waveguides	Microscope, Profiler data
CWS13	S	4	8.95	10.60	Old	etched channels w/ cladded waveguides	Microscope, Profiler data
CWS15	S	4	0.00	10.60	New	uncladded waveguides on thick Cytop for glass bonding	Microscope
CWS16	S	4	0.00	10.60	New	uncladded waveguides on thick Cytop for glass bonding	Microscope, AFM
CWS17	S	4	0.00	10.60	New	uncladded LTI11 waveguides	Microscope
CWS18	S	4	0.00	10.60	New	uncladded LTI11 waveguides	Microscope
CWS19	S	4	10.38	10.60	New	etched channels w/ cladded waveguides	Microscope, Profiler data
CWS21	S	2	9.68	9.80	New	etched channels w/cladded waveguides	Microscope, Profiler data
CWS22	S	2	10.51	9.80	New	etched L1 openings w/cladded waveguides	Microscope, Profiler data, AFM
CWS23	S	2	9.50	9.80	New	etched channels w/cladded waveguides (over-etched rough surface)	Profiler Data
CWS24	S	2	9.16	9.80	New	etched L1 openings w/cladded waveguides	Microscope, Profiler data

Table 13: Process record details of fabricated wafers. Simultaneous process batches are grouped together in boxes.

II. CWS 19 Microscope Process History

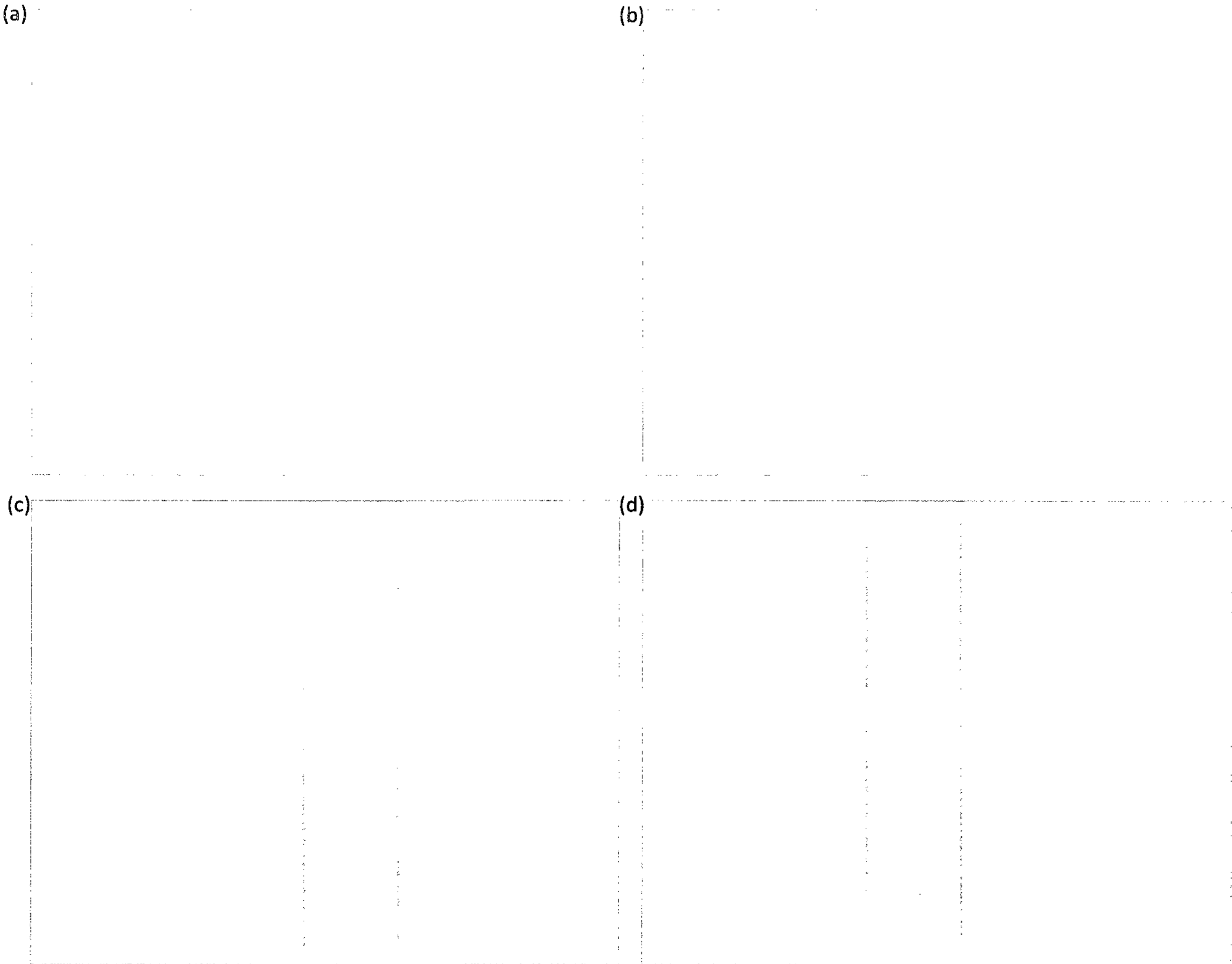

Figure 50: Bi-layer lithography pattern as described in Chapter 3.1. (a), (b) *10x* magnification. (c), (d) *100x* magnification

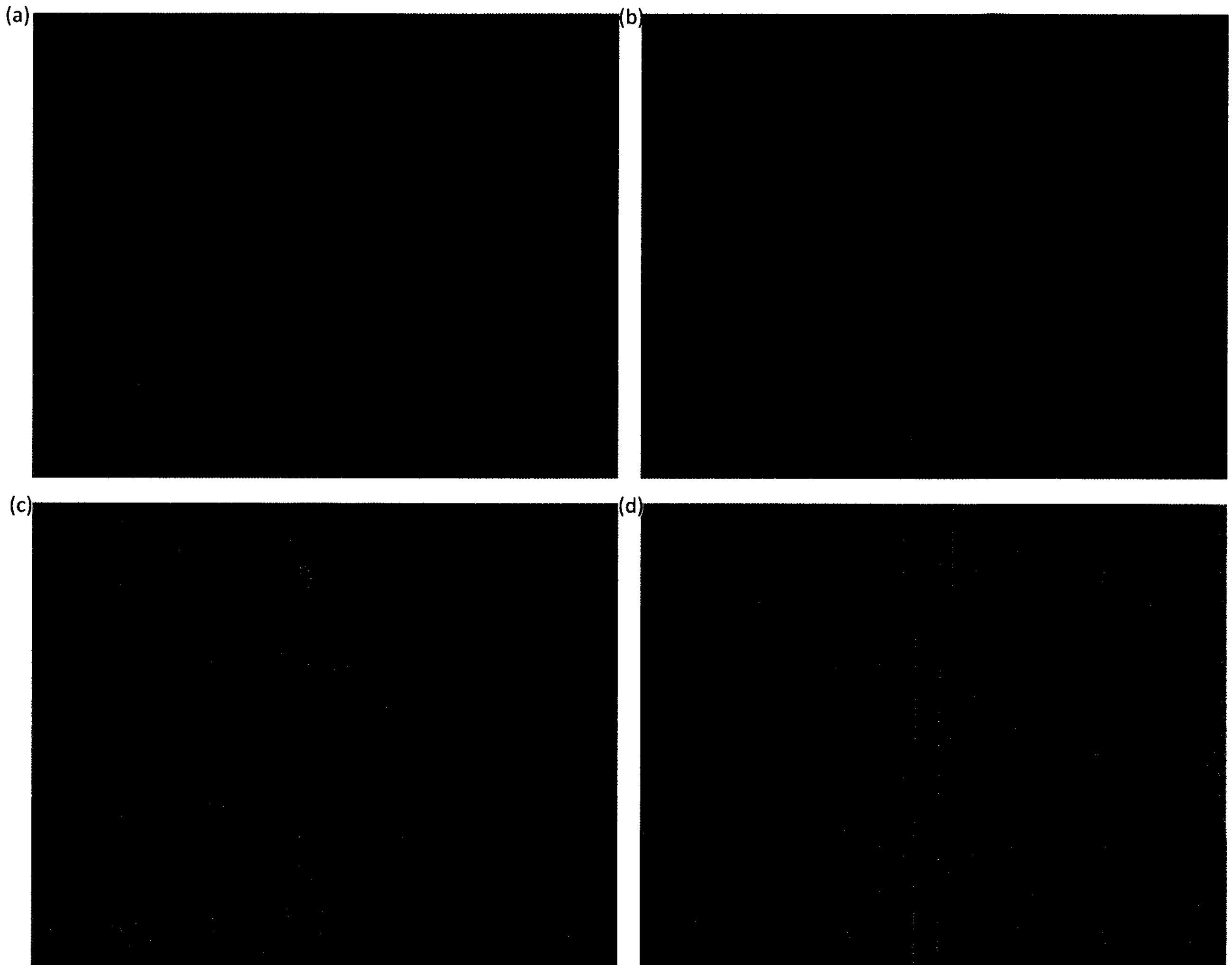

Figure 51: ***Au*** **waveguide devices on half cladded** ***CYTOP*** **as described in Chapter 3.1. (a), (b)** ***10x*** **magnification. (c), (d)** ***100x*** **magnification**

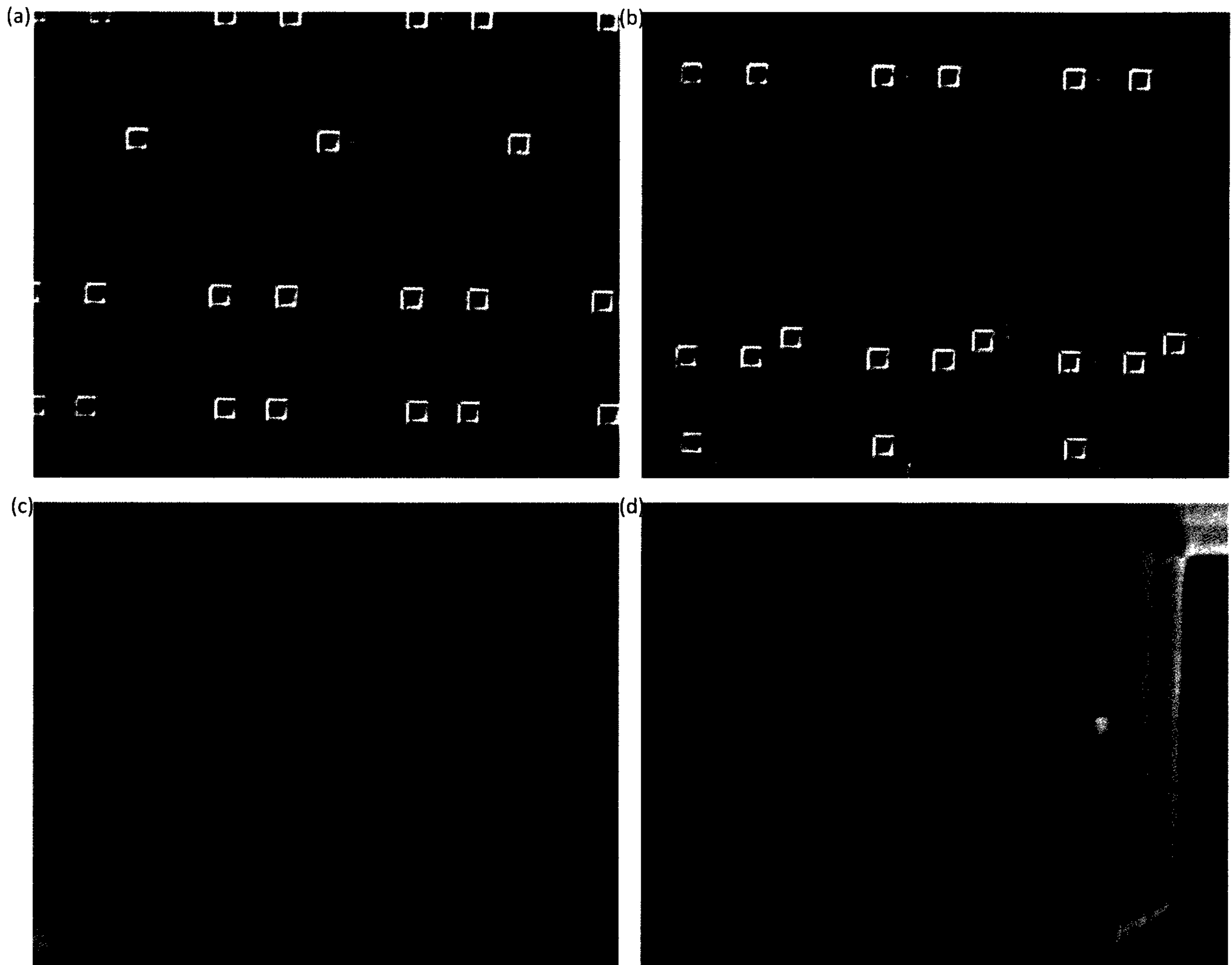

Figure 52: ***Au*** **waveguide devices in fully cladded (embedded)** ***CYTOP*** **as described in Chapter 2.2. (a), (b)** ***10x*** **magnification. (c), (d)** ***100x*** **magnification**

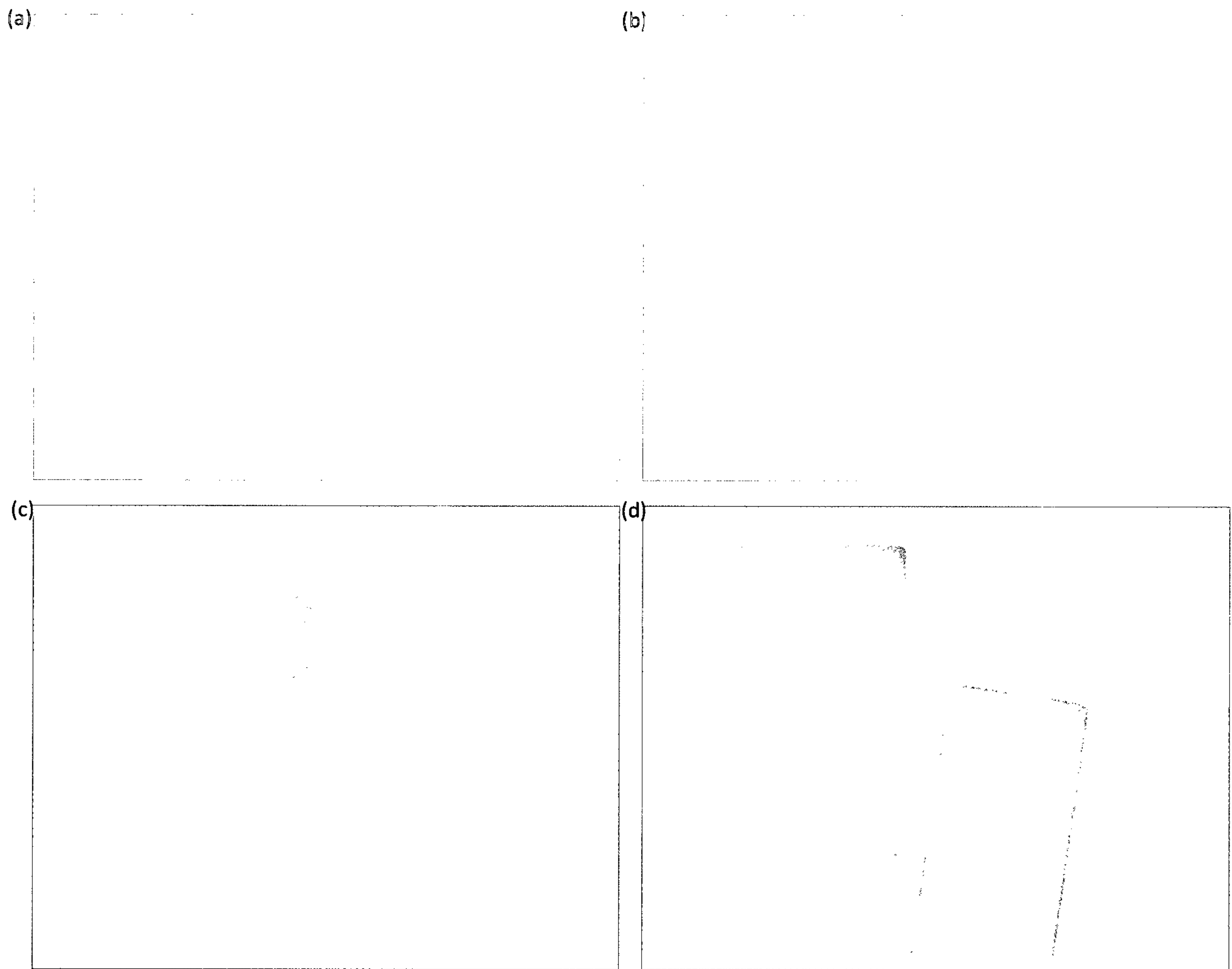

Figure 53: Microfluidic channel lithography as described in Chapter 3.2. (a), (b) *10x* magnification. (c) *100x* magnification focused on waveguide. (d) *100x* magnification focused on channel pattern.

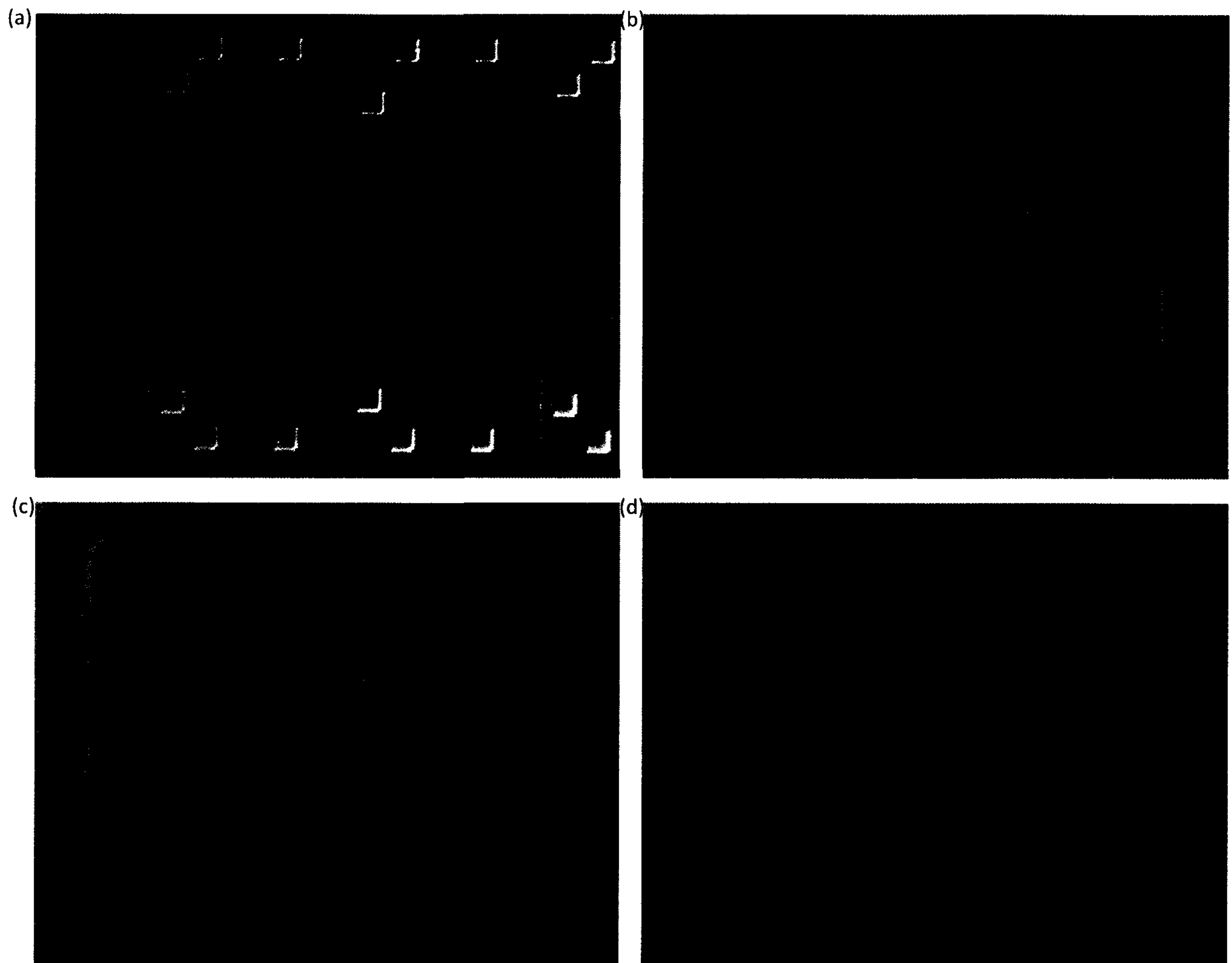

Figure 54: ***Au*** **waveguide devices embedded in CYTOP with etched microfluidic channels as described in Chapter 4.2. (a), (b)** ***10x*** **magnification. (c)** ***100x*** **magnification focused on waveguide. (d)** ***100x*** **magnification focused on channel opening.**

References

[1] P.N. Prasad, *"Introduction to Biophotonics"*, John Wiley and Sons Inc. (2003)

[2] M. A. Cooper, *"Optical biosensors: where next and how soon"*, Dug Discovery Today, Vol. 11, 1061 (2006)

[3] B.Kuswandi, R. Andres, R. Narayanaswamy, *"Optical fibre biosensors based on immobilised enzymes"*, Analyst, Vol. 126, 1469 (2001)

[4] B. Kuswandi, C. I. Fikriyah, A. A. Gani, *"An optical fiber biosensor for chlorpyrifos using a single sol–gel film containing acetylcholinesterase and bromothymol blue"*, Talanta, Vol. 74, 613 (2008)

[5] N. Skivesen, A. Têtu, M. Kristensen, J. Kjems, L. H. Frandsen, P. I. Borel, *"Photonic-crystal waveguide biosensor"*, Optics Express, Vol. 15, 3169 (2007)

[6] M. M. W. Muscatello, S. A. Asher, *"Poly(vinyl alcohol) Rehydratable Photonic Crystal Sensor Materials"*, Advanced Functional Materials, Vol. 18, 1 (2008)

[7] L. Rindorf, J.B. Jensen, M. Dufva, L. H. Pedersen, P. E. Høiby, O. Bang, *"Photonic crystal fiber long-period gratings for biochemical sensing"*, Optics Express, Vol. 14, 8224 (2006)

[8] E. J. Cho, F. V. Bright, *"Optical Sensor Array and Integrated Light Source"*, Analytical Chemistry, Vol. 73, 3289 (2001)

[9] W. G. Holthoff, E. C. Tehan, R. M. Bukowski, N. Kent, B. D. MacCraith, F. V. Bright, *"Radioluminescent Light Source for the Development of Optical Sensor Arrays"*, Analytical Chemistry, Vol. 77, 718 (2005)

[10] P. K. Yuen, N. H. Fontaine, M. A. Quesada, P. Mazumder, R. Bergman, E. J. Mozdy, *"Self-referencing a single waveguide grating sensor in a micron-sized deep flow chamber for label-free biomolecular binding assays"*, Lab Chip, Vol. 5, 959 (2005)

[11] K. Tiefenthaler, W. Lukosz, *"Sensitivity of grating couplers as integrated-optical chemical sensors"*, Opt. Soc. Am. B, Vol. 6, 209 (1989)

[12] A. Leung, P. M. Shankar, R. Mutharasan, *"A review of fiber-optic biosensors"*, Sensors and Actuators B, Vol. 125, 688 (2007)

[13] A. Densmore, D.-X. Xu, S. Janz, P. Waldron, T. Mischki, G. Lopinski, A. Delâge, J. Lapointe, P. Cheben, B. Lamontagne, J. H. Schmid, *"Spiral-path high-sensitivity silicon photonic wire molecular sensor with temperature-independent response"*, Optics Letter, Vol. 33, 596 (2008)

[14] B. Sepúlveda, J. Sánchez del Río, M. Moreno, F. J. Blanco, K. Mayora, C. Domínguez, L. M. Lechuga, *"Optical biosensor microsystems based on the integration of highly sensitive Mach–Zehnder interferometer devices"*, J. Opt. A: Pure Appl. Opt., Vol. 8, S561 (2006)

[15] A. Densmore, D.X. Xu, P. Waldron, S. Janz, A. Delâge, P. Cheben, J. Lapointe, "Thin *silicon waveguides for biological and chemical sensing"*, Proc. of SPIE, Vol. 6477, 647718 (2007)

[16] F. Prieto, B. Sepúlveda, A. Calle, A. Llobera, C. Domínguez, A. Abad, A. Montoya and L. M. Lechuga, *"An integrated optical interferometric nanodevice based on silicon technology for biosensor applications"*, Nanotechnology, Vol. 14, 907 (2003)

[17] P. W. Milonni, J. H. Eberly, *"Lasers"*, John Wiley & Sons (1991)

[18] C. Kittel, *"Introduction to Solid State Physics – 8th Edition"*, John Wiley & Sons (2005)

[19] W. L. Barnes, A. Dereux, T. W. Ebbesen, *"Surface plasmon subwavelength optics"*, Nature, Vol . 424 (2003)

[20] S. A. Maier, H. A. Atwater, *"Plasmonics: Localization and guiding of electromagnetic energy in metal /dielectric structures"*, J. App. Phys., Vol. 98, 01101 (2005)

[21] A. Otto, *"Excitation of nonradiative surface plasma waves in silver by the method of frustrated total reflection"*, Z. Phys., Vol. 216, 398 (1968)

[22] E. Kretschmann, *"Die Bestimmung optischer Konstanten von Metallen durch Anregung von Oberfliichenplasmaschwingungen"*, Z. Phys., Vol. 241, 313 (1971)

[23] P. Berini, *"Long-range surface plasmon polaritons"*, Advances in Optics and Photonics, Vol. 1, 484 (2009)

[24] P. Berini, *" Bulk and surface sensitivities of surface plasmon waveguides"*, New J. of Phy., Vol. 10, 105010 (2008)

[25] M. Tencer, P. Berini, *"Toposelective Electrochemical Desorption of Thiol SAMs from Neighboring Polycrystalline Gold Surfaces"*, Langmuir, Vol. 24, 12097 (2004)

[26] D. Sarid, *"Long-range surface-plasma waves on very thin metal films"*, Phys. Rev. Lett., Vol. 47, 1927 (1980)

[27] P. Berini, *"Plasmon-polariton waves guided by thin lossy metal films of finite width: Bound modes of symmetric structures"*, Physical Review B, Vol. 61, 10484 (2004)

[28] R. Charbonneau, P. Berini, E. Berolo, E. Lisicka-Shrzek, *"Experimental observation of plasmon–polariton waves supported by a thin metal film of finite width"*, Optics Letter, Vol. 25, 844 (2000)

[29] P. Berini, *"Plasmon-polariton waves guided by thin lossy metal films of finite width: Bound modes of asymmetric structures"*, Physical Review B, Vol. 63, 125417 (2001)

[30] T. Nikolajsen, K. Leosson, S. I. Bozhevolnyi, *"In-line extinction modulator based on long-range surface plasmon polaritons"*, Optics Communications, Vol. 244, 455 (2005)

[31] R. Slavík, J. Homola, *"Ultrahigh resolution long range surface plasmon-based sensor"*, Sens. Actuators B, Vol. 123, 10 (2007)

[32] A.W. Wark, H. J. Lee, R. M. Corn, *"Long-range surface plasmon resonance imaging for bioaffinity sensors"*, Anal. Chem., Vol. 77, 3904 (2005)

[33] J. Dostálek, A. Kasry, and W. Knoll, *"Long range surface plasmons for observation of biomolecular binding events at metallic surfaces"*, Plasmonics, Vol. 2, 97 (2007)

[34] R. Daviau, E. Lisicka-Skrzek, R. N. Tait, and P. Berini, *"Broadside excitation of surface plasmon waveguides on CYTOP"*, Appl. Phys. Lett., Vol.94, 091114 (2009)

[35] R. Daviau, A. Khan, E. Lisicka-Skrzek, R. N. Tait, and P. Berini, *"Fabrication of surface plasmon waveguides and integrated components on CYTOP"*, submitted to Microelectron. Eng. (2009)

[36] K.R. Williams, R. S. Muller, *"Etch Rates for Micromachining Processing"*, J. MEMS, Vol. 5, 256 (1996)

[37] K.R. Williams, K. Gupta, M. Wasilik, "Etch *Rates for Micromachining Processing-Part II"*, J. MEMS, Vol. 12, 761 (2003)

[38] *"Amorphous Fluoropolymer CYTOP: Tehcnical Data"*, Asahi Glass Company, http://www.agc.cp.jp

[39] R. Buckley and P. Berini, "Figures *of merit for 2D surface plasmon waveguides and application to metal stripes"*, Opt. Express Vol. 15, 12174 (2007)

[40] Berini, P., Charbonneau, R., Lahoud, N., Mattiussi, G., *"Characterisation of long-range surface plasmon-polariton waveguides"*, (AIP) Journal of Applied Physics, Vol. 98, 1 (2005)

[41] R. Charbonneau, C. Scales, I. Breukelaar, S. Fafard, N. Lahoud, G. Mattiussi, P. Berini, *"Passive Integrated Optics Elements Based on Long-Range Surface Plasmon Polaritons"*, J. of Lightwave Technology, Vol. 24, 477 (2006)

[42] R. Charbonneau, N. Lahoud, G. Mattiussi, P. Berini, *"Demonstration of integrated optics elements based on long-ranging surface plasmon polaritons"*, Optics Express, Vol. 13, 977(2005)

[43] J. Melin, K. Hedsten, A. Magnusson, D. Karlén, H. Rödjegård, K. Persson, J. Bengtsson, P. Enoksson, F. Nikolajeff, "Microreplication *in a silicon processing compatible polymer material"*, J. Micromech. Microeng., Vol. 15, S116 (2005)

[44] *"Microposit™ SPR™220 Series Photoresists"*, Rohm and Hass Electronic Materials, http://www.rohmhaas.com

[45] *"Microposit® Remover 1165"*, Rohm and Hass Electronic Materials, http://www.rohmhaas.com

[46] *"Microposit^{TM} S1800^{TM} G2 Series Photoresists"*, Rohm and Hass Electronic Materials, http://www.rohmhaas.com

[47] *"LOR and PMGI Resists"*, MicroChem, http://www.microchem.com/

[48] M. J. Madou, *"Fundamentals of Microfabrication: The Science of Miniaturization, Second Edition"*, CRC (2002)